SPECTROSCOPIC STUDY OF THE FUNDAMENTAL BAND OF CARBON MONOXIDE FOR ATMOSPHERIC COMPOSITION RETRIEVALS

NAZRUL ISLAM
Master of Science, Physics, Jahangirnagar University, 2012

A Thesis
Submitted to the School of Graduate Studies
Of the University of Lethbridge
in Partial Fulfillment of the
Requirements for the Degree

MASTER OF SCIENCE

Department of Physics and Astronomy
University of Lethbridge
LETHBRIDGE, ALBERTA, CANADA

SPECTROSCOPIC STUDY OF THE FUNDAMENTAL BAND OF CARBON MONOXIDE FOR ATMOSPHERIC COMPOSITION RETRIEVALS

NAZRUL ISLAM

Date of Defense: January 10, 2017

Dr. Adriana Predoi-Cross Supervisor	Professor	Ph.D.
Dr. Michael Gerken Co-Supervisor	Professor	Ph.D.
Dr. Brant Billinghurst Examination Committee Member Staff Scientist at Canadian Light Source Saskatoon, Saskatchewan	Staff Scientist	Ph.D.
Dr. Craig Coburn Examination Committee Member	Associate Professor	Ph.D.
Dr. Albert Cross Examination Committee Member Founder, AC^2 Scientific	Adjunct Professor	Ph.D.
Dr. Behnam Seyed Mahmoud Chair, Thesis Examination Committee	Associate Professor	Ph.D.

Abstract

Over the past couple of decades, the study of infrared spectra of carbon monoxide has been the subject of interest because of its existence in the Earth's atmosphere as well in different planetary atmospheres. This work presents a line-shape study transitions of pure carbon monoxide and carbon monoxide mixed with air in the fundamental band, recorded over a temperature range from 79 K to 296 K using a high-resolution Fourier Transform Spectrometer (FTS). In this study, different pressure induced line-shape parameters as well as their temperature dependences have been measured and compared with relevant previous published results. Also, the transformation of line-shapes due to line-mixing and Dicke narrowing effects have been investigated. Two semi-empirical approaches, namely: the Exponential Power Gap (EPG) and Energy Corrected Sudden (ECS) approximation have been employed for theoretical calculation of line-mixing coefficients which show good agreement with the measured values.

Acknowledgements

I would like to express my gratitude to everyone who helped and guided me to complete this thesis work. Firstly, I thankfully acknowledge the opportunity to work with Dr. Adriana Predoi-Cross as a member of her research group. She has been a good professor, and did really a great job in guiding me throughout my entire M.Sc. program. Whenever I had only a minor question, she would instantly pause her work to give precise and clear answers.

I would like to thank my co-supervisor Dr. Michael Gerken for his continuous guidance and support. He has been an excellent mentor throughout the last one year. I would like to give my special thanks to all my committee members, Dr. Brant Billinghurst, Dr. Craig Coburn and Dr. Albert Cross. They have been always supportive and curious about my research work.

I would like to express my gratitude to Dr. V. Malathy Devi (College of William and Mary) and Dr. Mary Ann H. Smith (NASA Langley Research Centre) for all the experimental work that they did for spectra recording. Dr. D. Chris Benner (College of William and Mary) is thanked for allowing us to use the software LABFIT in our study. I also would like to thank Dr. Aziz Ghoufi for the theoretical calculation of the Dicke narrowing parameter.

I am very thankful to Hoimonti Rozario, Ph.D. student, and Abdullah Al Mashwood, a M.Sc. student, in the Department of Physics and Astronomy at our university for their support, and sharing their knowledge with me. Last but not least, I want to give a

special thanks to my beloved family for their love and encouragement, and friends for the inspiration.

Finally, I would like to thank “the Natural Sciences and Engineering Research Council of Canada CREATE” “Advanced Methods, Education and Training in Hyperspectral Science and Technology (AMETHYST)” program for their financial support.

Table of Contents

List of Figures

List of Tables

List of Abbreviations

FTS	Fourier Transform Spectrometer
FTIR	Fourier Transform Infrared
FFT	Fast Fourier Transform
HITRAN	High Resolution Transmission
OPD	Optical Path Difference
ZPD	Zero Path Difference
SDV	Speed Dependent Voigt
DCE	Double Cat's Eye
SNR	Signal-to-Noise Ratio
OFHC	Oxygen-free high-conductivity copper
EPG	Exponential Power Gap Law
ECSA	Energy Correlated Sudden Approximation
IOSA	Infinite-Order Sudden Approximation
MSD	Mean Square Displacement
MFP	Mean Free Path

CHAPTER 1: INTRODUCTION

1.1. Overview

Spectroscopy is a wide branch of science which deals with the interaction of electromagnetic radiation with matter. The qualitative and quantitative interpretation of this interaction provides the fundamental information on molecular structure and molecular dynamics under a given set of physical conditions. Molecular properties such as molecular bond strength, dipole and quadrupole moments can also be obtained from spectroscopic measurements. Infrared (IR) spectroscopy has been implemented to understand the molecular structure of trace components of the planetary atmosphere [1].

In spectroscopy, high-resolution measurements are effective tools used to describe the physical states of molecules through their spectral features (line position, line intensity and others). The term “spectral line” is used to describe an experimentally observed transition while the term “line-shape function” refers to theoretical models used to describe the shapes of spectral lines. The complex behavior of different line-shape parameters shows the necessity of measurements with high resolution. Fourier Transform Spectrometers (FTS) are instruments that have the ability to increase the efficiency of spectroscopic measurements in the laboratory. In this context, Fourier Transform Spectrometers (FTS) and their advantages will be presented in a general way. In addition, the presence of diatomic carbon monoxide (CO) in the Earth and planetary atmospheres will also be discussed in this chapter. Finally, previous laboratory studies for CO line-shape parameters will be summarized at the end of this chapter.

1.2. Fourier Transform Infrared (FTIR) Spectroscopy

In 1800, Frederick William Herschel discovered the infrared (IR) region of the electromagnetic spectrum [2]. In his experimental work, he used a glass prism and blackened thermometers and noticed the presence of a different ray which was not in the range of the visible spectrum and passed through the edge of the red end of the visible spectral range. The first, IR absorption spectra for over 50 compounds were obtained by Abney and Festing in 1882 [3]. In 1903, W.W. Coblentz studied more than a hundred organic and inorganic compounds using IR spectroscopy. In the early age of IR spectroscopy, it was difficult to record IR spectra because scientists had to design and build their own experimental setup. In order to minimize vibrations caused by a variety of noise sources, spectra were usually recorded at night. Furthermore, spectra retrieval processes were time-consuming. Three to four hours were the usual time to record a single IR spectrum. Due to all of these difficulties, spectroscopic scientists tried to invent a more reliable, faster and accurate high-resolution spectral technique in order to record IR spectra.

Today's modern Fourier Transform Infrared (FTIR) spectroscopy would have been impossible without the invention of the Michelson interferometer [4]. Abraham Michelson invented this optical device in 1880. During that time, it was difficult for him to record the interferograms manually, and the calculations for the conversion of an interferogram into a spectrum were also time-consuming. However, the growth of computers helped to perform faster Fourier transform calculations, but there was no algorithm available which could have performed faster calculations. In 1965, J.W. Cooley and J.W. Tukey jointly developed a remarkable algorithm at Bell Labs which is known as "*Cooley-Tukey Algorithm*" or "*Fast Fourier Transform (FFT) Algorithm*" [4]. This algorithm had the ability to perform fast

Fourier Transform using a computer. Due to its fast calculating ability, it is still used as a basis transformation routine in commercial FTIR instruments. The ability to perform the FFT algorithm with a mini-computer lead to an incredible advancement of FTIR spectroscopy. Over the years, FTIR has played an important role in the enhancement of high-resolution spectra both in laboratory studies and remote sensing applications.

Fourier Transform spectroscopy has several significant advantages like:

I. During a single scan, it has the ability to cover the entire infrared wavelength range (0.7-1000 μm) of the incident light which is commonly referred to as the *multiplexing* or *Fellgett advantage* [5].

II. In order to control the optical path difference, a He-Ne light source (monochromatic light) in the spectrometer performs an integrated wavelength calibration with high precision and it is called as the *Connes advantage* [6].

III. It has the ability to encompass the entire intensity of all wavelength components, leading to higher optical throughput, called the *throughput* or *Jacquinot advantage* [7].

Apart from all of these advantages, FTIR spectrometers are mechanically very simple, and provide high signal-to-noise ratios. The optical system of a Michelson interferometer and the overall structure of an FTIR spectrometer will be discussed in chapter three.

1.3. Carbon monoxide (CO) as a diatomic molecule

A diatomic molecule contains two atoms, of either the identical element (homonuclear) or composed of dissimilar elements (heteronuclear). Examples of homonuclear diatomic molecules are H_2, O_2, N_2 whereas examples of common heteronuclear molecules are CO, HCl, NO and others.

Carbon monoxide, C≡O, is a linear diatomic molecule having a carbon and an oxygen atom. The atoms are joined by a triple bond. Due to the difference of electronegativity of the constituting atoms, CO is a polar molecule with a dipole moment 0.11 Debye [8]. The bond length of CO is 112.8 pm and 28.010 g/mol is its molar mass. Its melting point and boiling point are $-205.02\,℃$ (68.13 K) and $-191.5\,℃$ (81.6 K), respectively.

In 1776, a chemical reaction of zinc oxide with coke done by the French chemist De Lassone was considered as the first ever discovery of CO, but unfortunately he named it wrongly as hydrogen. Later in 1800, the Scottish chemist William Cumberland Cruikshank noticed that this molecule was actually a combination of carbon and oxygen. CO is a very toxic chemical compound and in 1846, its toxic properties were first tested on dogs by the French scientist Claude Bernard [9].

Diatomic molecules have $D_{\infty h}$ or $C_{\infty v}$ point symmetry. The molecular structure of CO does not have a center of symmetry; therefore, it belongs to $C_{\infty v}$ point group having one vibrational mode ($3N-5$ with N=2).

1.4. Carbon Monoxide (CO) as a trace constituents of planetary atmosphere

Carbon monoxide (CO) is a greenhouse gas, having contributions to the carbon cycle and global warming. As a trace constituent, CO is present in planetary atmospheres, stellar atmospheres, and the interstellar medium. Atmospheric oxidation of alkanes or organic molecules including methane results in the emission of carbon monoxide into atmosphere. In planetary atmospheres, CO is usually produced by the oxidation of organic compounds occurring during the combustion process of biomass, fossil fuels, and

vegetation [10]. In addition, oxidation of CO by tropospheric hydroxyl radical (OH) leads to the production of a significant amount of tropospheric ozone (O_3) as well. However, two months is the average lifetime of atmospheric CO, which is quite short and throughout the globe its sources are not evenly distributed [11]. Eventually, these variations lead to an unstable concentration of CO spread around the globe. Hence, several ground-based, balloon- and satellite-based remote-sensing missions have been employed during the past couple of decades to monitor the atmospheric concentration of CO. Due to all of these facts it is considered as an important molecule in the spectroscopic community.

Connes *et al*. [12] studied the high-resolution spectra of different planetary atmospheres including Jupiter, Saturn, Venus, and Mars. The authors used their Fourier-transform spectrometer (FTS) and are considered as pioneers for their remarkable observation of those planetary spectra for the first time. Ground-based 5 μm CO spectra were retrieved with the help of a Connes-types FT spectrometer, having a spectral apodized resolution of 0.20 cm^{-1}, located at McDonald Observatory (Texas, USA), and thus confirmed the presence of CO in the lower atmosphere of Jupiter [13]. In 1985 and 1986, IR spectra of the CO bands of Saturn were observed in the 4.7 μm spectral region by a Fabry-Perot spectrometer located at the Astronomical Observatory on Mauna Kea, Hawaii [14]. This experiment was significant because it was the first detection of CO in Saturn's atmosphere based on the fundamental band (0→1) and for that the spectral resolution of the spectrometer was 0.15 cm^{-1} at 2100 cm^{-1} (≈4.7 μm). By using an infrared technique, the presence of CO on Mars was first observed by Kaplan *et al.* [15]. Furthermore, CO spectra having 115 GHz ro-vibrational transitions were observed in the atmosphere of Mars [16]. High-resolution interferometric CO spectral lines in the first overtone band (0→2) of Venus's atmosphere were first observed by P. Connes *et al.* [17].

1.5. Motivation for this study

The molecular constituents of the Earth and other planets are accurately quantified with the help of molecular spectroscopic techniques where the instruments are usually mounted on ground-based telescopes, spacecrafts and aircraft platforms in order to record the spectra. With the enhancement of modern technology, the spectral resolution of Earth and planetary atmospheric spectra have been developed significantly and the interpretation of these spectra are only possible when one could analyze the spectral line parameters accurately.

In order to obtain precise atmospheric line-shape profiles of carbon monoxide (CO), NASA has launched several satellite missions (2013-2016) such as the *GEO stationary Coastal and Air Pollution Events* (GEO-CAPE) mission and the *Active Sensing of CO_2 Emissions over Nights, Days, and Seasons* (ASCENDS) in the 4.6- μm spectral region [18]. The measurement of accurate CO line-shape parameters over a range of temperatures is of high importance. The spectroscopic database HITRAN has extensive information on CO. However, the parameters of CO which are already noted in HITRAN do not meet the desired accuracy of 1% or better required for 4.6- μm spectral region. Moreover, data for less-abundant isotopologues and for weaker transitions are still missing.

Tropospheric carbon monoxide in the 0→1 band, can be monitored by means of spectroscopic remote sensing in the 4.6- μm spectral range. This particular spectral range was chosen because of the sun's high output coupled with the small ground level thermal emission. Furthermore, measurements of accurate line-shape parameters for $^{12}C^{16}O$ in the fundamental band are important because $^{12}C^{16}O$ is the most abundant isotopologue of CO. My spectroscopic studies will accurately determine line strengths (intensities), self- and

air-pressure-induced line shifts and the self- and air-broadened broadening coefficients for the fundamental band (0→1) of $^{12}C^{16}O$ at room temperature and at other temperatures. Other parameters such as line mixing (line coupling), narrowing effect of absorption lines are also considered in the data fitting procedure.

1.6. Summary of previous studies

Spectral line-shape parameters of CO for high-resolution spectroscopic studies have been done by different researchers and reported in publications. One of the earlier studies of carbon monoxide line-shape parameters was carried out by T. Nakazawa and M. Tanaka [19] who investigated the intensities (line strengths) and the self-broadened half-widths of CO, as well as O_2-, N_2- and CO_2-broadened half-widths in the 0→1 band at 300 K. Later on, Devi *et al*. [20] studied the self- and H_2-broadened line width and shift coefficients for $^{12}C^{16}O$ in the 0→2 band. They investigated 48 spectral lines, and all of them were recorded at National Solar Observatory on Kitt Peak, Arizona with the McMath-Pierce Fourier transform spectrometer.

Very recently published papers [18, 21] based on the 0→2 band transition of three most abundant CO isotopologues ($^{12}C^{16}O$, $^{13}C^{16}O$, $^{12}C^{18}O$) reported accurate results for air-broadening widths, pressure-induced air-shift, and their temperature dependences. However, the updated results of air- and self -broadened widths in the 0→1 and 0→2 bands of $^{12}C^{16}O$ are included in HITRAN [22-24] just based on the study by Zou and Varanasi [25]. In their study, eight spectra were obtained using the Fourier Transform Spectrometer (FTS) Bruker IFS 120HR at 296 K and they analyzed them with a multi-spectral-line fitting technique. For transitions *m* index between -24 and 26 in the 0→1 band, they reported the pressure induced air-broadening and shifts. However, for the 0→2 band, both self- and air-

pressure-induced broadening and shift coefficients, and their temperature dependences along with uncertainties were taken into account for the same range. The authors did not consider line-mixing effects while analyzing the spectra with the Voigt profile. L. Regalia-Jarlot *et al.* [26] have studied the measurement of H_2- and air-broadened line widths and shift coefficients for the 0→1 band of $^{12}C^{16}O$. They also presented their results for self- and H_2-broadened line parameters for the 0→2 band as well.

J.W. Brault *et al.* [27] used high-resolution Fourier-transform spectra to measure the line intensities, self-broadening coefficients and self-shifts of $^{12}C^{16}O$ in the 0→2 band. In order to minimize the noise level, the authors used a simultaneous fitting technique where the pressure ranges for all the spectra were in the range of 200 to 600 Torr. Also, they have retrieved the speed-dependent broadening coefficients by considering line-mixing and Dicke-narrowing effects. These two effects occur due to the transformation of line-shapes at a different pressure regime. As a result, their line-shape studies showed 1% deviation from the usual Voigt profile.

Broadening and line-shift coefficients along with their temperature dependences for both pure and helium-mixed CO have already been measured by A.W. Mantz *et al.* [28] for the 0→1 band. Spectra were retrieved using the McMath-Pierce Fourier transform spectrometer (FTS), and both our and their spectra were retrieved from the same spectrometer which is situated at the National Solar Observatory on Kitt Peak, Arizona. By using a detailed analysis, measurements of the line-mixing coefficients of CO broadened by He in the weak overlapping spectral regime of 0→1 and 0→2 bands have been published by Thibault *et al.* [29]. No studies of line-mixing coefficients for air-broadened carbon monoxide in the 0→1 band were reported previously. In addition, comparable

measurements of self- and air-broadened widths, self- and air-shift and their temperature dependences for different line-shape profiles like Voigt, Speed-Dependent Voigt and Rautian profile for 0→1 bands have not been reported.

Boissoles *et al*. [30] have calculated the theoretical line-mixing coefficients in the 0→1 band of CO broadened by He, and compared them with overlapping weak spectral lines obtained for temperature ranges between 292 to 78 K. In order to do this, they used the Energy Corrected Sudden Approximation (ECSA) and Infinite Order Sudden Approximation (IOSA) for the calculation of broadening coefficients and line coupling coefficients.

Predoi-Cross *et al*. [31] theoretically predicted and experimentally measured the broadening, shifting and line-mixing coefficients of self-broadened CO and CO broadened by nitrogen in the 0→2 band. In their study, the retrieved spectra were obtained at room temperature and they used the Energy Corrected Sudden (ECS) approximation for the calculation of line mixing. Their results emphasised that other than line mixing there might be other effects which could also contribute to line asymmetry. A temperature-dependent effect for 0→1 band of CO mixed with N_2 was reported by Predoi-Cross *et al*. [10]. The authors measured the line-broadening coefficients of CO broadened by N_2 at 348 K and compared these results with the room-temperature broadening coefficients. They used a temperature scaling law, in order to combine, both the pressure-broadening coefficients at two different temperatures. By using a scaling law, they determined the temperature-dependent coefficients or exponents. In their investigation of temperature exponent, they used Lorentz, Voigt and hard-collision models. Line-mixing parameters at 348 and 310 K were also reported.

CHAPTER 2: THEORETICAL BACKGROUND

2.1. Overview

In molecular spectroscopy, phenomena such as absorption, emission and scattering of light occur when the light interacts with the gas molecules, and due to transitions between energy levels, spectral lines appear. The aim of this chapter is to discuss the ro-vibrational (rotational and vibrational) spectroscopy for diatomic molecules. Electromagnetic radiation and its interaction with matter will be discussed at the beginning. This chapter will cover the discussion of vibrational bands of interest for pure rotational, pure vibrational and ro-vibrational spectra in terms of quantum mechanical perspective.

Furthermore, I will discuss the fundamentals of absorption spectroscopy along with the Beer-Lambert Law and present different line-shape models which have been implemented in molecular spectroscopy in order to describe accurate absorption features. How temperature affects the line-shape parameters will also be described in this chapter. Finally, the basic concepts of the line-mixing processes and theoretical approaches from which line-mixing coefficients are usually calculated will be covered at the end of this chapter. Most of the sections of this chapter is based on the "Modern Spectroscopy" book written by J. Michael Hollas [32], and Dr. Chad Povey's Ph.D. thesis [33].

2.2. Principles of Spectroscopy

2.2.1. Electromagnetic radiation and its interaction with matter

Electromagnetic radiation or light propagates as a transverse wave at a finite speed of 3×10^8 m/s in vacuum. The electromagnetic wave is composed by the strength of electric $\vec{E}$ and magnetic $\vec{H}$ fields [32]. Both of these components will travel in the direction away

from the source and are always at a right angle to each other. Propagation of an electromagnetic wave in the x-direction is shown in Figure 2.1.

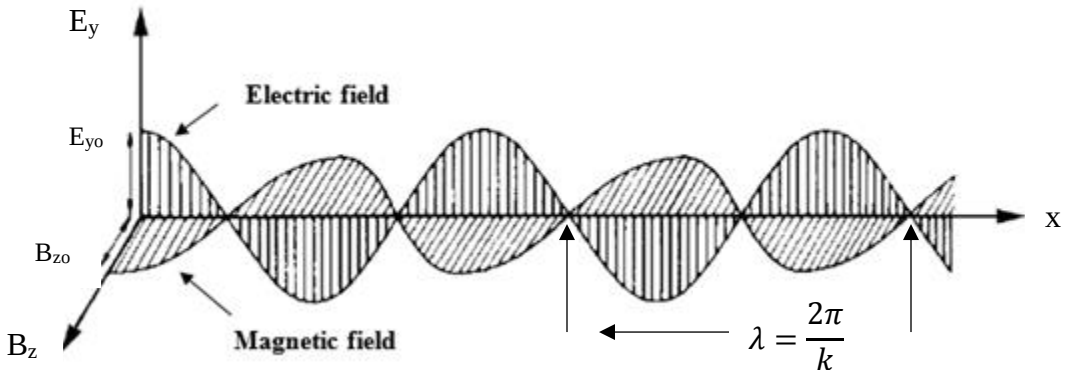

Figure 2.1: Electromagnetic radiation moving along the x direction (adopted from source, p: 28) [32].

The propagating wave can be described by the following equations:

$$E_y = E_{yo}\, cos(2\pi vt - kx) \tag{2.1}$$

$$B_z = B_{zo}\, cos(2\pi vt - kx) \tag{2.2}$$

where E_{yo} and B_{zo} are the maximum amplitudes of the electric and magnetic fields, $2\pi v$ is the angular frequency of the oscillating fields, k is the wavenumber, t is time and x is the position. Since the amplitude of both fields are showing periodic cosine waves having same frequency, meaning that they are in-phase, and the wavenumber (k) will be identical for each component. However, the frequency v can cover a broad spectral range from radio waves to gamma rays. Due to the inverse relationship between frequency and wavelength (λ), the order of spectral regimes are reversed in terms of wavelength scale.

How the light will interact with atoms or molecules depends on the frequency of the light, the strength of its electromagnetic field and the properties of the matter itself. In order to understand their interactions in terms of quantum mechanics, we can assume two energy states m and n of an atom having eigenenergies E_m and E_n, respectively. It is

supposed that both states are stationary as long as they are independent of time. Three types of interactions may occur while electromagnetic radiation interacts with a two-energy-states systems. During the interaction, a change of energy between the energy states will occur. Mathematically, this change of energy (ΔE) can be written as:

$$\Delta E = E_m - E_n = h\upsilon_{mn} = hc\tilde{\upsilon}_{mn} \quad (2.3)$$

Here h is Planck's constant (6.62606896×10^{-34} J.s) and υ_{mn} is the frequency of the incident light. c denotes the speed of light, and $\tilde{\upsilon}_{mn}$ is the wavenumber (m^{-1}) of the transition. The above-mentioned three processes which are responsible for changes of energy in the system are described below:

I. Induced absorption: In this process, an incident photon having energy $h\upsilon$ is absorbed by the atom M of the molecular system and excites it from lower energy state m to upper energy level n.

$$M + hc\tilde{\upsilon}_{mn} \rightarrow M^* \quad (2.4)$$

II. Spontaneous emission: In this case, atom M^* in the upper energy state (n) spontaneously drops into the lower state(m) by emitting a photon.

$$M^* \rightarrow M + hc\tilde{\upsilon}_{mn} \quad (2.5)$$

III. Stimulated emission: When the incident photon of frequency υ interacts with the excited atom (M^*) and de-excites it from the energy level m to the energy level n , then a second photon having exactly the same frequency will release. In this process, the second photon will be identical to the incident photon in terms of their phase, frequency, polarization and direction of propagation [32].

$$M^* + hc\tilde{\upsilon}_{mn} \rightarrow M + 2hc\tilde{\upsilon}_{mn} \quad (2.6)$$

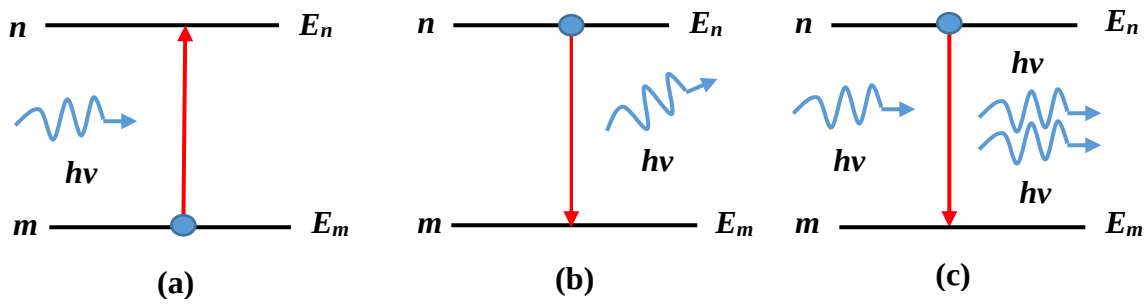

Figure 2.2: Three possible types of interaction between the electromagnetic radiation and the electron in the energy states m and n. (a) induced absorption, (b) spontaneous emission, (c) stimulated emission [34].

If we consider N_n and N_m as the populations of states n and m, respectively, then due to the induced absorption, the rate of change of population of state n can be written as:

$$\frac{dN_n}{dt} = N_m B_{mn} \rho(\tilde{\nu}), \tag{2.7}$$

where B_{mn} (s^{-1}) is the Einstein B-coefficient which defines the probability of absorption of light during the transition. The spectral radiation density $\rho(\tilde{\nu})$, is shown by the following equation:

$$\rho(\tilde{\nu}) = \frac{8\pi hc\tilde{\nu}^3}{\exp\left(\frac{hc\tilde{\nu}}{k_B T}\right)-1} \tag{2.8}$$

Where k_B is the Boltzmann constant ($1.38064852 \times 10^{-23}$ m^2 kg s^{-2} K^{-1}). The changes of population N_n after induced emission is given by:

$$\frac{dN_n}{dt} = -N_n B_{nm} \rho(\tilde{\nu}) \tag{2.9}$$

where B_{nm} is the Einstein coefficient for induced emission process and is equivalent to B_{mn}. For spontaneous emission, it can be written as:

$$\frac{dN_n}{dt} = -N_n A_{nm} \tag{2.10}$$

where A_{nm} is the Einstein -A coefficient. As it is a spontaneous process, the spectral radiation density $\rho(\tilde{\nu})$ is absent in the above equation. At equilibrium, we have:

$$\frac{dN_n}{dt} = (N_n - N_m)\, B_{nm}\rho(\tilde{v}) - N_n A_{nm} = 0 \tag{2.11}$$

Here N_n and N_m are related to the degrees of degeneracy of lower state n and higher state m, respectively. By using the Boltzmann distribution law, their relationship can be written as:

$$\frac{N_n}{N_m} = \frac{g_n}{g_m}\exp(-\frac{\Delta E}{k_B T}) = \exp(-\frac{\Delta E}{k_B T}) \tag{2.12}$$

In equation (2.12) g_n and g_m are the corresponding degrees of degeneracy of states n and m. It is supposed that at equilibrium g_n and g_m are the same. Using the above relationship and putting the expression of $\rho(\tilde{v})$, mentioned in equation 2.8 into equation 2.11, the final relationship between A_{nm} and B_{nm} would be:

$$A_{nm} = 8\pi hc\tilde{v}^3 B_{nm} \tag{2.13}$$

The three emission and absorption processes are the fundamental aspects of interactions between the electromagnetic radiation and matter. The pair of states are described as electronic states where only the electrons of an atom interact with the incident light. In molecular physics, according to the Born-Oppenheimer approximation, the motion of atomic nuclei and electrons in a molecular system can be separated due to their dissimilarity in mass. Electrons in the atomic orbit can move much faster than the vibrating nuclei.

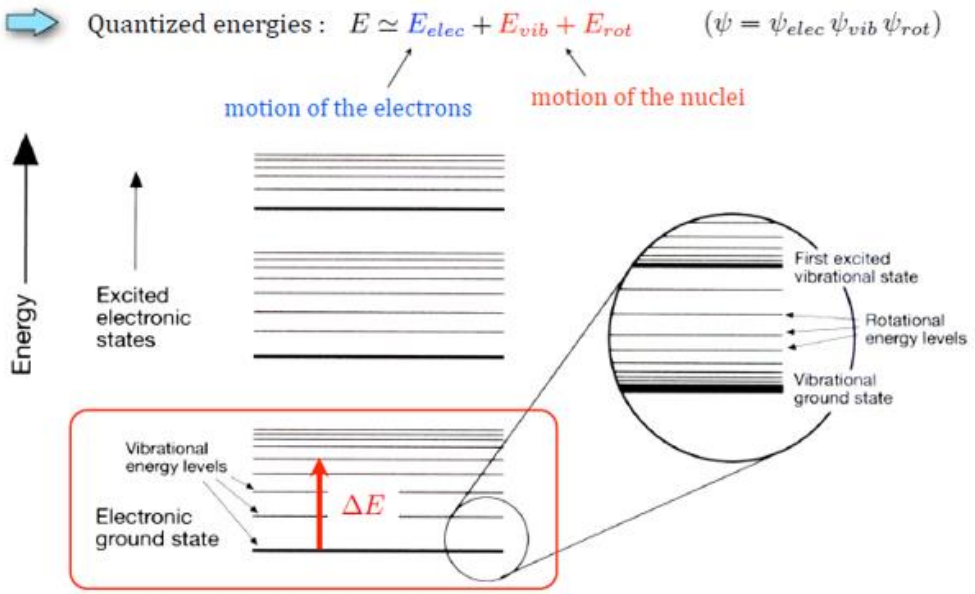

Figure 2.3: Molecular motions in different energy states [courtesy: Dr. J. Vander Auwera (ULB)].

Mathematically, the total wavefunction of the molecule will be divided into nuclear (vibrational and rotational) and electronic components. Furthermore, the energy components of the nuclei and the electrons are also considered separately.

$$|\Psi_{total}\rangle = |\psi_{electronic}\rangle|\psi_{vibrational}\rangle|\psi_{rotational}\rangle \tag{2.14}$$

$$E_{total} = E_{electronic} + E_{vibrational} + E_{rotational} \tag{2.15}$$

Photons in the infrared region can cause vibrations of a molecule i.e. excitation to many possible vibrational levels within a single electronic state. In contrast, light in the microwave range can neither excite the vibrational states nor the electrons of the molecules. Microwave radiation can, however, excite rotational states.

2.3. Pure vibration

The motion of a molecule is usually described by its degrees of freedom. In a 3-dimensional space, an N-atomic molecule will have 3N degrees of freedom. Apart from

translational motion, rotational and vibrational motion of molecules are also taken into account in order to get comprehensive knowledge about molecular motion. Due to the rotational and the translational motion of the atoms, the degrees of freedom around the x-, y- and z-axes would be 6 and the remaining 3N-6 degrees represent the vibrational motion. Hence, 3N-6 degrees of freedom would be the number of vibrational mode of a non-linear polyatomic molecule.

For a linear molecule, 3N-5 would be the number of normal modes of vibration because rotating along its own axis will not change the molecule. In a single mode of vibration atoms can vibrate simultaneously with the same frequency and phase. In general, all of these normal modes belong to a single normal coordinate. However, each of these vibrational modes is independent under this coordinate but sometimes it is also possible to have the same frequency for two or more vibrational modes. In that case, atoms of each of these modes vibrate at the same frequency and the modes are referred to as degenerate modes.

The time-independent Schrödinger equation provides the energy value and the frequency of each of the normal modes.

$$H|\psi\rangle = E|\psi\rangle \tag{2.16}$$

Here H is the Hamiltonian which corresponds the total energy of the system. E and $|\psi\rangle$ are the eigenenergies and the wavefunctions, respectively. The separation of the total wavefunction mentioned in equation 2.14 is just an approximation but still effective for the analysis of the vibrational and rotational motion of any molecule.

2.3.1. Harmonic Oscillator

Let us consider a diatomic molecule vibrating similar to a harmonic oscillator. The solutions of the above Schrödinger equation gives the eigenenergies of the harmonic oscillator as follows:

$$E(v) = hv\ (v + \tfrac{1}{2}) \tag{2.17}$$

where v is the vibrational quantum number (v = 0, 1, 2…) and υ is the frequency of the vibrating molecule. Therefore, each of the energy states are equally spaced. Mathematically, the frequency υ is interconnected with the reduced mass [$\mu = \frac{m_1 m_2}{m_1 + m_2}$] of the two atoms and k is the force constant and it can be expressed as:

$$\upsilon = \frac{1}{2\pi} \left(\frac{k}{\mu}\right)^{1/2} \tag{2.18}$$

The change in the dipole moment ($\vec{\mu}$) of two energy states having vibrational wave functions ψ'_υ and ψ''_υ is related by the vibrational transition moment $\overrightarrow{R_v}$ [32]:

$$\overrightarrow{R_v} = \int \psi'^{*}_\upsilon \vec{\mu}\ \psi''_\upsilon\ dx \tag{2.19}$$

Above, the position x (equal to $r - r_e$) is the change of intermolecular distance from equilibrium. r_e is the position at equilibrium. Homonuclear diatomic molecules (H_2, O_2 etc.) do not have permanent dipole moments ($\vec{\mu} = 0$) and a vibration does not generate a dipole moment. As a consequence, $\overrightarrow{R_v}$ would be zero and vibrational transitions will not appear. In contrast, a heteronuclear diatomic molecule has a non-zero dipole moment that varies with x.

The variation of dipole moment with respect to x can be expressed as a Taylor series expansion with the equilibrium configuration denoted by the superscript 'e'.

$$\vec{\mu} = \vec{\mu}_e + \left(\frac{d\vec{\mu}}{dx}\right)_e x + \frac{1}{2!} \left(\frac{d^2\vec{\mu}}{dx^2}\right)_e x^2 + \cdots \tag{2.20}$$

Putting the value of μ into equation (2.19), the vibrational transition moment R_v becomes

$$\overrightarrow{R_v} = \vec{\mu}_e \int \psi_v'^{*}\, \psi_v''\, dx + \left(\frac{d\vec{\mu}_e}{dx}\right)_e \int \psi_v'^{*}\, x\, \psi_v''\, dx + \cdots \quad (2.21)$$

Since, both wavefunctions are orthogonal to each other ($\int \psi_v'^{*}\, \psi_v''\, dx = 0$) and are eigenfunctions of the same Hamiltonian, equation (2.21) turns into a more simplified form after neglecting the higher order terms.

$$\overrightarrow{R_v} = \left(\frac{d\vec{\mu}}{dx}\right)_e \int \psi_v'^{*}\, x\, \psi_v''\, dx \quad (2.22)$$

The first term of the above equation implies a non-zero change of dipole moment under the certain condition $\Delta v = \pm 1$. Δv is the difference of lower and upper energies in terms of vibrational quantum number. This condition is usually referred to as the *vibrational section rule*. Vibrational transitions of a harmonic oscillator are only possible when they satisfy this condition.

2.3.2. The Anharmonic Oscillator

The concept of harmonic oscillator of a diatomic molecule is only applicable when the intermolecular distance is not far away from the equilibrium distance. But, when the intermolecular distance of the diatomic molecule is large enough from its equilibrium position, the assumption of harmonic motion of the molecule becomes invalid and the motion is anharmonic. In that case, the molecule dissociates into two neutral atoms where both atoms move independently without influencing each other. Typically, harmonic oscillator does not give the details information about the vibrational structure of real molecules. In order to expain the vibrational structure of the molecule, anharmonic oscillator can be used as an ideal model. Figure 2.4 shows a comparison between the potential energy (V) of an anharmonic oscillator and a harmonic oscillator.

Due to the anharmonicity of molecular vibrations, the selection rule for vibrational transitions is relaxed from $\Delta v = \pm 1$ to $\Delta v = \pm 1, \pm 2, \pm 3, ...$,where $\pm 2, \pm 3$ represent weak overtone transitions. Furthermore, anharmonic motion also introduces a separate energy spacing which is dependent on the vibrational quantum number. In terms of wavenumber units, the eigenvalue $G(v)$ for anharmonic motion can be expressed by the following power series in $\left(v + \frac{1}{2}\right)$

$$G(v) = \tilde{v}_e \left(v + \frac{1}{2}\right) - \tilde{v}_e x_e \left(v + \frac{1}{2}\right)^2 + \tilde{v}_e y_e \left(v + \frac{1}{2}\right)^3 + \cdots \quad (2.23)$$

where $\tilde{v}_e x_e, \tilde{v}_e y_e$ are the anharmonic constants for 2nd and 3rd order polynomial. The energy associated with vibration of a diatomic molecule can be derived by the above equation.

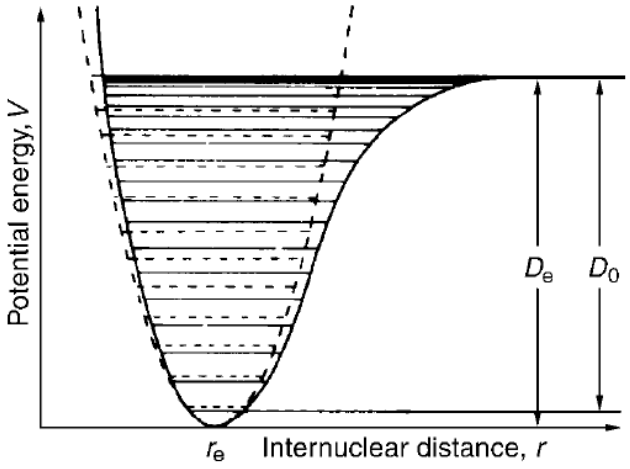

Figure 2.4: Potential energy curve of a diatomic molecule moving as a harmonic (dashed curve) and an anharmonic (solid curve) oscillator where the dashed and the solid lines representing energy states for both of the motions respectively. D_0 is the dissociation energy with respect the ground state, whereas D_e represents the dissociation energy measured from the equilibrium potential energy level (adopted from source, p: 143)[32].

2.4. Pure Rotation

2.4.1. The rigid rotor

The rigid rotor is a useful mechanical model for explaining the rotational motion of a diatomic molecule in which the bond linking the nuclei is considered as a rigid, weightless rod. Considering the model of a rigid rotor, rotation of a heteronuclear diatomic molecule is shown in Figure 2.5.

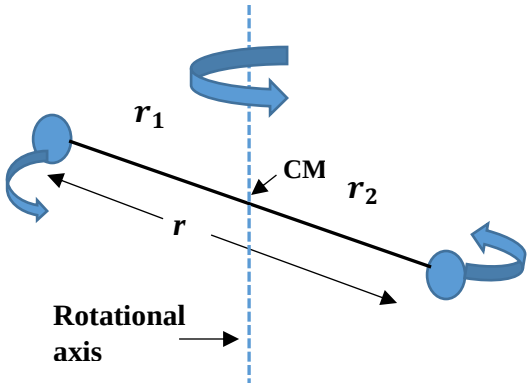

Figure 2.5: Rotation of a heteronuclear diatomic through the center of mass(CM) and about the axis perpendicular to the bond [35].

In case of rotational transitions, the energy term E_r of a diatomic rigid rotor can be obtained from the solution of the Schrödinger equation for a rigid rotor:

$$E_r = \frac{h^2}{8\pi^2 I} J(J+1) \tag{2.24}$$

where J is the rotational quantum number ($J = 0, 1, 2, ..$), I is the moment of inertia (equal to μr^2, where μ is the reduced mass of the interacting atoms and r is the intermolecular distance). In reality, it is not energy but frequency that is measured experimentally. In wavenumber terms equation (2.24) can be expressed as:

$$F(J) = \frac{E_r}{hc} = \frac{h}{8\pi^2 cI} J(J+1) = BJ(J+1) \tag{2.25}$$

where B is the rotational constant which has an inverse relationship with the moment of inertia. In spectroscopy, the determination of B is considered as a strong structural technique that basically provides the internuclear distances. Rotational transitions which are allowed or forbidden are determined by selection rules. For a rigid rotor, the selection rule is:

$$\Delta J = \pm 1 \tag{2.26}$$

Here, ΔJ is $J' - J''$, where J' is the rotational quantum number of upper energy state and J'' symbolizes the rotational quantum number of lower energy state. Conventionally, $\Delta J = +1$ and $\Delta J = -1$ represent absorption and emission, respectively. Though, $\Delta J = +1$ is applicable for both of the cases. The radiation absorbed by the diatomic molecule can be expressed in terms of wavenumber as follows:

$$\tilde{\nu}_{J+1\leftarrow J} = F(J') - F(J'') = B(J+1)(J+2) - BJ(J+1) = 2B(J+1) \tag{2.27}$$

It is clear from the above equation that the spacing of adjacent rotational transitions is multiple of $2B$. For example, Figure 2.6 shows a set of relative populations ($\frac{N_j}{N_o}$), transition wavenumbers ($\tilde{\nu}$) of CO.

2.4.2. Centrifugal distortion

In reality, a molecule does not behave like a perfectly rigid rotor. As the molecule starts to rotate from lower angular momentum to higher, the atoms begin to separate from each other due to the effect of centrifugal forces. As a consequence, it will change the value of the moment of inertia slightly. Furthermore, transition spacing between the energy states will decrease slightly with the increase of rotational quantum number J. An additional

centrifugal distortion term (D) should be included in equation (2.27) in order to consider the small changes in transition spacing for higher J values.

$$F(J) = BJ(J+1) - D[J(J+1)]^2 \tag{2.28}$$

For a diatomic molecule, the centrifugal constant D is always positive. The modified transition wavenumber equation should be written as:

$$\tilde{\nu}_{J+1\leftarrow J} = F(J+1) - F(J) = 2B(J+1) - 4D(J+1)^3 \tag{2.29}$$

The value of D is much smaller than the value of rotational constant B. The influence of D is only significant for larger J values and therefore the energy spacing between such transitions reduces rapidly.

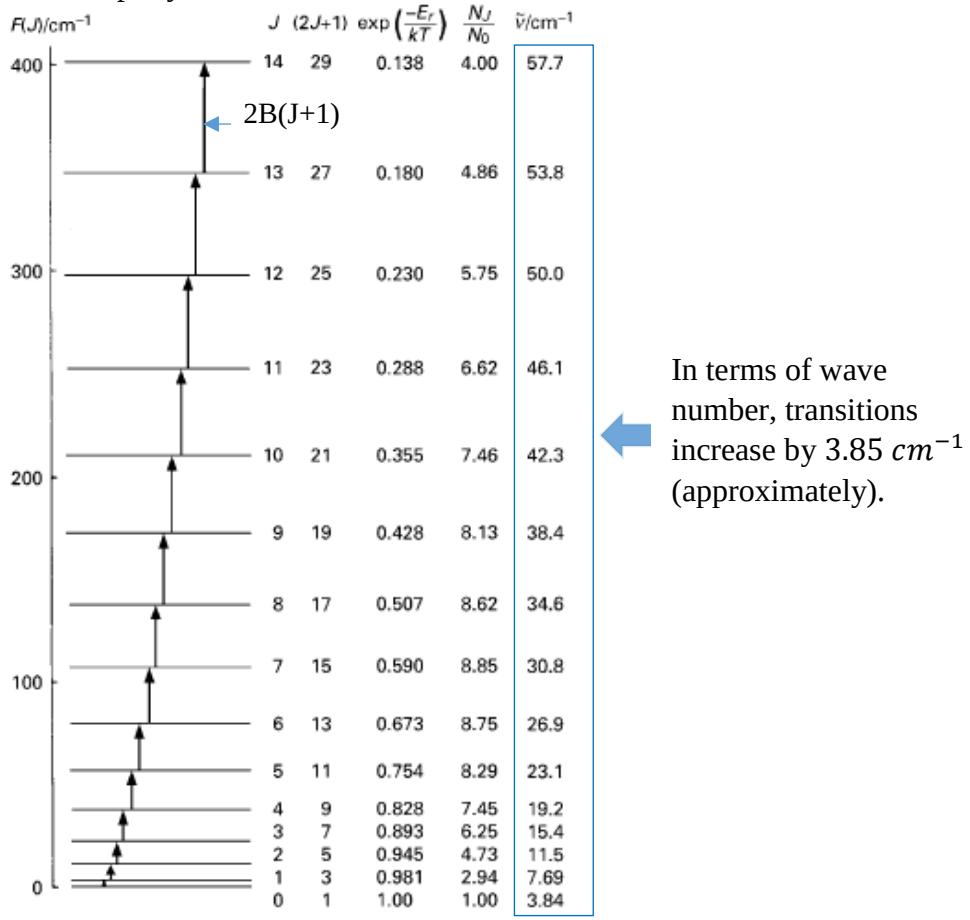

Figure 2.6: A set of rotation transitions for carbon monoxide molecule (adopted from source, p: 107)[32].

2.5. Rotation-vibration

Due to the change in bond length during the molecular motion, rotational transitions of a molecule can be affected by its vibrational transition. Consequently, infrared spectra are the simultaneous excitation of both rotational and vibration motions. This coupling of two different transitions introduces vibrational dependency terms and requires a slight modification in equation 2.28. Therefore, the term values of equation 2.28 and 2.29 can be expressed as:

$$F_v(J) = B_v J(J+1) - D_v[J(J+1)]^2 \tag{2.30}$$

$$\tilde{\nu}_{J+1\leftarrow J} = 2B_v(J+1) - 4D_v(J+1)^3 \tag{2.31}$$

Mathematically, the vibrational dependency of B and D.

$$B_v = B_e - \alpha\,(v+\tfrac{1}{2}) \tag{2.32}$$

$$D_v = D_e - \beta\,(v+\tfrac{1}{2}) \tag{2.33}$$

Here, B_e and D_e are defined for the molecular equilibrium configuration. α and β are the vibration-rotation interaction constants having very small value as compared to B_e and D_e, respectively. As far as vibrational dependency is concerned, the centrifugal distortion constant (D_v) does not have a significant impact on rotation-vibration transitions as the rotational constant does.

2.6. Bands of linear molecules

To study the rotational-vibrational bands of any linear molecule is always difficult due to the complex structure of the corresponding spectra. In order to describe the band structure of a linear molecule, the molecular symmetry of that molecule as well as its point

group should be taken into account. Linear centro-symmetric molecules ($i.e. CO_2$, C_2H_2) belong to the $D_{\infty h}$ point group whereas heteronuclear diatomic linear molecule ($i.e. CO, HCl$) belong to the $C_{\infty v}$ point group without having inversion centre.

According to the character table of $C_{\infty v}$, the allowed transitions from lower vibrational state to upper level followed by the selection rule would be:

$$\Sigma^+ \leftarrow \Sigma^+ \text{ and } \Pi \leftarrow \Sigma^+ \tag{2.34}$$

where Σ is the vibrational states of the diatomic molecule having no angular momentum and this kind of band is commonly referred to as $\Sigma^+ \leftarrow \Sigma^+$ band. For such a diatomic molecule, all types of Σ rotation-vibration energy states can therefore be written as:

$$\frac{E(v,J)}{hc} = F(v,J) = v_v + B_v(J+1) - D_v J^2(J+1)^2 \tag{2.36}$$

Here, B_v is the rotational constant. v_v and D_v are the vibrational energy and centrifugal distortion constant of state v , respectively. Depending on vibrational angular momentum, molecular bands are divided into two categories: *parallel* and *perpendicular*. Parallel bands usually occur when the vibrational angular momentum is zero in the lower vibrational state l = 0, and the vibrational angular momentum does not change during the transition, i.e. Δl = 0. Furthermore, the dipole moment also changes parallel along the molecular axis. Selection rules for such type of bands are $\Delta J = \pm 1$, which define the branches of the transition. In quantum mechanics, branches of transition for a rigid rotor are usually referred as P, and R. According to the above section rules for parallel bands, two allowed transitions are $\Delta J = -1$ and $\Delta J = +1$, and they are basically representing P- and R-branches, respectively. In terms of the wavenumber equation, in a rigid rotor the frequencies of such transitions can be expressed as:

$$\tilde{\nu}_p = \tilde{\nu}_o - (B'_v + B''_v)J + (B'_v - B''_v)J^2 \quad (2.37)$$

$$\tilde{\nu}_R = \tilde{\nu}_o + 2B'_v - (3B'_v + B''_v)J + (B'_v - B''_v)J^2 \quad (2.38)$$

where $\tilde{\nu}_o$ represents the pure-rotation vibration transition wavenumber. B'_v and B''_v are the rotational constants of the upper and lower state, respectively. Equation (2.37) represents the P-branch transitions where $J = 1, 2, 3, 4, \ldots$ meanwhile, $J = 0, 1, 2, 3, \ldots$ would be the values for the R-branch presented in equation (2.38). In the rigid rotor limit, it is possible to generalize equation (2.37) and (2.38) by introducing an expanding term *m*. For P- and R-branch transitions the modified form of equation (2.37) and (2.38) would be:

$$\tilde{\nu}_m = \tilde{\nu}_o + (B'_v + B''_v)m + (B'_v - B''_v)m^2 \quad (2.39)$$

where $m = -J$ for P branch transitions, and $m = J + 1$ for R branch transitions.

Perpendicular bands are considered as the second type of bands which usually occur due to changes of dipole moment perpendicularly with respect to the molecular axis. In addition, perpendicular bands arise due to the excitation of the bending vibration of a polyatomic molecule. This bending vibration leads to change in the angular momentum ($\Delta l = \pm 1$) in the vibrational states. These types of bands are normally known as $\Pi \leftarrow \Sigma$ bands in which $l'' = 0$ and $l = \pm 1$. According to selection rules, allowed transitions for such types of bands are $\Delta J = 0, \pm 1$. Keeping the same transitions in the P and R branches, perpendicular bands introduce a new branch which lies in between of these two branches. This new branch is known as the Q branch where $\Delta J = 0$. Bands having transitions from the vibrational ground state to the higher energy state with ν = 1 and following the two mentioned selection rules are called fundamental bands. However, when the lower vibrational state $l \neq 0$ but $\Delta l = 0$, then the bands for these types of transitions are identified

as $\Pi \leftarrow \Pi$, $\Delta \leftarrow \Delta$ bands. Allowed transitions for these bands are exactly the same as the perpendicular bands, hence $\Delta J = 0, \pm 1$. Though, this time the Q branch would be significantly weaker than the perpendicular band.

2.7. Rotational-vibration band of CO

Carbon monoxide (CO) is a heteronuclear diatomic molecule with $C_{\infty v}$ symmetry. It has one $(3N - 5 = 3 \times 2 - 5 = 1)$ vibrational mode which is a stretching mode. CO possesses only the v_1 stretching mode in its chemical bond having vibrational angular momentum of $l = 0$. Since there are no bending modes in CO, it will not have any perpendicular bands. It has only a parallel $\Sigma \leftarrow \Sigma$ band which has only P and R branches.

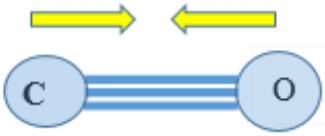

Figure 2.7: Stretching mode of CO.

2.8. Absorption spectroscopy

2.8.1. Beer-Lambert law

Absorption spectroscopy is a subdivision of spectroscopy where the light source, absorption gas cell, and a spectrometer are the basic components for retrieving spectroscopic properties from any gas molecule. A schematic view of absorption spectroscopy is shown in Figure 2.8. Electromagnetic radiation passes through the gas cell which contains the molecules of interest. After interacting with gas molecules, the transmitted light passes through the spectrometer and finally reaches a detector.

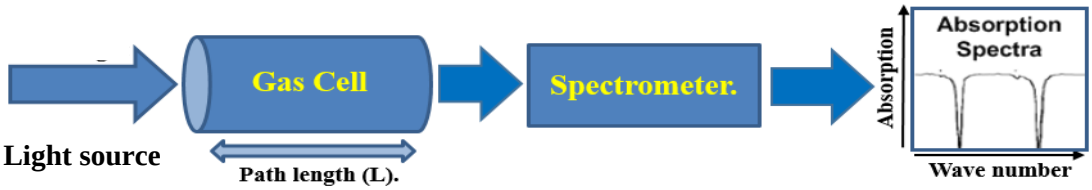

Figure 2.8: A schematic view of absorption spectroscopy.

The relationship between the intensity of light before and after passing through the gas cell is considered as a fingerprint for the spectral analysis of the inserted gas. The radiation absorbed by the gas molecule is quantified by a well-known law called Beer-Lambert law. Mathematically, it can be derived as:

$$I_1 = I_0 e^{-\alpha C L} \tag{2.40}$$

where $I_1$and I_0 are the transmitted and incident intensity of light, respectively. α is the gas absorption coefficient which depends on the wavelength of the incident light. C is the gas concentration and L is the path length of the gas cell.

In order to describe the transmission of a monochromatic source, equation (2.40) can be modified as follows [33]:

$$\left({}^{I_1}/_{I_0}\right)_{\tilde{\nu}} = e^{-\alpha_{\tilde{\nu}}} \tag{2.41}$$

where the spectral absorbance in terms of wavenumber is defined by the variable $\alpha_{\tilde{\nu}}$ which has a linear relationship with couple of physical parameters as given by:

$$\alpha_{\tilde{\nu}} = p\chi_{abs}S(T)\varphi_{\tilde{\nu}}L \tag{2.42}$$

In equation 2.42, p and T are the pressure (atm) and temperature (K) of the molecule. χ_{abs} is the gas volume mixture ratio of the absorbing species, S is the spectral line strength ($cm^{-2}atm^{-1}$). $\varphi_{\tilde{\nu}}$ is the line shape function. Different line- shape functions generally used in spectroscopy will be discussed in details in the following section.

2.9. Line-shape functions

2.9.1. Overview

In spectroscopy, "line-shape function" refers to theoretical models used to describe the shapes of spectral lines. Different line-shape functions have been used in the past few decades. The choice of the function depends on the temperature, pressure and all other physical conditions of the gas molecule. Depending on the quality of the spectra, several physical effects including natural line broadening, Doppler broadening, collisional broadening and shift, line-mixing, Dicke narrowing, speed dependence, temperature dependence etc. need to be considered while fitting them to a line shape profile.

2.9.2. Natural line broadening

Let us consider a two-level atomic system for spontaneous emission (Figure 2.9), where E_1 is the excited energy state of an atom having intrinsic lifetime of τ_{sp}. According to Heisenberg's uncertainty principle, it can be written as follows:

$$\Delta E\, \Delta t \geq \frac{h}{2\pi} \tag{2.43}$$

But since $\Delta t = \tau_{sp}$ and $\Delta E = h\Delta \upsilon$, equation (2.43) can be expressed in the following way:

$$\Delta\upsilon \sim \frac{1}{2\pi\tau_{sp}} \tag{2.44}$$

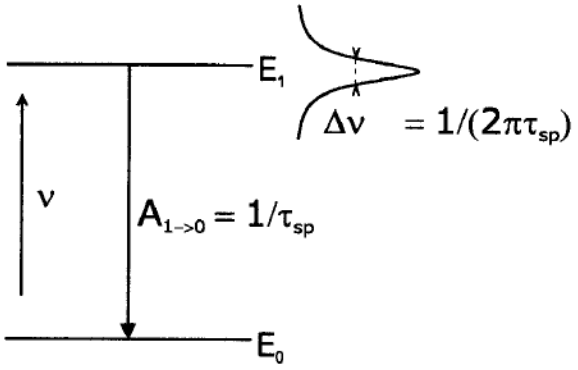

Figure 2.9: Spontaneous emission for $E_1 \rightarrow E_o$ transition, which arises a finite linewidth (adopted from source, p: 27) [36].

The uncertainty principle defines the spontaneous lifetime of the atom in the excited level, and predicts that the atom would not be able to stay in the excited state (E_1) more than τ_{sp} seconds on average. Due to the transition between these two energy levels, a spread of frequencies (line width) will appear, and is known as the "natural linewidth".

2.9.3. Doppler profile

At very low pressure, molecules in a gas can move randomly by the influence of their thermal motion. Let us consider a gas molecule is undergoing no collisional effect and moving with uniform velocity ($\vec{v}$) due to its thermal motion, then the position of that molecule at time t will be:

$$r = \vec{v}t \tag{2.45}$$

The change in position of the molecule with time will give rise to a Doppler shift and it can be expressed as:

$$Doppler\ shift = \frac{w_\nu v_z}{c} \tag{2.46}$$

In the above expression, w_v is the transition frequency. v_z is the velocity component of the free streaming molecule and it is always directed parallel to the incident wave vector (k). Therefore, a Doppler shift associated with v_z can be shown in terms of Maxwell-Boltzmann thermal velocities distribution:

$$F_M(v_z) = (\frac{M}{2\pi k_B T})^{3/2}\, e^{-(\frac{v_z}{v_p})^2} \tag{2.47}$$

$$v_p = (\frac{2k_B T}{M})^{1/2} \tag{2.48}$$

where M and v_p are the mass and the most probable speed of the molecule. An inhomogeneous broadening is introduced by this velocity distribution and it is symmetric about the transitions frequency. The dipole auto-correlation function needs to be discussed in order to consider this inhomogeneous broadening. For free streaming molecule the dipole autocorrelation function can be written as [33]:

$$C_{ext}(t) = < e^{-i(\vec{k}\,\vec{v})t} > \tag{2.49}$$

By using equation 2.45, the thermal equilibrium of equation 2.47 can be resolved in the following way:

$$C_{ext}(t) = \; e^{-(\frac{\Delta\omega_D t}{2})^2} \tag{2.50}$$

Here $\Delta\omega_D$ is the Doppler width. The relationship between Doppler width and the Doppler line profile can be achieved by doing the Laplace transform of equation 2.48, as follows:

$$I_D(\tilde{\omega}) = \frac{1}{\sqrt{\pi}\Delta\omega_D}\, e^{-(\frac{\Delta\omega_D t}{2})^2} \tag{2.51}$$

with the detuning angular frequency,$\widetilde{\omega} = \omega - \omega_v$. The line shape function of this profile is a Gaussian function whose half width half maximum (HWHM) $\gamma_D$would be:

$$\gamma_D = \sqrt{\ln(2)}\frac{\Delta\omega_D}{2\pi c} \tag{2.52}$$

This line shape model is only applicable when molecules are moving due to their thermal motion and the collisional effects (pressure less than 10^{-3} atm) among the molecules are almost negligible. But, higher pressure and at lower temperature, the Doppler line profile would not be able to analyse the line shape of the molecules.

2.9.4. Lorentz profile

With the increase of pressure, molecules in a gas sample will exhibit collisional broadening. When two molecules collide with each other a phase shift $\varphi(t)$ in the rotational and vibrational energy states will be observed for both of them. Taking the average of the phase shift, the correlation function related with ro-vibrational degrees of freedom can be presented as:

$$C_{int}(t) = e^{i<\varphi(t)>} \tag{2.53}$$

where $\varphi(t)$ is the average of the phase shift which has both real and imaginary parts. Putting both the components in equation 2.51, the correlation function becomes:

$$C_{int}(t) = e^{-<(\Gamma+i\Delta)>} \tag{2.54}$$

In the above expression, Γ is the real part of the phase shift which describes the frequency shift and the imaginary part Δ defines the decay rate.

These collisional effects of the molecules lead to introduce a line shape model known as the Lorentz profile. By performing a simple Laplace transform of equation (2.52) the Lorentz profile can be obtained as follows:

$$I_L(\tilde{\omega}) = \frac{1}{\pi} \frac{\gamma_p}{(\tilde{\omega}-\delta p)^2+(\gamma_p)^2} \tag{2.55}$$

with γ_p as the HWHM and δp as the collisional shift at pressure.

2.10.5. Voigt profile

At intermediate pressures, both the thermal and collisional effects can be handled by considering a Voigt profile which is a convolution of Doppler and Lorentzian profiles. Depending on the pressure limits the Voigt profile will act either as a Doppler or as a Lorentz profile. The general expression of a Voigt profile can be expressed as [33]:

$$I_v(x,y) = \int_{-\infty}^{\infty} I_D(\tilde{x}') I_L(x-\tilde{x},y)d\tilde{x}' \tag{2.56}$$

$$\tilde{x}' = \frac{\tilde{\omega}}{\Delta\omega_D}, x = \frac{\tilde{\omega}-\Delta}{\Delta\omega_D} \; and \; y = \frac{\Gamma}{\Delta\omega_D}$$

where $\tilde{x}', x \; and \; y$ are dimensionless parameters. In terms of a complex probability function equation 2.54 can be written as:

$$I_v(x,y) = \frac{1}{\sqrt{\pi}} \int_{-\infty}^{\infty} Re[w(x,y)] \tag{2.57}$$

where the complex probability function, $w(x,y)$ can be written as:

$$w(x,y) = \frac{i}{\pi} \int_{-\infty}^{\infty} \frac{e^{-t^2}}{x-t+iy} \, dt \tag{2.58}$$

2.9.6. Speed-Dependent Voigt (SDV) profile

The Voigt profile assumes that the thermal motion of the gas molecules travels at the most probable speed following the Maxwell-Boltzmann velocity distribution. But, in reality, gas molecules do not move with the same most probable speed. Hence, it is important to introduce a new line profile to see how the broadening and line shifts are affected by the velocity of the gas molecules. Thus, the velocity-dependent broadening and shifting terms introduce an asymmetry in the line shapes which is understood by the Speed-Dependent Voigt (SDV) profile. The SDV model is usually introduced when the regular Voigt profile is not sufficient to minimize the weighted residuals of the spectra.

Berman [37] was the first person who analytically incorporated the speed-dependent effects of the molecules in Voigt line shape functions and expressed the speed-dependent Voigt function in the following way:

$$I_{sdv} = \frac{1}{\pi}\, Re\{\int \frac{F_M(\vec{v})}{[\Gamma(v) - i(\tilde{\omega} - \Delta(v)) - \vec{k}\,\vec{v}]}\, d^3\vec{v}\} \tag{2.59}$$

$\Gamma(v)$ and $\Delta(v)$ are the speed-dependent broadening and shift, respectively. $F_M(\vec{v})$ is the Maxwell-velocity distribution function which has already defined in equation 2.47.

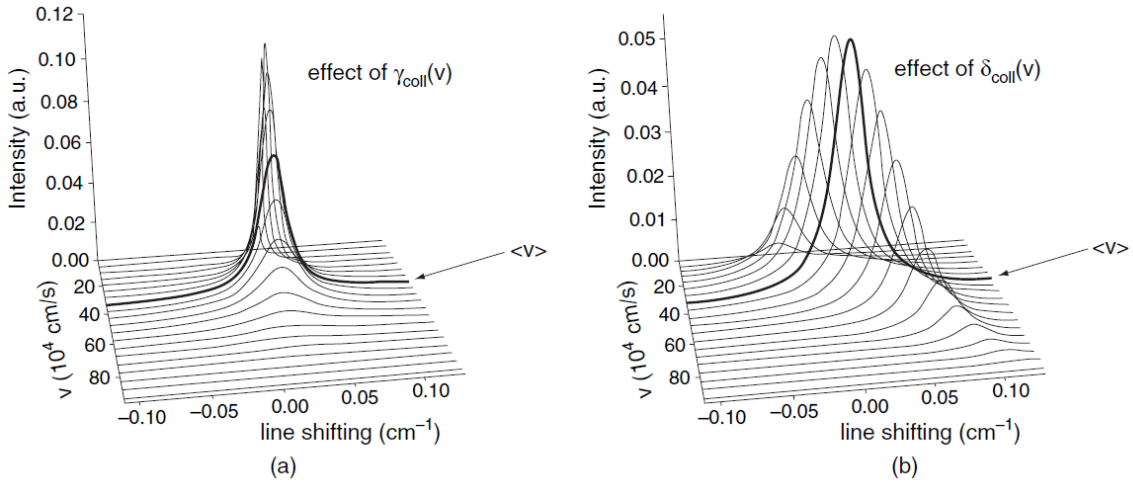

Figure 2.10: Effects of speed dependence on a spectral line. *(a)* collisional line broadeing $\Gamma(v)$ affected by the speed dependence broadening *(b)* impact of the speed dependence of the line shift $\Delta(v)$ (adopted from source, p: 92) [38, 39].

2.9.7. Rautian-Sobelman profile

The Voigt profile has been used in laboratory spectra analysis from the early age of spectroscopic remote sensing. For many applications, it has the ability to follow the physical conditions of the spectra when they are fitted. Moreover, this profile is comparatively faster and more reliable for the analysis of spectra. However, one of the subtle effects in the spectra known as “Dicke narrowing” can not be accounted for with this profile.

At intermediate gas pressures, the Dicke narrowing effect, which is also known as collisional narrowing, occurs when the wavelength of the incident light becomes exactly the same or less than the mean free path (MFP) of the gas molecules. MFP is the average distance travelled by any gas molecule before colliding with other molecule. Due to this effect, in the Voigt profile, the value of broadening coefficients would become smaller than

the expected value. In order to consider, the narrowing effect, the Rautian-Sobelman [40] model for hard collisions has been implemented.

Depending on the mass of the absorber molecule (M_1) and the perturber (M_2) two types of collisions have already been identified. If the mass of the radiator is almost equal or lighter than the perturber ($M_1 \leq M_2$), then the molecules experienced hard collisions, resulting a hard collision profile commonly known as Rautian-Sobelman profile. In this present study, we used the Rautian-Sobelman profile because the mass of the radiator molecule, CO (27.99 g/mol) and the perturber, an average air molecule (28.96 g/mol) are very close to each other. The general mathematical formula for Rautian-Sobelman profile can be expressed as [40]:

$$I(R) = \frac{1}{\sqrt{\pi}} Re\ [\frac{w(x,y+z)}{1+\sqrt{\pi}w(x,y+z)}] \tag{2.60}$$

In the above expression, $z = \frac{V_{VC}^{H}}{\Delta\omega_D}$; where V_{VC}^{H} is the hard velocity changing collision rate.

2.9.8. Narrowing Parameter

A single united atom force field model was used by theoreticians Dr. Aziz Ghoufi and his research group members at Universite de Rennes, France to calculate the diffusion constant of CO [41]. For that, van der Waals interactions were considered to describe the intermolecular interaction of a CO gas sample and these interactions were modeled by a Lennard-Jones potential. Molecular dynamics (MD) simulations were run by using a software package known as DLPOLY [42]. In the simulation, a 10 ns time period is considered as acquisition phase after an equilibrium period of 5 ns whereas 1 fs was used as time-step. While running the MD simulation, a statistical ensemble like NVT was taken

into account where N corresponds to the number of particles, V is the volume of the box and T = 300 K. The Nose-Hoover algorithm [43] was used in order to keep constant canonical ensemble temperature where the thermostat relaxation time was 0.5 fs. The Verlet algorithm to calculate velocities was used by theoreticians for the integration of the motion equation [44]. The self-diffusion coefficient (D_s) of any gas sample can be computed from the Mean Square Displacement (MSD) method:

$$D_S = \frac{1}{6}\lim_{t\to\infty}\frac{MSD}{t}$$

$$MSD\ (t) = \langle\sum_{i=1}^{N}(r_i\ (t) - \ \ r_t(0)^2\rangle \tag{2.61}$$

where the position of a particle (i) at time t is denoted by r_i (t). From the above expression, the calculated diffusion constant of pure CO is 1.938137x10^5 cm^2 s^{-1}. The narrowing parameter (β_c) is related to the diffusion constant through the following equation [45]:

$$\beta_c = \frac{K_B T}{2\pi c M D} \tag{2.62}$$

where $K_B T$ is the thermal energy of the molecules, *c* is the speed of light, M is the molar mass and D denotes the diffusion constant. The narrowing parameter for pure gas calculated from equation 2.60 is 0.024076 cm^{-1}. Consistently, narrowing parameters for the spectral lines were fixed throughout the entire spectra analysis process.

2.9.9. Temperature dependence of line parameters

The interpretation of line-shape parameters of atmospheric trace gases is always complicated because of their randomly changing physical conditions. Temperature is one of the vital conditions in the atmosphere which has significant impacts on molecular line

shape. Temperature-dependence phenomena of the line-shape parameters were first observed by Birnbaum [46] and later were developed by Bonamy *et al*. [47]. According to their approximation, the line-shape parameters as a function of temperature can be shown as:

$$\frac{\sigma_1}{\sigma_2} = \frac{\gamma(T_1)}{\gamma(T_2)} = \left(\frac{T_1}{T_2}\right)^{-n} \tag{2.63}$$

The left side (σ) of the above equation defines the line-shape parameter of interest and the pressure-broadening coefficient $\gamma(T)$ is considered here as an example for that. T is the temperature and n is the temperature-dependence coefficient.

Variations of this law can be discussed from two different theoretical perspectives. The first theoretical concept assumes a simple kinematic case where mean molecular velocity and molecular density are examined in terms of collisional frequency. This assumption shows a linear relationship between the collisional frequency and molecular density as well as with the mean molecular velocity. Hence, density will vary inversely with temperature (T^{-1}) and molecular mean velocity follows a square root relationship with temperature($\sqrt{T}$). This is the example of a simple case for that n = 0.5. But, in reality, $n = 0.5$ is rarely measured and therefore a more reliable approach known as Anderson-Tsao-Cunette Theory [48, 49] needs to be considered, for getting a complete understanding on the molecular dynamics. Later it was Birnbaum [46] who considered partial collisional cross sections and the form of collisional efficiency in the Anderson-Tsao-Cunette theory in order to express it in a simplified way. When the quadrupole-quadrupole forces are considered as the dominant factors, then the inclusion of these two modified terms change the value of n from 0.50 to 0.75 [50]. Equation 2.61 has been used as a determinant of n

which has rotational quantum number dependency and can also vary with the temperature range of interest [51]. The output of Bonamy *et al.* [47] study came to a point that Birnbaum [46] assumptions will not be valid at a higher temperature range when molecular collisions begin to decrease from their usual rate. However, this scaling law has performed quite nicely for a specific temperature range especially for the temperate in the earth's lower atmosphere [50, 52].

2.9.10. Line Mixing

2.9.10.1. Overview

If two adjacent spectral lines represent the same initial and final vibrational states, it is possible that the angular momentum between molecules present in the gas is perturbed due to inelastic collisions, which will result in mixing of the two lines. Basically, line mixing or line coupling is responsible for some of the observed line asymmetries in molecular spectra. At the beginning, the computed spectrum in the least square solution considered as a Voigt profile inclusion of line mixing which allows to fit or fix line mixing in the solution.

2.9.10.2 The Relaxation Matrix

The Lorentzian profile is the dominating portion in the Voigt shape model. If, $I(\omega)$ denotes the Lorentzian part of the line-shape factor as a function of different variables then the overall equation can be written as [27].

$$I(\omega) = X^T\ (\omega - \omega_0\ - iW)^{-1}\rho X \tag{2.64}$$

ω and ω_0 both are N x N diagonal matrix in which the wavenumbers of the spectral line positions are considered as diagonal elements for the first matrix (ω) whereas line positions having zero pressures are supposed to be the diagonal elements for ω_0 matrix. For both of the cases, the off-diagonal elements are supposed to be zero. For each spectral line, ρ is the population number of the lower energy state. X is a 1xN matrix that represents a ratio between the square root of the intensity (S) and the number of density (ρ) of each spectral line. T represents the transpose of the matrix and i is an imaginary number. W is the relaxation matrix which describes the nature of the physical conditions like line mixing within the spectral line profiles at any time. The diagonal elements of W give both the Lorentz widths (α_{Lj}) and pressure-induced shifts (δ_j). The real part of the matrix presents broadening and the imaginary part corresponds the pressure shift.

$$W_{jj} = \alpha_{Lj} + i\delta_j \tag{2.65}$$

The details calculations of relaxation matrix is reported in reference [53]. In order to calculate the broadening and line mixing coefficients, it is important to solve the relaxation matrix. There are two (EPG law and ECS approximation) models that have been implemented for the calculation of the relaxation matrix, W.

CHAPTER 3: EXPERIMENTAL DETAILS

3.1. Overview

The Michelson interferometer is the main component of most FTIR spectrometers and is considered as the first design of interferometer used in Fourier Transform spectrometers. How a Michelson interferometer works and how the interferogram becomes a spectrum will be discussed in detail in this chapter. In addition, the Cat's Eye design interferometer and its advantages will be presented. This chapter will describe the general structure of 1-m McMath-Pierce Fourier transform spectrometer (FTS) situated at Kitt Peak, National Solar Observatory (NSO), Arizona. Finally, the spectra analysis software "Labfit" will be discussed at the last part of this chapter.

3.2. Introduction to Fourier Transform Spectrometer (FTS)

3.2.1. Principle of a Michelson Interferometer

The Michelson interferometer comprises an infrared light source, two plane mirrors and a beamsplitter connected to a detector system. One of the mirrors is fixed and the other one can move perpendicularly along the direction of the incident light. The beamsplitter can split a light beam into two beams of light, where the difference in distances traveled by these light beams is used to create an interferogram, which is a pattern of light intensities. This variation in distance is called the optical path difference (OPD). The combined light beam which leaves the interferometer is resolved as a function of OPD by a detector and is basically gives the spectral information to the spectrometer [4]. The simplest optical arrangement of a Michelson interferometer is illustrated in Figure 3.1.

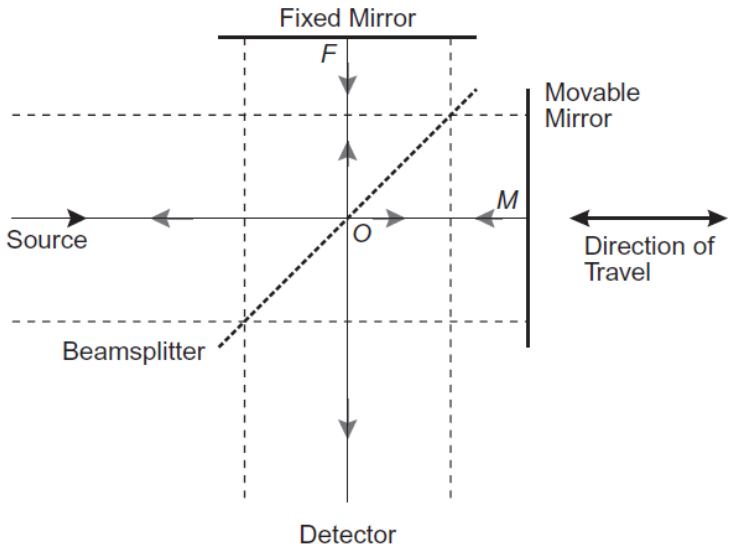

Figure 3.1: Optical arrangement of Michelson Interferometer (adopted from source, p: 20) [65].

In Figure 3.1 the fixed mirror and the movable mirror are perpendicular to each other. At point O, the beamsplitter ensures that half of the incident infrared light is transmitted along OM direction and the rest of the light is reflected in the OF direction. The reflected light goes to the fixed mirror, whereas the transmitted light strikes the movable mirror. After coming back from their respective mirrors, they interfere at the beamsplitter and are again transmitted and reflected equally. After interacting with the sample, the transmitted recombined beam strikes the detector.

When the movable mirror and the fixed mirror are equidistant from the beam splitter and the light beams travel the same distance and bounce back to the beam splitter at the same time. In that case, OPD of the light beams will be zero, which is commonly known as zero path difference (ZPD) [4]. If there is no path difference, the two beams are assumed to be in phase and create a constructive interference at the beam splitter. However, an optical path difference usually occurs due to the movement of the movable mirror. The deviation of the moving mirror from the ZPD is known as mirror displacement (Δ). The

optical path difference (OPD) is usually referred to as optical retardation and is denoted by the symbol δ. The relationship between the path difference (δ) and the mirror displacement can be expressed as:

$$\delta = 2\Delta \tag{3.1}$$

The above equation implies that the additional distance travels by the infrared ray reflected from the moving mirror compare to fixed mirror is equal to 2Δ. Constructive interference occurs when the path difference of the light beam is equivalent to multiples of its wavelength (λ). Mathematically it can be written as:

$$\delta = n\lambda \tag{3.2}$$

where $n = 0,1,2,3,..$ In contrast, when the extra distance of the moving mirror is $1/4\,\lambda$ compare to the fixed one, then according to equation 3.1 the path difference would be $1/2\,\lambda$. The interference of the light beams under this condition is called destructive interference and is given by:

$$\delta = (n + 1/2)\,\lambda \tag{3.3}$$

In that case, light beams are completely out of phase while overlapped with each other and result in a very low intensity recombined beam. A graphical representation of light intensity and OPD is known as an interferogram, which is the basic measurement retrieved by an FTIR. After being Fourier transformed, this interferogram is converted into a spectrum. A complete interferogram is obtained when the moving mirror accomplished a complete backward and forward motion. Such a complete back and forth motion referred to as a full scan. The frequency of the interferogram and the velocity of the movable mirror are related by the following equation:

$$F_v = 2VW \tag{3.4}$$

where F_v is the frequency of the interferogram which is also known as the Fourier frequency, V velocity of the moving mirror in cm/s, and W presents the wavenumber of the light in cm^{-1}.

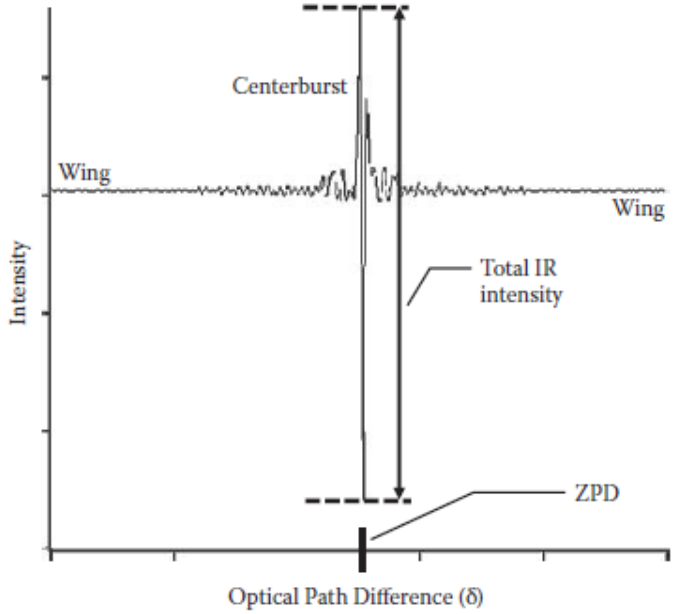

Figure 3.2: Layout of an interferogram (adopted from source, p: 27) [4].

Infrared light having many wavenumbers constructively interferes at ZPD, and a large burst of intense peak arises in the interferogram. This intense peak is known as centerburst, which is only possible when all the wavelengths of the infrared light are in-phase. With the change of the optical path difference, the intensity of the light drops rapidly on both parts of the interferogram. Either side from the centerburst are known as the wings of the interferogram. The intensities of the wings are always very low, due to the overlapping of various frequencies which are out of phase and interfered destructively.

3.2.2. The Cat's Eye Design for Fourier Transform Interferometers

In this experimental work, instead of a Michelson interferometer, a "Cat's Eye" design interferometer was used. It has a movable beam splitter with a combination of two identical "Cat's Eye" shape concave mirrors M_1 and M_2 having a radius R [54]. Such type of interferometer is also known as Double Cat's Eye (DCE) interferometer. The optical alignment of this interferometer is shown in Figure 3.3.

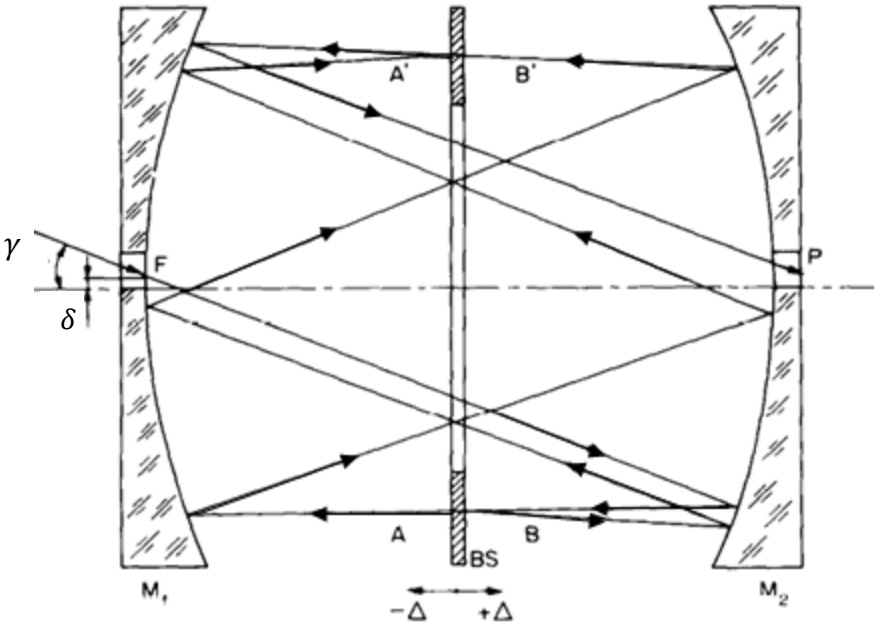

Figure 3.3: Light passing through the optical arrangement of a Cat's Eye interferometer [54].

At the beginning, the beam splitter is placed at the center of the two mirrors. As it is a moving splitter, it can move either side of the mirrors having a value of $\pm\Delta$. The movement of beam splitter yields the optical path difference by an amount of $\pm\ 4\Delta$. In Figure 3.3, the direction of the entrance light and the mirrors axis is denoted by the angle γ, and δ ($\delta \ll$ R) is the deviation of the focal point of the entrance light in mirror M_1 from the mirrors axis. The beam splitter splits the entrance beam, and the beam will leave the interferometer after interference. The entrance light passes through the beam splitter and

strike the mirror M_2, and after reflection, the beam hits the splitter again and splits it into two coherent beams A and B. Beam A passes through the beam splitter, whereas beam B bounces back to mirror M_2. At the mirrors, both beams have reflected three times and interfered at the top of the beam splitter. The beams at the top of the beam splitter are named as A' and B', which are exactly parallel to A and B, correspondingly. Finally, the interfered beam reflected from the mirror M_1 and focused onto the detector P.

3.2.3. Advantages of Double Cat's Eye (DCE) Interferometer

Optical elements having high linear and angular misalignments both are allowed in the Double Cat's Eye (DEC) interferometer. Hence, optical alignment in DEC is not necessarily important during the process of the interferometer. At the beam splitter, the interferometer has both non-coincidental and interfering beams, and it can also produce extra light channels without creating any complexity in its structure. Movement of the beam splitter has a significant impact on the resolution of the interferometer, and it can be twice for per unit motion of it. A DCE interferometer has a small angle of view. In the laboratory, Fourier spectrometers sometimes require to measure a small angle of view, and it can easily be measured with this special interferometer.

3.2.4. Signal-to-Noise Ratio (SNR)

The measurement of the signal-to-noise ratio (SNR) determines the performance of any Fourier transform infrared spectrometer. SNR is obtained by taking a ratio of the peak height of a spectrum and the level of noise close to the spectrum at some baseline point. Usually, random fluctuation of the spectrum leads to the introduction of noise at

above or below the baseline. Furthermore, SNR has a relationship with the number of scans (N), and is given by:

$$SNR \propto (N)^{1/2} \tag{3.5}$$

Table 3.1. Relationship between SNR and number of scans [4].

No: of Scans	SNR changes over 1 scan
1	1
4	2
16	4
25	5
64	8
100	10
1024	32

FTIR having high SNR is a sensitive technique and has the ability to measure the absorbances more accurately.

3.2.5. Interferogram to spectra

As it was mentioned earlier in section 3.2.1, the Fourier transform of an interferogram leads to a spectrum. According to Joseph Fourier, a sum of sine and cosine waves can be expressed as a series with a single mathematical function having a simple x and y plot.

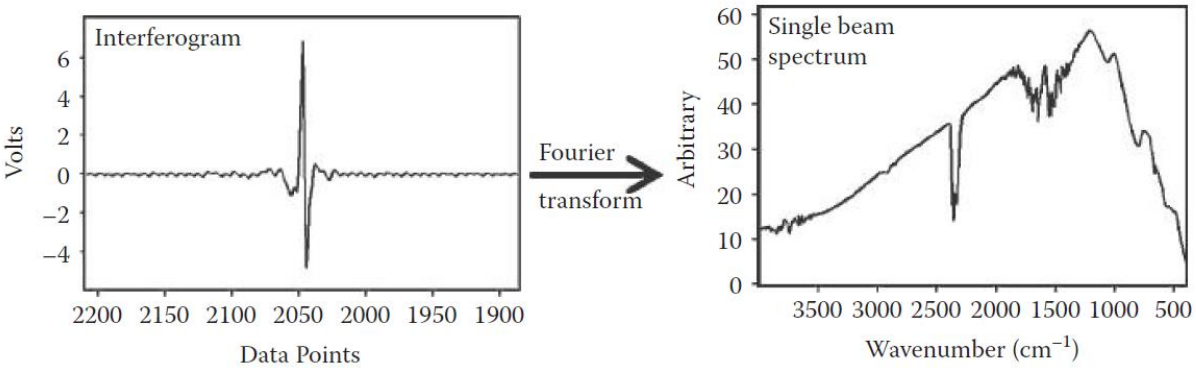

Figure 3.4: Fourier transformation of an interferogram which yields a single beam spectrum (adopted from source, p: 32)[4].

In this context, the interferogram of directed light to the detector is considered as a superposition of cosine waves. The interferogram or interference pattern of cosine waves are measured with the detector. Therefore, the interferogram can be written as follows:

$$S(\delta) = B(\tilde{v}_o) cos\ 2\pi\tilde{v}_o\delta \tag{3.6}$$

Where $B(\tilde{v}_o)$ is the intensity of light at a wavenumber $\tilde{v}_o$ and $S(\delta)$ is the cosine Fourier transform of $B(\tilde{v}_o)$. The computation of this cosine Fourier transform, yields the infrared spectra. For a continuous light source, the interferogram can be expressed by the integral as follows:

$$S(\delta) = \int_{-\infty}^{+\infty} B(\tilde{v}) cos\ 2\pi\tilde{v}\delta\ \ d\tilde{v} \tag{3.7}$$

In this experimental work, I considered wavenumber (frequency) domain as the Fourier space. The relationship between the transformed spectra and the interferograms can also be explained in terms of their units. Units of the x-axis of any function will be inverted when it undergoes through the Fourier transformation process. Graphically, the optical path difference (cm) and infrared intensity are plotted in the x and y-axis of an interferogram, and when the interferogram is Fourier transformed an inverted x-axis units will appear.

This new intensity vs. wavenumber (cm^{-1}) function is known as the infrared spectrum as shown in Figure 3.4. The term “single beam” written at the upper left side in Figure 3.4 illustrates that the FTIR spectrometer used only one infrared beam in order to obtain this spectrum. When the interferograms are measured with a single beam without any sample present in the spectrometer, then the obtained single beam spectrum is known as a background spectrum. The background spectrum contains the spectral information

from the instrument and the environment. However, the interferogram obtained in the presence of a sample and the Fourier transformation of that interferogram yield a sample beam spectrum, which additionally includes the contribution of the sample along with the environmental and the instrumental influences. In order to get only the sample spectral information, it is important to cancel the environmental and the instrumental contributions from the sample beam spectrum. To do this, the sample spectrum must be divided with the background spectrum, and this ratio will give a transmitted spectrum as follows:

$$\%T = I/I_o \tag{3.8}$$

where I and I_o are the intensities of the sample and the background spectrum.

3.3. Experimental Setup

3.3.1. FT spectrometer at the National Solar Observatory, Kitt Peak, AZ

The spectra of CO were recorded with a 1-m McMath-Pierce Fourier transform spectrometer (FTS) at Kitt Peak, National Solar Observatory (NSO), Arizona, USA. The details of this experimental setup is given by A.W. Mantz *et al*. [28]. In their study, they used Helium (He) as a perturber whereas in my study I used air. Both of the cases, the experimental setup was same. The summary of the experimental setup is listed in Table-3.2. The simple experimental setup for the measurements of IR spectra of CO (0→1) band comprised of an Oriel glowbar source having voltage powers of 10-12 V, a potassium chloride (KCl) beamsplitter, two InSb detectors which are at liquid-nitrogen temperature, gas controlling system and an electronic device to store the data. Two coolable absorption sample cells having path length 1.1313 and 4.3050 cm, were placed between the IR source and the slit of the spectrometer. Both gas cells were made of oxygen-free high-conductivity

copper (OFHC). Each of the sample cell was placed on an OFHC mounting platform and the OFHC copper station itself was attached to a CTI-Cryogenics pump. The sample temperatures were controlled with two sensors, which were basically 50 W heaters and are connected to the OFHC copper mounting platform. Each cell is provided with its own temperature sensor. The Lakeshore Model 331 and Model 630 are the sensors to readout, control and calibrate the temperature of the cells. These sensors are very effective in maintaining the temperature with $\pm$0.01 K over the temperature range of 12-250 K [55].

Table 3.2**:** Experimental setup of 1-m McMath-Pierce FTS [28].

Spectral coverage range	0-2980 cm^{-1}
Maximum optical path difference	96.12 cm
Path length of the cells	1.131 and 4.305 cm
Spectral resolution	0.0052 cm^{-1}
Co-added scans	10-12
Time for spectra recording	1h (approximately)
Signal-to-noise ratio	850 (approximately)
Size of the FTS aperture	8 mm
IR Source	Oriel Glowbar at 12 V
Detectors (2)	InSb
Beam splitter	KCl
Filters	InAs+ Si Nose

The sample cells are placed inside a vacuum chamber. The chamber is generally kept at pressure less than 10^{-6} Torr by cryopumping it with a cryocooler. Throughout the experiment, a large mechanical pump continuously pumped the vacuum chamber and maintained the chamber vacuum. There were two CaF_2 windows inside the chamber, and each cell is provided with windows having a diameter of 50 mm, which allows a beam of

45 mm to pass through the gas cells. Both cells do not have any temperature gradients throughout their entire length.

3.3.2. Spectra Recording and Calibration

At the beginning, few spectra of pure CO were recorded with the shorter cell and due to some temperature sensing problems related to this cell, the rest of the spectra of pure and air-mixed CO were recorded with the longer cell. At room temperature, the small cell was filled with 99.998 % (research grade) pure CO. In order to avoid molecular collisions, initially, low CO pressures (≈1 Torr) were chosen so that only the thermal motion of the molecules contributes accurate line center positions, which allow the consideration of precise pressure-induced shift measurements. The pressures inside the gas cells were consistently monitored during the entire data retrieval periods. 12 scans were averaged for each spectrum. After recording few spectra of pure CO at room temperature, air molecules having a pressure range between 35 and 620 Torr were added to the CO to the longer gas cell. Details of the physical conditions of all spectra are reported in chapter four.

To measure the line shifts of the spectra, calibration of the wavelength scales with respect to CO line positions of the fundamental band (0→1) is very important and this process was done by our collaborators with accuracy ~0.00018 cm^{-1} [28]. Usually, spectra are calibrated by taking the ratio of the observed and calculated line positions of different molecules present in the spectral range. In this study, a couple of strong and weak water lines were taken into account to calculate the calibration factor. Mathematically, it can be written as:

$$\text{Calibration factor} = \left(\frac{\text{Experimental line position}}{\text{Line position from Hitran}} \right) \tag{3.9}$$

This calibration factor is then multiplied with the wavenumber scale, and used by the software. We used the multispectrum analysis software "Labfit" developed by Dr. Chris Benner of College of William and Mary, Williamsburg, VA, USA to analyze the spectra recorded at various pressures and temperatures in the 2000 to 2280 cm^{-1} spectral range.

3.4. "Labfit" software

3.4.1. Description of "Labfit" software

Labfit is a multispectral fitting program that can be employed to analyze spectra recorded by FT or laser spectrometers. The original version of this code was developed by Dr. Chris Benner in the early 1990's. Since then after a couple of generations, this program has become a very efficient tool in the spectroscopic research community for its simultaneous fitting of numerous spectra. The program uses the Levenberg-Marquardt algorithm which has the ability to reduce the summation of the squares of differences (weighted residuals) between calculated and experimental spectra [56].

This fitting technique has some unique advantages. For example, spectra obtained with a tunable diode laser spectrometer and a Fourier-transform spectrometer can be fitted simultaneously. Furthermore, spectra retrieved at various spectral resolutions can also be fitted simultaneously. This program can run iteratively, after each iteration, the fitted parameters are updated automatically. This program allows users to modify or change parameters from the solution. New spectra can also be added to the solution at any time.

Based on known experimental conditions like temperature, pressure, mixing ratio etc. Labfit can fit the spectra using different spectral line-shape parameters such as line positions, intensities, line widths, pressure shifts, line mixing, narrowing and so on, for

each spectral line. At the beginning, each of the spectra is fitted individually, and then these values are averaged or combined to get the final results.

3.4.2. Speed-dependent Voigt (SDV) and its implementation in Labfit

The Speed-dependent Voigt (SDV) model is employed when the regular Voigt profile is not enough to minimize the weighted residuals of the spectra. In this study, Labfit was employed to determine the speed-dependent line-shape parameters. To do this, several spectra were simultaneously fitted in the program, accounting for speed-dependence in the Voigt line-shape model or in the Rautian line-shape profile. The mathematical formulation of speed-dependent broadening coefficients of molecules having velocity *v* can be expressed in the following way [18, 57-60].

$$\gamma^0(v) = \gamma^0\left\{1 + \Gamma_2\left[\left(\frac{v}{v_p}\right)^2 - 1.5\right]\right\} \tag{3.10}$$

where γ^0 represents the thermally average pressure broadening coefficients. Γ_2 is the speed dependence parameter [57, 58]. v_p is the most probable speed, described earlier in equation 2.48.

The speed-dependent broadening coefficients in equation (3.10) and the Voigt line-shape model in equation (2.65) both are considered for calculating the speed-dependent Voigt line-shape function. After integrating that function, the real (K_s) and imaginary (L_s) parts become:

$$K_s(x, y, S) = \frac{2}{\pi}\int_{-\infty}^{\infty} e^{-v^2} v \tan^{-1}\left\{\left[\frac{v+x}{y(s\{v^2-c\}+1)}\right]^2\right\} dv \tag{3.11}$$

$$L_s(x, y, S) = \frac{1}{\pi} \int_{-\infty}^{\infty} e^{-v^2} v \ln\left\{\left[\frac{v+x}{y(s\{v^2-c\}+1)}\right]^2\right\} dv \quad (3.12)$$

In Labfit, the speed-dependence parameter is fixed to 0 while running it with the Voigt profile. In our study, while considering the speed-dependent Voigt profile, a guess value (0.08000) was taken as a speed-dependent parameter and I fitted this parameter for all 40 studied strong transitions. There are no previous speed-dependent coefficient values published for the 0→1 band of CO. The 0.08 initial value was chosen as a guess value for this study based on a CO study of the 0→2 band [18].

CHAPTER 4: EXPERIMENTAL AND THEORETICAL RESULTS

4.1. Overview

This chapter will cover the line-shape measurements of pure CO, as well as air-broadened CO spectra at room temperature and other temperatures ranging from 79 to 296 K. The Voigt, Speed-Dependent Voigt (SDV), and Rautian profiles will be implemented for these spectroscopic line-shape measurements. By applying the Exponential Power Gap Law (EPG) and Energy Correlated Sudden approximation (ECS), theoretical line-mixing coefficients will be calculated. Finally, this chapter will summarize all the measured results and their comparison with similar published papers.

4.2. Line-shape study of pure and air-mixed CO spectra at room temperature

In order to fit spectral parameters using a multispectrum fitting technique, spectral line parameters like line positions, intensities, self- and air-broadening coefficients were initially taken from the HITRAN database [24]. The following well-known equations were used to determine the pressure-broadening coefficients, pressure-shift coefficients and their temperature dependences [28]:

$$b_L\,(p, T) = p\,[b_L^o\,(air)\,(P_0, T_0)(\,1-\chi)\,[\tfrac{T_o}{T}]^{\,n1} + p\,[b_L^o\,(self)\,(P_0, T_0)\chi[\tfrac{T_o}{T}]^{\,n2} \quad (4.1)$$

$$\upsilon = \upsilon_0 + p[\,\delta^0(air)(1-\chi) + \delta^0(self)\chi] \quad (4.2)$$

$$\delta^0(T) = \delta^0(T_0) + \delta'[T - T_0] \quad (4.3)$$

In equation 4.1 $b_L\,(p, T)$ is the Lorentz halfwidth ($cm^{-1}\,atm^{-1}$) for a single spectral line where p and T are the pressure and temperature. b_L^o and δ^0 denote the pressure broadening and pressure induced line-shift coefficients, respectively, expressed in $cm^{-1}atm^{-1}$ at room

temperature (296 K). b_L^o *(air)* (P_0, T_0) is the Lorentz halfwidth broadened by air at 1 atm and 296 K. χ is the volume mixing ratio ($\frac{P_{CO}}{P_{CO+air}}$). The parameters *n1* and *n2* represent the temperature dependences of air- and self-broadening coefficients, respectively. In equation 4.2, υ_0 (cm^{-1}) and υ (cm^{-1}) are the line positions at zero pressure and at a particular pressure *p*, respectively. In equation 4.3, the temperature dependence of the pressure-induced line-shift coefficient is denoted by δ', whereas $\delta^0(T)$ and $\delta^0(T_0)$ are the temperature dependence of the pressure-induced line-shift coefficients at T and T_0, respectively.

4.2.1. Spectroscopic results and comparisons with other studies

In this study, spectroscopic line-shape parameters for eight spectra of pure and air-mixed CO were analysed at room temperature for the spectral range 2000 to 2280 cm^{-1}. Furthermore, six spectra of pure CO were studied for all the three mentioned profiles. Physical conditions of 10 spectra (6 pure and 4 air-mixed) of CO are listed in table 4.1.

Table 4.1: Physical conditions of the CO spectra.

Temperature (K)	Gas	Path length (cm)	Pressure (Torr)	Volume Mixing Ratio (VMR)
296.96	CO-CO	1.1313	528.74	1
296.56	CO-CO	1.1313	307.99	1
296.41	CO-CO	1.1313	113.81	1
296.36	CO-CO	1.1313	15.63	1
296.36	CO-CO	1.1313	1.02	1
296.42	CO-CO	4.3050	0.94	1
296.92	CO-Air	4.3050	619.61	0.007180
297.02	CO-Air	4.3050	241.41	0.002799
297.13	CO-Air	4.3050	128.90	0.001500
297.19	CO-Air	4.3050	65.28	0.000760

The Voigt profile was implemented for the measurement of line-shape parameters of air- broadened CO spectra. In that case, forty (40) ro-vibrational P- and R-branch

transitions were simultaneously fitted for the spectral range of 2000 to 2280 cm^{-1} (Figure 4.1).

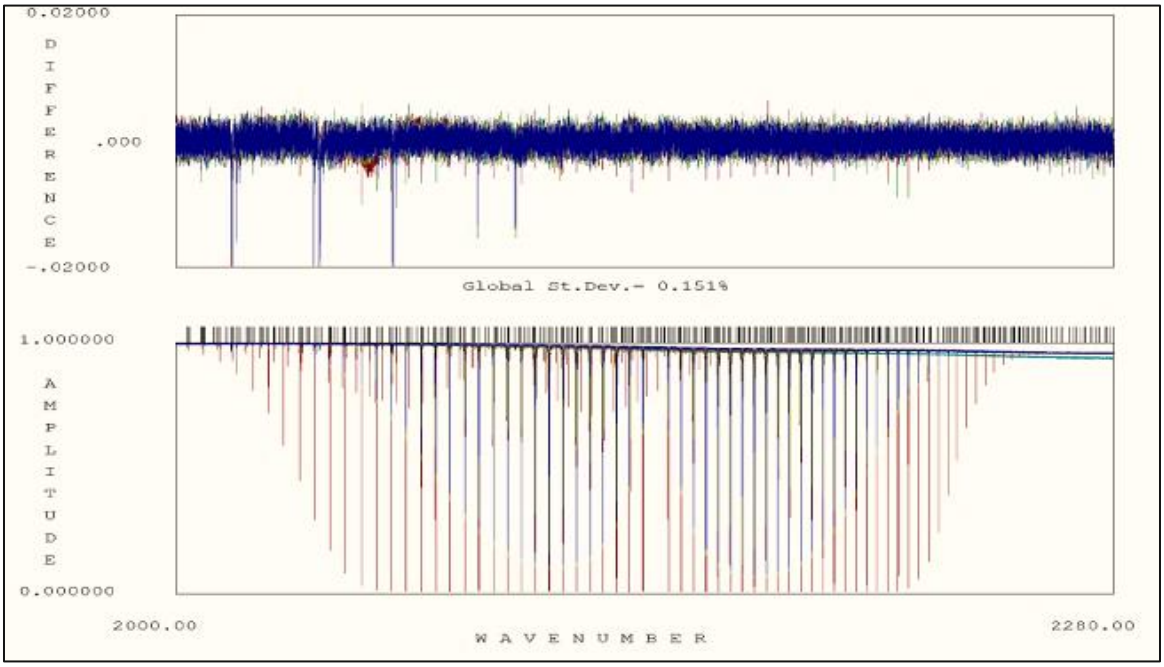

Figure 4.1: In the lower trace, eight CO absorption spectra recorded at 296 K (4 self-broadened and 4 air-broadened) for the spectral range 2000 to 2280 cm^{-1}. The self-broadened spectra were recorded at 528.74, 307.99, 113.81 and 15.63 Torr. The Voigt profile was implemented for their analysis. The upper trace represents the weighted fit residuals. The standard deviation shown here is 0.151%.

The spectral line-shape parameters of air-broadened $^{12}C^{16}O$ measured in the present study are listed in Table 4.2. The rotational quantum index, m (for P branch, m = -J and J+1 for R branch), spectral lines, line position, calculated line intensity, self- and air-broadening coefficients, pressure-induced self- and air-shift coefficients, and the Einstein A-coefficients are listed in the same table. The uncertainties are included in parentheses. Both the pure and air-mixed spectra were fit simultaneously and all the mentioned line parameters were retrieved after one single multispectral fit.

Table 4.2: Line parameters in the P-branch of pure- and air-mixed $^{12}C^{16}O$ (1-0) spectra applying the Voigt profile.

m	Lines	Position[a]	[b]Intensity(self)	b_L^o (air)[c]	b_L^o (self)[d]	δ^o (air)[e]	δ^o (self)[f]	Einstein-A Coefficients[g]
-24	P (24)	2041.666659(2)	$8.22(2)\times10^{-21}$	0.05201(38)	0.0518(1)	-0.00383(36)	-0.00512(1)	14.67 (4)
-23	P (23)	2046.27632(2)	$1.24(2)\times10^{-20}$	0.05351(39)	0.0523(1)	-0.00325(24)	-0.00498(1)	14.75 (4)
-22	P (22)	2050.854316(1)	$1.79(2)\times10^{-20}$	0.05145(19)	0.0541(1)	-0.00283(17)	-0.00478(1)	15.09 (3)
-21	P (21)	2055.400541(1)	$2.52(3)\times10^{-20}$	0.05000(0)	0.0569(1)	-0.00363(10)	-0.00462(1)	15.57(1)
-20	P (20)	2059.914857(1)	$3.53(4)\times10^{-20}$	0.05190(12)	0.0594(1)	-0.00334(9)	-0.00453(1)	15.86(0)
-19	P (19)	2064.397087(1)	$4.81(5)\times10^{-20}$	0.05212(10)	0.0629(1)	-0.00284(7)	-0.00394(1)	16.20(1)
-18	P (18)	2068.847111(1)	$6.44(6)\times10^{-20}$	0.05215(8)	0.059(2)	-0.00276(6)	-0.00546(1)	16.49(2)
-17	P (17)	2073.264776(1)	$8.49(6)\times10^{-20}$	0.05290(7)	0.0584(2)	-0.00288(5)	-0.00431(1)	16.68(3)
-16	P (16)	2077.649941(1)	$1.10(6)\times10^{-19}$	0.05420(6)	0.0631(2)	-0.00329(5)	-0.00408(1)	16.77(3)
-15	P (15)	2082.002414(1)	$1.39(8)\times10^{-19}$	0.05487(5)	0.0655(3)	-0.00272(4)	-0.00503(1)	16.93(3)
-14	P (14)	2086.322108(1)	$1.72(8)\times10^{-19}$	0.05550(5)	0.0675(3)	-0.00277(4)	-0.0059(1)	17.14(3)
-13	P (13)	2090.608842(1)	$2.08(9)\times10^{-19}$	0.05662(5)	0.074(3)	-0.00273(4)	-0.00358(1)	17.30(3)
-12	P (12)	2094.862495(1)	$2.44(11)\times10^{-19}$	0.05741(4)	0.0791(3)	-0.00266(3)	-0.00318(1)	17.53(3)
-11	P (11)	2099.082899(1)	$2.80(12)\times10^{-19}$	0.05803(4)	0.0876(3)	-0.00279(3)	-0.0067(1)	17.76(4)
-10	P (10)	2103.269893(1)	$3.13(14)\times10^{-19}$	0.05898(5)	0.0883(4)	-0.00261(3)	-0.00525(1)	17.95(4)
-9	P (9)	2107.423368(1)	$3.39(15)\times10^{-19}$	0.05952(5)	0.0871(4)	-0.00264(3)	-0.00582(1)	18.21(4)
-8	P (8)	2111.543165(1)	$3.58(16)\times10^{-19}$	0.06050(5)	0.091(4)	-0.00271(3)	-0.00632(1)	18.43(4)
-7	P (7)	2115.629126(1)	$3.64(16)\times10^{-19}$	0.06165(5)	0.0913(4)	-0.00258(3)	-0.00466(1)	18.77(4)
-6	P (6)	2119.681116(1)	$3.56(15)\times10^{-19}$	0.06333(5)	0.096(4)	-0.00250(3)	-0.00642(1)	19.12(4)
-5	P (5)	2123.698989(1)	$3.33(14)\times10^{-19}$	0.06558(5)	0.0934(4)	-0.00242(4)	-0.00462(1)	19.52(4)
-4	P (4)	2127.682582(1)	$2.93(12)\times10^{-19}$	0.06806(5)	0.0925(4)	-0.00222(4)	-0.00481(1)	20.22(4)
-3	P (3)	2131.631739(1)	$2.39(10)\times10^{-19}$	0.07162(5)	0.0924(3)	-0.00201(4)	-0.00488(1)	21.23(3)
-2	P (2)	2135.546349(1)	$1.69(9)\times10^{-19}$	0.07502(6)	0.0907(3)	-0.00174(5)	-0.00578(1)	23.83(4)
-1	P (1)	2139.426248(1)	$8.84(7)\times10^{-19}$	0.08078(11)	0.0915(2)	-0.00157(8)	-0.0034(1)	35.51(3)

[a]line position (cm^{-1}), [b]line intensities (cm^{-1}/molecule. cm^{-2}), [c]air-and [d]self broadening ([cm^{-1}/ (molecule cm^{-2})]), [e]air-and [f]self-shift coefficients (cm^{-1} atm^{-1}), [g]Einstein-A coefficients (s^{-1}).

Table 4.3: Line parameters in the P-branch of pure- and air-mixed $^{12}C^{16}O$ (1-0) spectra applying the Voigt profile.

m	Lines	Position[a]	[b]Intensity(self)	b_L^o (air)[c]	b_L^o (self)[d]	δ^o (air)[e]	δ^o (self)[f]	Einstein-A Coefficients[g]
1	R(0)	2147.081277(1)	$8.98(7)\times10^{-19}$	0.07992(11)	0.0924(2)	-0.00139(8)	-0.00429(1)	12.06 (3)
2	R(1)	2150.856147(1)	$1.77(9)\times10^{-19}$	0.07540(6)	0.0924(3)	-0.00152(5)	-0.0056(1)	14.57(3)
3	R(2)	2154.595729(1)	$2.55(11)\times10^{-19}$	0.07143(5)	0.0865(4)	-0.00159(4)	-0.00279(1)	15.69(3)
4	R(3)	2158.299858(1)	$3.21(13)\times10^{-19}$	0.06820(5)	0.0871(4)	-0.00173(4)	-0.00291(1)	16.47(4)
5	R(4)	2161.968390(1)	$3.73(16)\times10^{-19}$	0.06570(5)	0.0896(4)	-0.00172(4)	-0.00319(1)	16.92(4)
6	R(5)	2165.601187(1)	$4.06(18)\times10^{-19}$	0.06347(5)	0.0913(4)	-0.00167(4)	-0.00212(1)	17.37(5)
7	R(6)	2169.198104(1)	$4.24(20)\times10^{-19}$	0.06180(5)	0.0927(4)	-0.00185(3)	-0.00315(1)	17.65(5)
8	R(7)	2172.758978(1)	$4.26(21)\times10^{-19}$	0.06084(5)	0.0913(4)	-0.00191(3)	-0.00379(1)	17.89(5)
9	R(8)	2176.283676(1)	$4.14(20)\times10^{-19}$	0.05969(5)	0.0841(4)	-0.00186(3)	-0.00467(1)	18.11(5)
10	R(9)	2179.772043(1)	$3.90(19)\times10^{-19}$	0.05886(5)	0.0853(4)	-0.00185(3)	-0.00317(1)	18.28(4)
11	R(10)	2183.223935(1)	$3.58(17)\times10^{-19}$	0.05817(5)	0.0823(4)	-0.00187(3)	-0.00369(1)	18.34(4)
12	R(11)	2186.639215(1)	$3.19(14)\times10^{-19}$	0.05744(5)	0.0805(4)	-0.00186(3)	-0.00317(1)	18.48(4)
13	R(12)	2190.017717(1)	$2.77(12)\times10^{-19}$	0.05664(4)	0.0776(3)	-0.00202(3)	-0.00348(1)	18.63(4)
14	R(13)	2193.359320(1)	$2.35(11)\times10^{-19}$	0.05588(5)	0.0745(3)	-0.00200(4)	-0.0042(1)	18.75(4)
14	R(14)	2196.663859(1)	$1.95(9)\times10^{-19}$	0.05494(5)	0.071(3)	-0.00209(4)	-0.00366(1)	18.75(3)
16	R(15)	2199.931185(1)	$1.58(8)\times10^{-19}$	0.05404(5)	0.0692(3)	-0.00201(4)	-0.00374(1)	18.94(3)
17	R(16)	2203.161164(1)	$1.25(7)\times10^{-19}$	0.05333(5)	0.0654(2)	-0.00219(4)	-0.00431(1)	18.90(2)
18	R(17)	2206.353646(1)	$9.66(7)\times10^{-20}$	0.05253(6)	0.0632(2)	-0.00229(5)	-0.00399(1)	19.08(3)
19	R(18)	2209.508491(1)	$7.32(6)\times10^{-20}$	0.05151(7)	0.061(2)	-0.00248(6)	-0.00417(1)	19.14(2)
20	R(19)	2212.625547(1)	$5.46(6)\times10^{-20}$	0.05078(9)	0.0581(1)	-0.00211(7)	-0.00478(1)	19.12(2)
21	R(20)	2215.704655(1)	$3.99(5)\times10^{-20}$	0.05054(11)	0.0566(1)	-0.00228(9)	-0.00525(1)	19.07(1)
22	R(21)	2218.745697(1)	$2.87(4)\times10^{-20}$	0.0504(14)	0.0544(1)	-0.0027(11)	-0.00516(1)	18.87(1)
23	R(22)	2221.748465(1)	$2.03(3)\times10^{-20}$	0.05053(17)	0.0527(1)	-0.0025(15)	-0.00512(1)	18.66(2)
24	R(23)	2224.712904(2)	$1.41(2)\times10^{-20}$	0.04999(23)	0.0511(1)	-0.00279(21)	-0.00514(1)	18.46(4)

[a]liens position (cm^{-1}), [b]line intensities (cm^{-1}/molecule. cm^{-2}), [c]air-and [d]self broadening ([cm^{-1}/ (molecule cm^{-2})]), [e]air-and [f]self-shift coefficients (cm^{-1} atm^{-1}), [g]Einstein-A coefficients (s^{-1}).

For most cases, our measured line parameters are comparable to the line-shape study of CO-CO and air-broadened CO in the 0→1 and 0→2 bands reported by Zou and Varanasi [25]. L. Regalia-Jarlot *et al.* [26] have studied air-broadened line widths for the 0→1 band of $^{12}C^{16}O$, which were also comparable to our measured air-broadening coefficients.

The measurements of line strengths (intensities) in this work and in the Zou and Varanasi [25] study both used the Voigt line profile. Line intensities in HITRAN are currently based on the study reported by Gang Li *et al.*[61]. From Figure 4.2, it is evident that my measured results show very good agreement with the HITRAN [61] database, GEISA (2015) database and the study reported by Zou and Varanasi [25]. In Figure 4.3, ratios of line intensities are plotted as a function of m (for P-branch, m = -J and J+1 for R-branch). The results of our measured line intensities over the values of the HITRAN [61], GEISA databases (2015) and the data reported by Zou and Varanasi [25] give the ratio of line intensities, and the mean values of these ratios to be 1.0077, 1.0079 and 0.9628, respectively. It is clear that the current study validate the line intensity values of CO with the HITRAN and GEISA databases, whereas the values reported by Zou and Varanasi deviate slightly from our results.

Air-broadening coefficients of $^{12}C^{16}O$ for the fundamental band have been reported in few prior studies. Air-broadened coefficients of CO reported by HITRAN [22], Zou and Varanasi [25] and L. Regalia-Jarlot *et al*.[26] are compared with my present study, and are shown in Figure 4.4. Air-broadening coefficients of $^{12}C^{16}O$ in HITRAN are currently based on the study reported by L.S. Rothman *et al*. [22]. Our present study shows strong agreement with the results of the earlier studies [25, 26] and the HITRAN database even though all the measurements were done using different instruments and methods. In

addition, the ratios of air-broadening coefficients of CO between the present study and the HITRAN database and the Zou & Varanasi study are shown in Figure 4.5. The means of the ratios are 1.006 and 1.013, respectively. From this comparison, it is obvious that the ratio our measured air-broadening values over HITRAN (1.006) reflect better agreement than the ratio with the results reported by Zou and Varanasi (1.013) [25].

Air-induced pressure-shift coefficients of CO for the fundamental band have only been reported in the Zou and Varanasi study. So, the values of air-shift coefficients in HITRAN are currently based on the study reported by Zou and Varanasi [25]. In Figure 4.6, the measured air-induced pressure shift coefficients are plotted as a function of m. The results of the present study were compared with the study reported by Zou and Varanasi, where they measured the spectral lines with the m index between -23 to 26. The present study shows good agreement with the Zou and Varanasi data in terms of the general trend of pressure shifts, but our results disagree with the reported values [25]. Measurements of line shifts are always difficult and highly depend on the instrumental setup and the technique used by scientists. Different calibration standard used by different experimental setups occur systematic shift in the data sets. Therefore, the differences observed between the air-shift measurements reported by Zou and Varanasi [25] and my results is not unexpected. The spectral line intensity (cm^{-1}/ molecule·cm^{-2}) of the molecular transition between *i* and *j* ro-vibrational energy levels can be expressed as:

$$S_{ij} = I_a \frac{A_{ij}}{8\pi c \nu^2{}_{ij}} \frac{g' e^{-c_2 E''/T} (1 - e^{c_2 \nu_{ij}/T})}{Q(T)} \tag{4.4}$$

where I_a is the natural abundance (99.998% for $^{12}C^{16}O$), g' is the statistic weight of the upper state, E'' is the lower state energy, c_2 is the second radiation constant ($c_2 =$

hc/k) related to the speed of light, Boltzmann constant and Planck constant, Q(T) is the total internal partition sum (107.12 for CO).

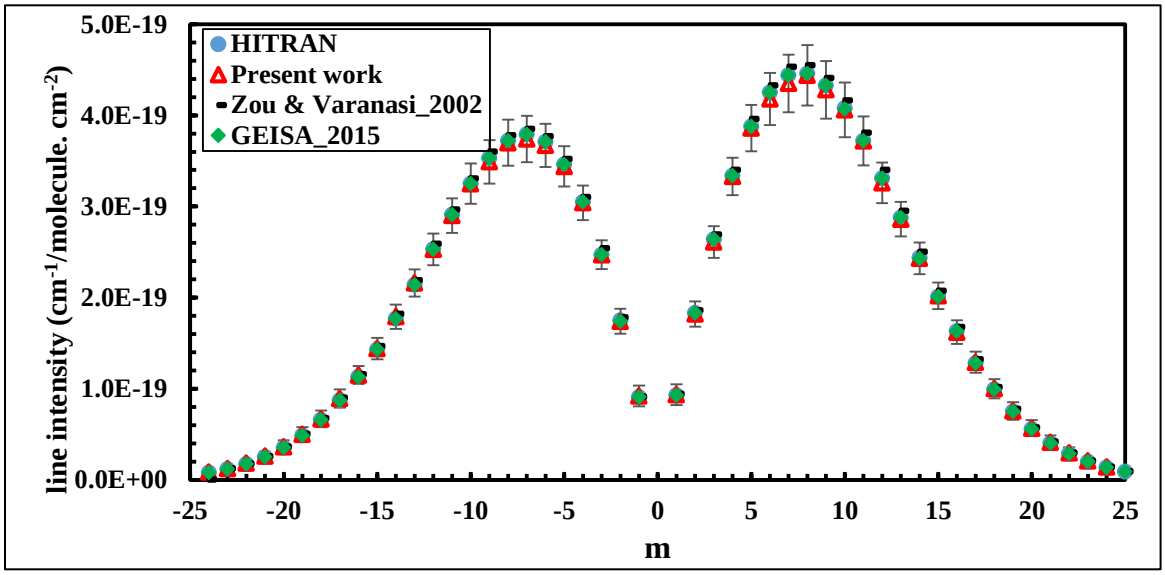

Figure 4.2: Measured line intensities of this work using the Voigt profile, and those from the study by Zou &Varanasi [25], the HITRAN [61] and the GEISA_2015 databases.

A_{ij} (s^{-1}) is a mathematical quantity which defines the probability of emission or absorption of light during a molecular transition. This mathematical quantity is commonly known as the Einstein-A coefficient. In this study, I used the equation (4.4) to calculate the Einstein-A coefficients and I compared our calculated results with the values from the HITRAN database. Both the data stored in HITRAN and my calculated values agree nicely with each other, and in terms of percentage of error our calculated values show good accuracy (3.62%).

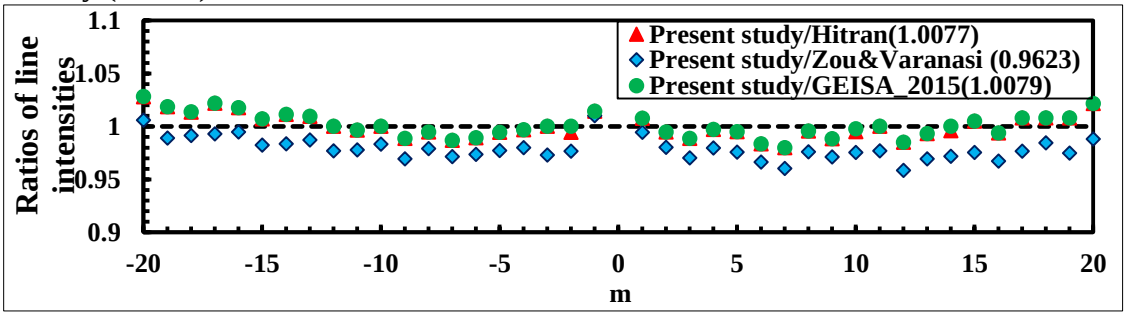

Figure 4.3: Ratios of line intensities between the values obtained in the present study and those from HITRAN [61] and GEISA_2015, as well as the values of the present study versus the study reported by Zou and Varanasi [25].

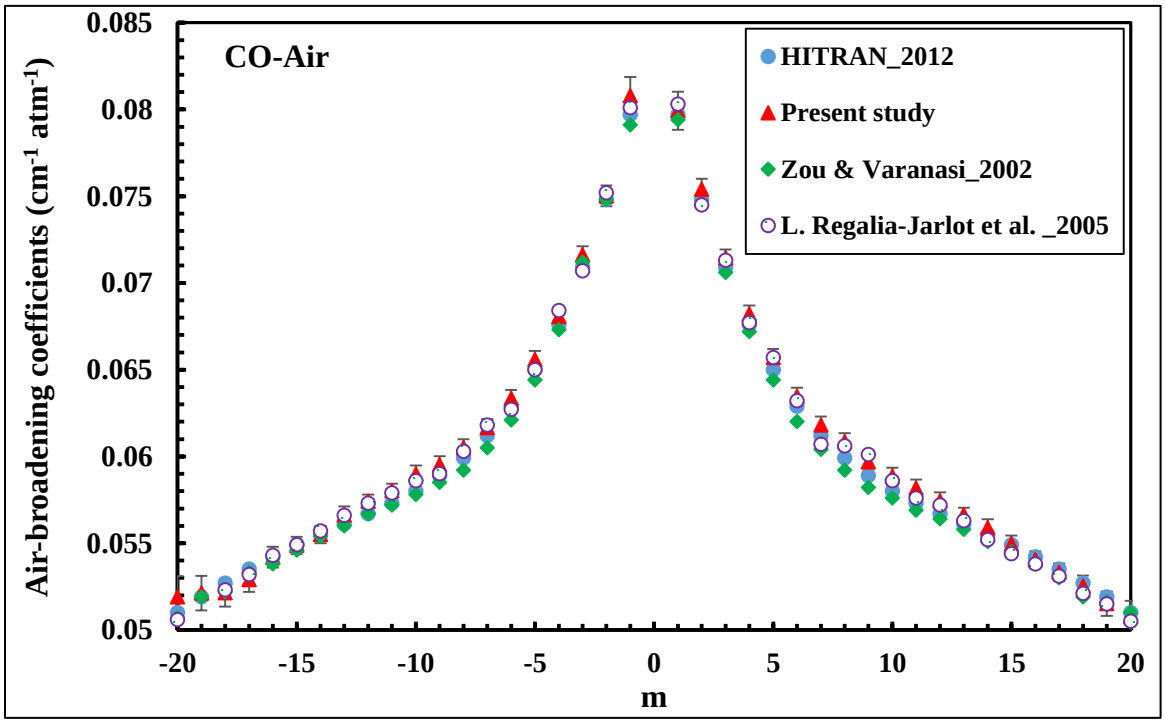

Figure 4.4:Comparision of measured air-broadening coefficients with HITRAN database [22], and the studies by Zou and Varanasi [25] and L.Regalia-Jarlot *et al*. [26] for the 0→1band.

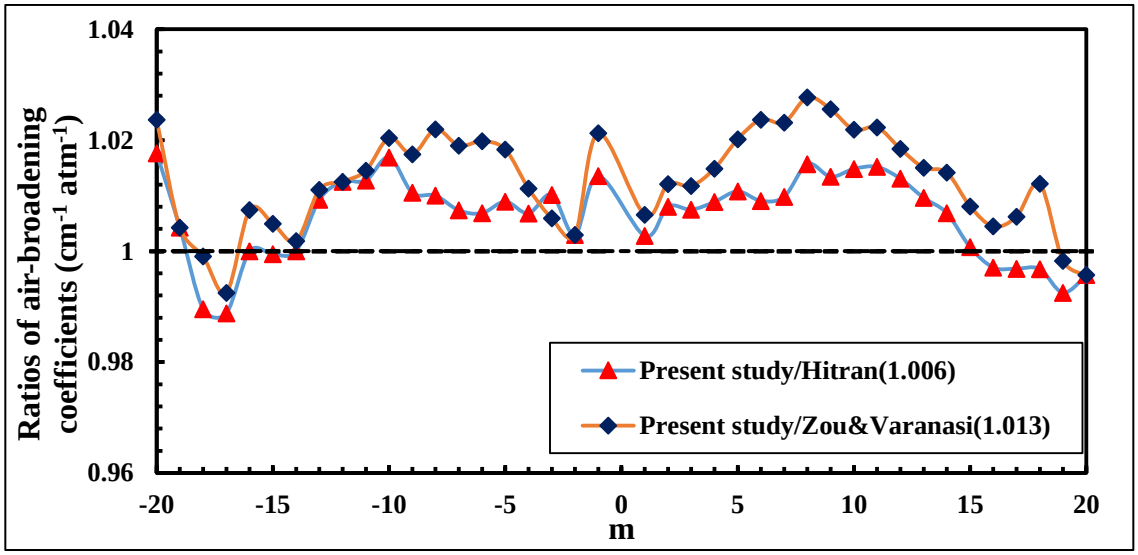

Figure 4.5: Ratios of air-broadening coefficients between the present study and the HITRAN database [22] and the Zou & Varanasi [25] study. My results are in better agreement with HITRAN data.

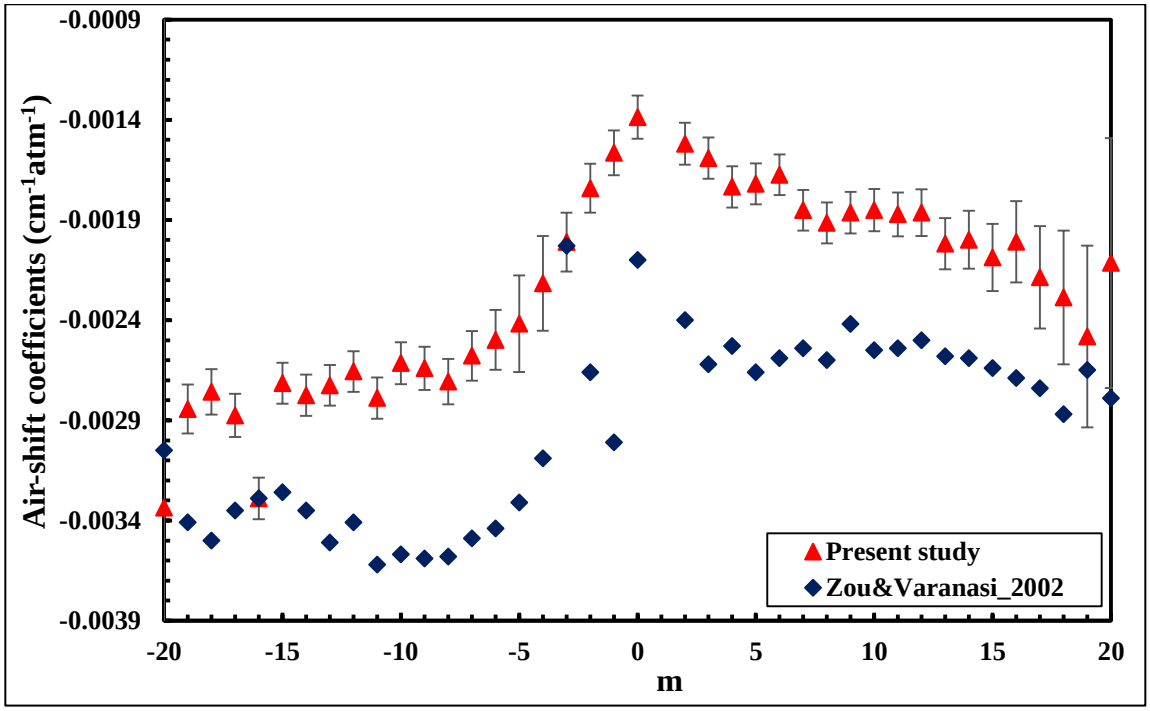

Figure 4.6: Plot of the air-induced pressure-shift coefficients of the present study, as well as those from the study of Zou and Varanasi [25] versus m of the 0→1 band. The systematic shift of these two sets of data occurs due to the different calibration standards used in the analysis.

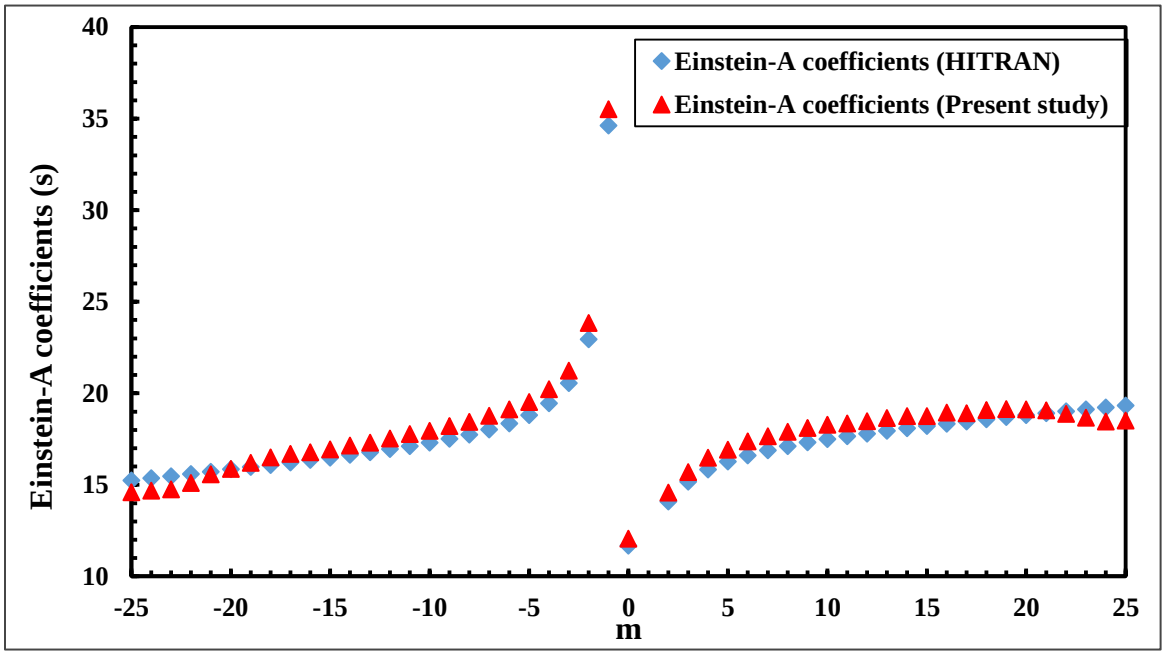

Figure 4.7: Comparison of Einstein-A coefficients between our measured values and HITRAN [24] data.

Table 4.4: Self-broadening ($cm^{-1}atm^{-1}$) and self-shift ($cm^{-1}atm^{-1}$) coefficients of six spectra of pure CO in the fundamental (1-0) band for Voigt, Speed-Dependent Voigt (SDV) and Rautian profiles.

m	Lines	Voigt		SDV		Rautian	
		$\mathbf{b_L^o}$(self) ($cm^{-1}atm^{-1}$)	$\boldsymbol{\delta^o}$(self) ($cm^{-1}atm^{-1}$)	$\mathbf{b_L^o}$(self) ($cm^{-1}atm^{-1}$)	$\boldsymbol{\delta^o}$(self) ($cm^{-1}atm^{-1}$)	$\mathbf{b_L^o}$(self) ($cm^{-1}atm^{-1}$)	$\boldsymbol{\delta^o}$(self) ($cm^{-1}atm^{-1}$)
-32	P(32)	0.0407(10)	-0.00391(13)	0.037(19)	-0.00418(13)	0.041(10)	- 0.00394(13)
-31	P(31)	0.0389(5)	-0.00622(7)	0.035(10)	-0.00618(7)	0.039(5)	-0.00624(7)
-30	P(30)	0.0484(4)	-0.00481(5)	0.062(14)	-0.00476(6)	0.048(4)	-0.00483(5)
-29	P(29)	0.0512(2)	-0.00392(3)	0.098(12)	-0.00280(5)	0.051(2)	-0.00393(3)
-28	P(28)	0.0473(2)	-0.00444(2)	0.047(3)	-0.00453(2)	0.047(2)	-0.00446(2)
-27	P(27)	0.0472(1)	-0.00494(1)	0.046(2)	-0.00503(1)	0.047(1)	-0.00496(1)
-26	P(26)	0.0486(1)	-0.00516(1)	0.048(1)	-0.00524(1)	0.049(1)	-0.00517(1)
-25	P(25)	0.0497(1)	-0.00509(1)	0.049(1)	-0.00517(1)	0.050(1)	-0.00511(1)
-24	P(24)	0.0518(1)	-0.00512(1)	0.053(1)	-0.00518(1)	0.052(1)	-0.00512(1)
-23	P(23)	0.0523(1)	-0.00498(1)	0.052(1)	-0.00505(1)	0.052(1)	-0.00499(1)
-22	P(22)	0.0541(1)	-0.00478(1)	0.054(1)	-0.00484(1)	0.054(1)	-0.00478(1)
-21	P(21)	0.0569(1)	-0.00462(1)	0.057(1)	-0.00468(1)	0.057(1)	-0.00462(1)
-20	P(20)	0.0594(1)	-0.00453(1)	0.059(1)	-0.00459(1)	0.059(1)	-0.00453(1)
-19	P(19)	0.0629(1)	-0.00394(1)	0.059(3)	-0.00400(1)	0.063(1)	-0.00394(1)
-18	P(18)	0.0590(2)	-0.00546(1)	0.072(2)	-0.00516(1)	0.059(2)	-0.00538(1)
-17	P(17)	0.0584(2)	-0.00431(1)	0.075(4)	-0.00439(1)	0.058(2)	-0.00431(1)
-16	P(16)	0.0631(2)	-0.00408(1)	0.068(6)	-0.00417(1)	0.063(2)	-0.00412(1)
-15	P(15)	0.0655(3)	-0.00503(1)	0.068(6)	-0.00499(1)	0.065(3)	-0.00503(1)
-14	P(14)	0.0675(3)	-0.00590(1)	0.069(5)	-0.00581(1)	0.067(3)	-0.00586(1)
-13	P(13)	0.0740(3)	-0.00358(1)	0.068(6)	-0.00381(1)	0.074(3)	-0.00366(1)
-12	P(12)	0.0791(3)	-0.00318(1)	0.070(6)	-0.00351(1)	0.079(3)	-0.00338(1)
-11	P(11)	0.0876(3)	-0.00670(1)	0.084(6)	-0.00680(1)	0.087(3)	-0.00666(1)
-10	P(10)	0.0883(4)	-0.00525(1)	0.077(7)	-0.00570(1)	0.088(4)	-0.00526(1)
-9	P(9)	0.0871(4)	-0.00582(1)	0.082(7)	-0.00607(1)	0.087(4)	-0.00579(1)
-8	P(8)	0.0910(4)	-0.00632(1)	0.085(7)	-0.00649(1)	0.091(4)	-0.00629(1)
-7	P(7)	0.0913(4)	-0.00466(1)	0.079(8)	-0.00489(1)	0.091(4)	-0.00474(1)
-6	P(6)	0.0960(4)	-0.00642(1)	0.087(8)	-0.00646(1)	0.096(4)	-0.00635(1)
-5	P(5)	0.0934(4)	-0.00462(1)	0.082(8)	-0.00462(1)	0.093(4)	-0.00468(1)
-4	P(4)	0.0925(4)	-0.00481(1)	0.082(7)	-0.00465(1)	0.092(4)	-0.00479(1)
-3	P(3)	0.0924(3)	-0.00488(1)	0.084(7)	-0.00475(1)	0.092(3)	-0.00486(1)
-2	P(2)	0.0907(3)	-0.00578(1)	0.092(7)	-0.00571(1)	0.091(3)	-0.00567(1)
-1	P(1)	0.0915(2)	-0.00340(1)	0.102(4)	-0.00374(1)	0.092(2)	-0.00343(1)
1	R(0)	0.0924(2)	-0.00429(1)	0.104(3)	-0.00389(1)	0.092(2)	-0.00428(1)
2	R(1)	0.0924(3)	-0.00560(1)	0.111(7)	-0.00456(1)	0.092(3)	-0.00550(1)
3	R(2)	0.0865(4)	-0.00279(1)	0.085(7)	-0.00298(1)	0.087(4)	-0.00288(1)

4	R(3)	0.0871(4)	-0.00291(1)	0.080(7)	-0.00327(1)	0.087(4)	-0.0030(1)
5	R(4)	0.0896(4)	-0.00319(1)	0.081(7)	-0.00343(1)	0.090(4)	-0.00319(1)
6	R(5)	0.0913(4)	-0.00212(1)	0.082(8)	-0.00230(1)	0.091(4)	-0.00221(1)
7	R(6)	0.0927(4)	-0.00315(1)	0.080(8)	-0.00325(1)	0.093(4)	-0.00319(1)
8	R(7)	0.0913(4)	-0.00379(1)	0.077(8)	-0.00372(1)	0.091(4)	-0.00375(1)
9	R(8)	0.0841(4)	-0.00467(1)	0.075(7)	-0.00442(1)	0.084(4)	-0.00455(1)
10	R(9)	0.0853(4)	-0.00317(1)	0.078(7)	-0.00312(1)	0.085(4)	-0.00324(1)
11	R(10)	0.0823(4)	-0.00369(1)	0.074(6)	-0.00348(1)	0.082(4)	-0.00367(1)
12	R(11)	0.0805(4)	-0.00317(1)	0.076(6)	-0.00311(1)	0.080(4)	-0.00322(1)
13	R(12)	0.0776(3)	-0.00348(1)	0.072(6)	-0.00333(1)	0.077(3)	-0.00349(1)
14	R(13)	0.0745(3)	-0.00420(1)	0.068(5)	-0.00398(1)	0.075(3)	-0.00416(1)
15	R(14)	0.0710(3)	-0.00366(1)	0.068(5)	-0.00361(1)	0.071(3)	-0.00368(1)
16	R(15)	0.0692(3)	-0.00374(1)	0.067(5)	-0.00372(1)	0.069(3)	-0.00374(1)
17	R(16)	0.0654(2)	-0.00431(1)	0.064(5)	-0.00430(1)	0.065(2)	-0.00428(1)
18	R(17)	0.0632(2)	-0.00399(1)	0.065(5)	-0.00410(1)	0.063(2)	-0.00400(1)
19	R(18)	0.0610(2)	-0.00417(1)	0.066(4)	-0.00436(1)	0.061(2)	-0.00419(1)
20	R(19)	0.0581(1)	-0.00478(1)	0.063(3)	-0.00491(1)	0.058(1)	-0.00477(1)
21	R(20)	0.0566(1)	-0.00525(1)	0.059(2)	-0.00533(1)	0.057(1)	-0.00525(1)
22	R(21)	0.0544(1)	-0.00516(1)	0.055(1)	-0.00524(1)	0.054(1)	-0.00516(1)
23	R(22)	0.0527(1)	-0.00512(1)	0.053(1)	-0.00520(1)	0.053(1)	-0.00512(1)
24	R(23)	0.0511(1)	-0.00514(1)	0.051(1)	-0.00521(1)	0.051(1)	-0.00514(1)
25	R(24)	0.0501(1)	-0.00505(1)	0.050(1)	-0.00513(1)	0.050(1)	-0.00506(1)
26	R(25)	0.0490(1)	-0.00520(1)	0.049(1)	-0.00528(1)	0.049(1)	-0.00521(1)
27	R(26)	0.0480(1)	-0.00513(1)	0.048(1)	-0.00522(1)	0.048(1)	-0.00515(1)
28	R(27)	0.0473(1)	-0.00521(1)	0.047(2)	-0.00529(1)	0.047(1)	-0.00523(1)
29	R(28)	0.0459(1)	-0.00538(2)	0.046(3)	-0.00546(2)	0.046(1)	-0.00540(2)
30	R(29)	0.0451(2)	-0.00539(3)	0.045(5)	-0.00547(3)	0.045(2)	-0.00541(3)
31	R(30)	0.0451(3)	-0.00498(4)	0.046(9)	-0.00504(5)	0.045(3)	-0.00500(4)
32	R(31)	0.0442(5)	-0.00521(7)	0.047(16)	-0.00525(7)	0.044(5)	-0.00523(7)
33	R(32)	0.0456(9)	-0.00354(11)	0.049(29)	-0.00355(12)	0.045(9)	-0.00357(11)

Most spectroscopic studies of CO did not compare self-broadening and self-shift coefficients of CO for 0→1 band. In this study, the self-broadening and shift coefficients of CO at 296 K for the fundamental band were compared using different line profiles. At first, six room-temperature spectra of pure CO spectra were analyzed. Both self-broadening and self-shift coefficients were calculated for higher rotational numbers m corresponding

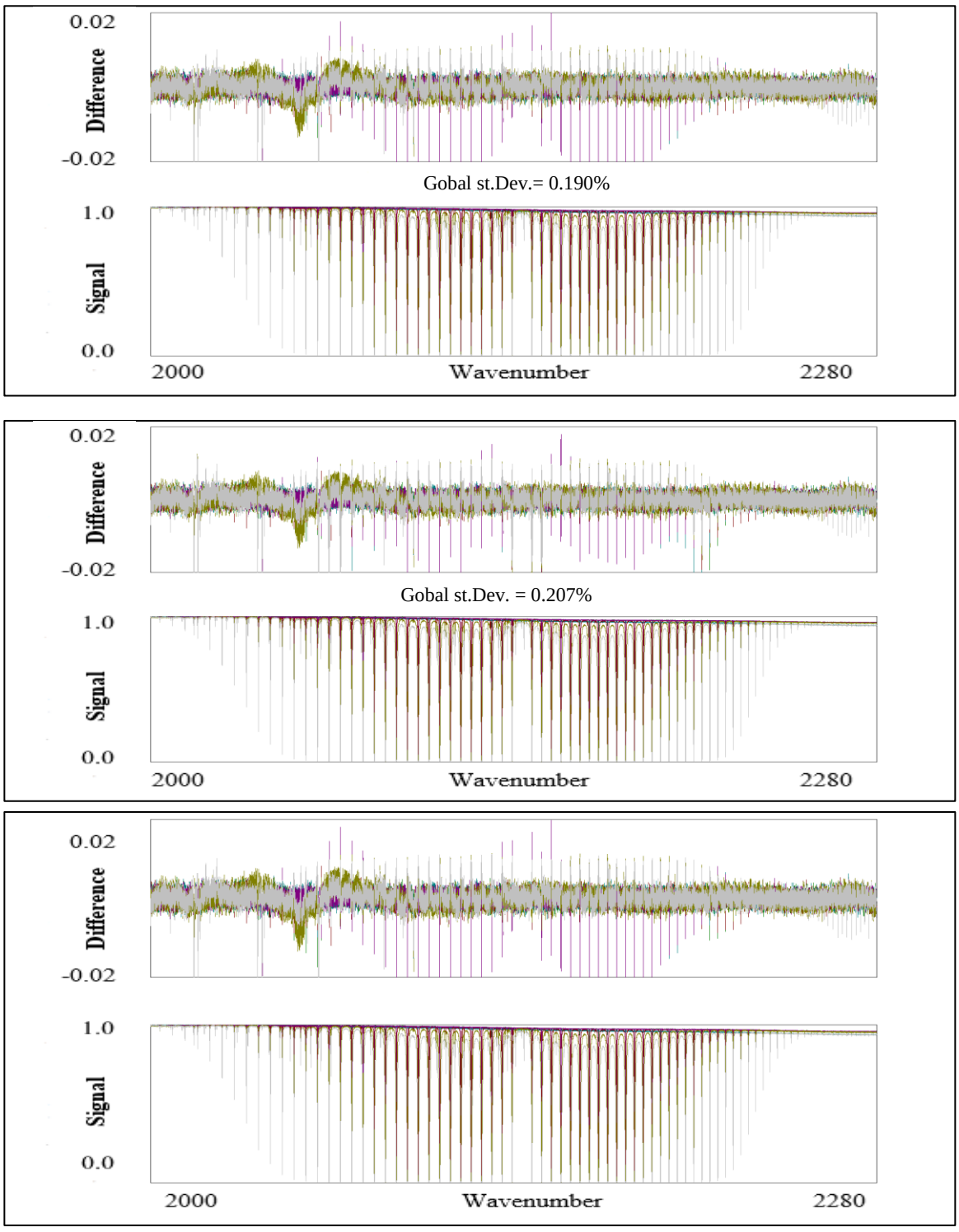

Figure 4.8: In the lower traces of each of the section represent six CO absorption spectra recorded at 296 K (6 self-broadened) for the spectral range 2000 to 2280 cm^{-1}. Different profiles were implemented for their analysis. (a) Voigt (b) Speed-dependent Voigt (SDV) and (c) Rautian profile. The upper traces represent the weighted fit residuals. The standard deviations shown here are 0.190%, 0.270% and 0.190%, respectively.

to |m| < 20 were saturated. Saturation happens when the line undergoes strong absorption, and thereby results in zero transmission of light of that frequency. As most of the published papers reported their results between -24 to 24 rotational quantum number, I was not able to compare my high rotational number values with previous studies. . In Figure 4.8 six spectra of pure CO are overlaid for Voigt, Speed-dependent Voigt (SDV) and Rautian profiles, and the weighted residuals of these profiles are 0.190%, 0.207% and 0.190%, respectively.

The difference between experimental and calculated spectra in SDV profile is larger than those using the other two profiles. The self-broadening coefficients and the self-shift coefficients of SDV model slightly deviate from the Voigt and the Rautian profiles, which is illustrated in Figure 4.9 and 4.10.

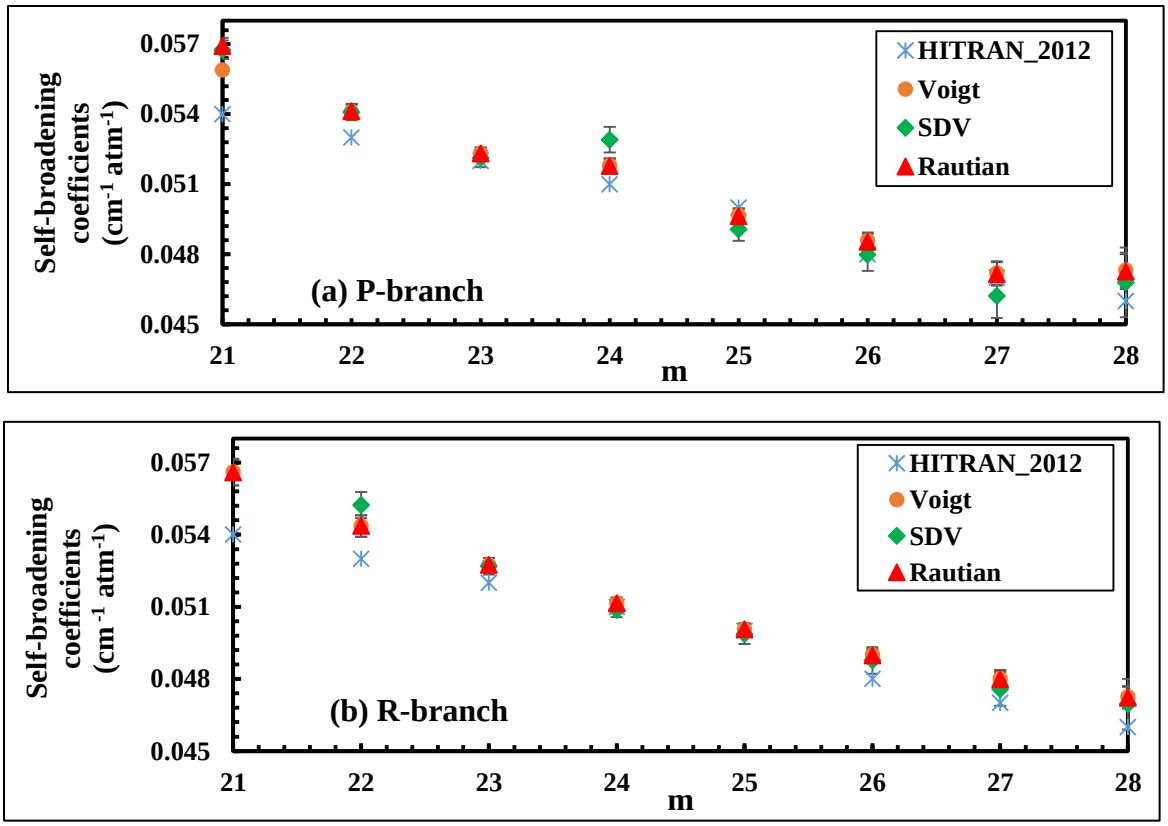

Figure 4.9: Comparison of the self-broadening coefficients of $^{12}C^{16}O$ in the 1-0 for different line models. (a) P-branch (b) R-branch, as well as compared with L.S. Rothman *et al.*[22], and later their reported results were listed in the HITRAN database.

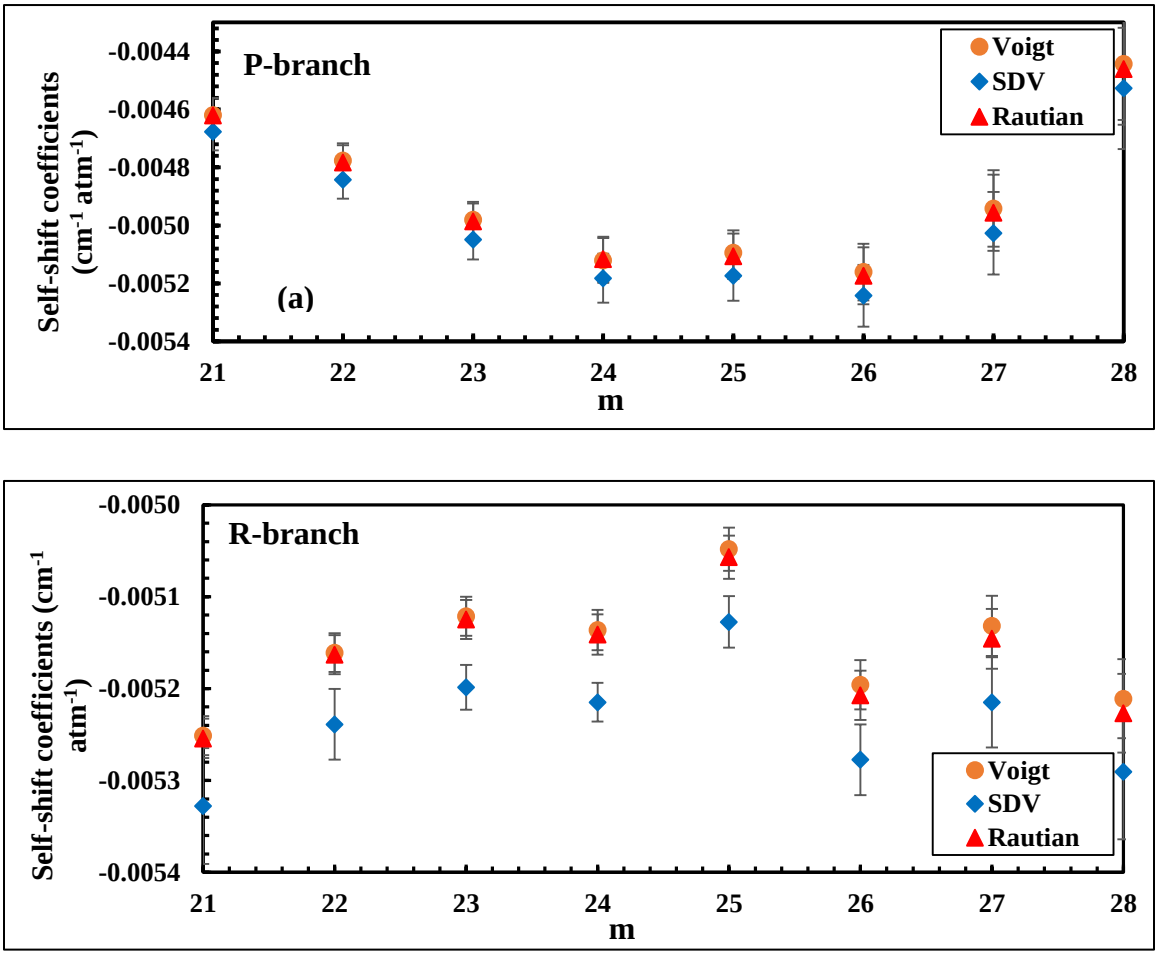

Figure 4.10: Comparison of the self-shift coefficients of $^{12}C^{16}O$ in the 1-0 for different line profiles.

4.3. Exponential Power Gap Law (EPG) for line-mixing calculation

The EPG law describes the relaxation matrix by calculating the collisional transfer rates of a lower rotational quantum energy state *k* to a higher energy state *j*. The collisional transfer rate κ_{jk} can be described by [31]:

$$\kappa_{jk} = a\left[\frac{|\Delta E_{jk}|}{B_0}\right]^{-b} \exp\left(\frac{-c|\Delta E_{jk}|}{KT}\right) \tag{4.5}$$

where ΔE_{jk} is the energy gap between the two states, B_o is the rotational constant, T is the temperature, K is the Boltzmann constant, and a, b, c are the unknown parameters, and their values need to be optimized. Transitions from j to k are calculated through detailed balance equation.

$$\rho_k \kappa_{jk} = \rho_j \kappa_{kj} \tag{4.6}$$

ρ_k and ρ_j are the population densities of the rotational energy levels *k* and *j*, respectively. The off-diagonal elements of the relaxation matrix are linked to collisional transfer rates and can be expressed as follows [62]:

$$W_{jk} = -\beta \kappa_{jk} \tag{4.7}$$

where β is a constant and in my present study I used β = 0.55 and 0.60. The diagonal elements (line widths and line shift) of the relaxation matrix is calculated as follows:

$$W_{kk} = \frac{1}{2}\left[\sum_j \kappa_{jk}\right]_{upper} + \frac{1}{2}\left[\sum_j \kappa_{jk}\right]_{lower} \tag{4.8}$$

The weak line-mixing coefficients (Y_{ok}) can be obtained from the following equation:

$$Y_{ok}(T) = 2\sum_{j\neq k} \frac{\mu_j}{\mu_k} \frac{w_{jk}}{\upsilon_k - \upsilon_j} \tag{4.9}$$

where μ_j and μ_k are the optical transitions of dipole matrix elements.

Theoretically calculated line-mixing coefficients from EPG law and experimentally determined values from different line profiles are listed in Table 4.5.

Table 4.5: Line-mixing coefficients (atm^{-1}) obtained from different line-shape profiles and calculated from the EPG model.

m	Lines	Voigt	SDV	Rautian	EPG(CO-CO)	EPG(Air-CO)
-18	P(18)	0.00531	0.00504	0.00501	0.004150	0.003728
-17	P(17)	0.00046	0.00051	0.00049	0.004087	0.003666
-16	P(16)	0.00073	0.00095	0.00087	0.004005	0.003585
-15	P(15)	0.00359	0.00354	0.00357	0.003909	0.003488
-14	P(14)	0.00455	0.00443	0.00447	0.003791	0.003368
-13	P(13)	0.00040	0.00061	0.00052	0.003647	0.003222
-12	P(12)	0.00026	0.00054	0.00049	0.003474	0.003045
-11	P(11)	0.00576	0.00558	0.00567	0.003266	0.002832
-10	P(10)	0.00294	0.00290	0.00295	0.003013	0.002573
-9	P(9)	0.00309	0.00310	0.00305	0.002708	0.002260
-8	P(8)	0.00287	0.00278	0.00283	0.002335	0.001878
-7	P(7)	0.00036	0.00047	0.00043	0.001880	0.001412
-6	P(6)	0.00173	0.00156	0.00166	0.001322	0.000838
-5	P(5)	-0.00109	-0.00099	-0.00103	0.000632	0.000121
-4	P(4)	-0.00150	-0.00155	-0.00154	-0.000217	-0.000787
-3	P(3)	-0.00213	-0.00218	-0.00216	-0.001247	-0.001972
-2	P(2)	-0.00122	-0.00142	-0.00140	-0.002544	-0.003708
-1	P(1)	-0.00534	-0.00528	-0.00525	-0.011171	-0.011305
1	R(0)	0.00850	0.00853	0.00850	0.027003	-0.019440
2	R(1)	0.00943	0.00930	0.00925	0.013982	0.023243
3	R(2)	0.00341	0.00348	0.00352	0.008719	0.010881
4	R(3)	0.00219	0.00230	0.00227	0.005502	0.006698
5	R(4)	0.00173	0.00171	0.00173	0.003249	0.004083
6	R(5)	-0.00020	-0.00011	-0.00013	0.001554	0.002315
7	R(6)	-0.00024	-0.00019	-0.00021	0.000223	0.001047
8	R(7)	-0.00042	-0.00046	-0.00046	-0.000851	0.000032
9	R(8)	-0.00052	-0.00070	-0.00063	-0.001737	-0.000763
10	R(9)	-0.00231	-0.00220	-0.00224	-0.002482	-0.001412
11	R(10)	-0.00232	-0.00231	-0.00234	-0.003110	-0.001994
12	R(11)	-0.00351	-0.00345	-0.00346	-0.003639	-0.002440
13	R(12)	-0.00356	-0.00353	-0.00355	-0.004095	-0.002832
14	R(13)	-0.00326	-0.00332	-0.00331	-0.004495	-0.003230
15	R(14)	-0.00451	-0.00450	-0.00448	-0.004841	-0.003558
16	R(15)	-0.00461	-0.00458	-0.00461	-0.005141	-0.003839
17	R(16)	-0.00373	-0.00381	-0.00379	-0.005400	-0.004067
18	R(17)	-0.00477	-0.00477	-0.00475	-0.005629	-0.004270
19	R(18)	-0.00467	-0.00466	-0.00462	-0.005836	-0.004520
20	R(19)	-0.00255	-0.00260	-0.00264	-0.006018	-0.004728

In the EPG model, a nonlinear algorithm written in MATLAB was used to find the best optimized values of a, b, c parameters. The values of a, b, c and β were found by

applying nonlinear least square fit to the sum rule which states that the sum of relaxation matrix elements in a column is equal to zero. When the experimental values of broadening coefficients match fourth decimal place to the diagonal elements of the relaxation matrix, the optimized values of these parameters are assume the reported results.

Table 4.6: Optimized values of EPG parameters.

β	Values (CO-CO)	Parameters	Values (Air-CO)	β
0.6	0.04219332(3)	a	0.02970517(4)	0.55
	0.45056420(6)	b	0.35939840(6)	
	1.02971900(7)	c	1.098497009(8)	

Weak self-broadened line-mixing coefficients of the present experimental work and calculated theoretical (EPG) values are compared with those from Devi *et al*. [18] in Figure 4.11. My theoretically calculated CO-CO values for the 0→1 band do not show exactly same results as the Devi *et al*. [18] data because their spectra were recorded for 0→2 band (as 0→1 band results are not available). Most of the experimentally calculated values from different profiles (Voigt, SDV and Rautian) are slightly deviated from the theoretical values due to the saturation of the spectral lines ($-20 \geq m \leq 20$) both in P- and R-branches.

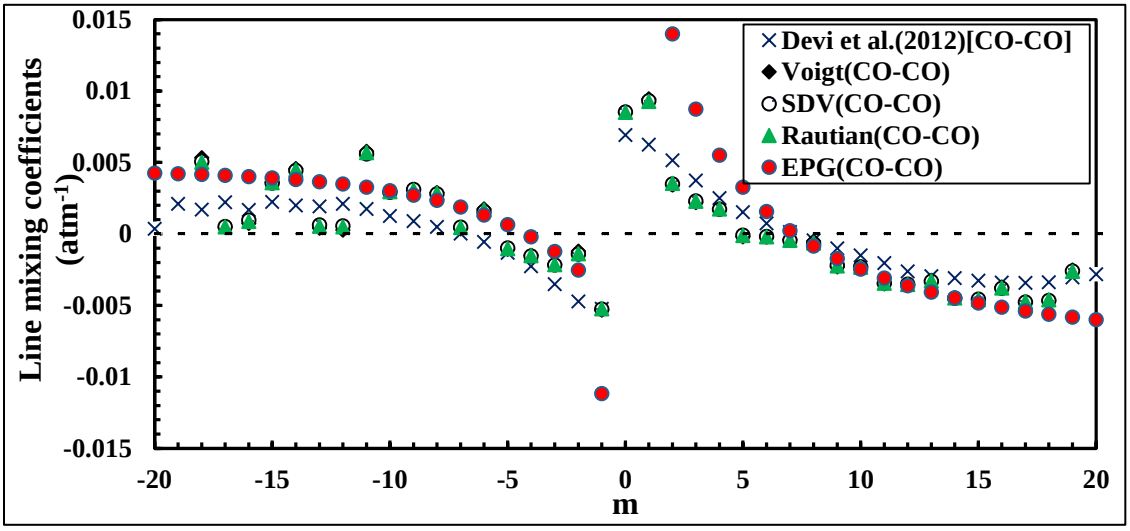

Figure 4.11: Weak self-broadened line mixing coefficients for different line-shape models compared with EPG method.

4.4. Energy Corrected Sudden Approximation (ECS)

The Energy Corrected Sudden (ECS) Approximation [38] is an angular momentum (L) dependent scaling law which is considered as an updated version of the Infinite-Order sudden law (IOS) [44] by including an adiabaticity factor. This law is applicable when the collisions among the molecules are not sudden [38, 44, 63] and the deviated spectral lines are not assumed as Lorentzian. For a diatomic molecule like CO perturbed by other molecules, the off-diagonal relaxation matrix elements for two transitions $J_f \leftarrow J_i$ and $J'_f \leftarrow J'_i$ ($J'_i < J_i$) can be expressed as:

$$\langle J_i' J_f' | W(T) | J_i J_f \rangle = (2J_i' + 1)\sqrt{(2J_f + 1)(2J_f' + 1)}$$

$$\times \sum_{Leven \neq 0} \begin{pmatrix} J_i & L & J_i' \\ 0 & 0 & 0 \end{pmatrix} \begin{pmatrix} J_f & L & J_f' \\ 0 & 0 & 0 \end{pmatrix} \begin{Bmatrix} J_i & J_f & 1 \\ J_f' & J_i' & L \end{Bmatrix} \times (2L+1)\frac{\Omega_J}{\Omega_L} Q_L \quad (4.10)$$

where $\begin{pmatrix} \cdots \\ \cdots \end{pmatrix}$ and $\begin{Bmatrix} \cdots \\ \cdots \end{Bmatrix}$ are representing Wigner 3J and 6J coefficients. Ω_J and Ω_J are the adiabaticity factor and the basic rate, respectively, and they can be written as:

$$\Omega_J = \left\{1 + \frac{1}{24}\left[\frac{\Delta\omega_j \, d_c}{\bar{v}}\right]^2\right\}^{-2} \quad (4.11)$$

$$\Omega_L = A\left[\frac{E_L}{B}\right]^{-\lambda} exp\left(-\beta\frac{E_L}{K_B T}\right) \quad (4.12)$$

In the above equations, $\Delta\omega_j$ is the difference of energy between the rotational energy levels. $d_c, \bar{v}, E_L, B$ are the scaling length, mean relative velocity in CO-air collisions, and rotational constant, respectively. The mean relative velocity ($\bar{v} = \sqrt{8K_B T/\pi\mu}$) is related to the reduced mass (μ) of the active and the perturbed molecules.

Table 4.7: Self- and air-broadened line-mixing coefficients (atm^{-1}) of CO in the R branch calculated from EPG and ECS models.

m	Lines	ECS(Air-CO)	ECS(CO-CO)	EPG (CO-CO)	EPG (Air-CO)
1	R(0)	0.017308	0.018973	0.027003	0.023243
2	R(1)	0.011871	0.013018	0.013982	0.010881
3	R(2)	0.008664	0.009508	0.008719	0.006698
4	R(3)	0.006151	0.006757	0.005502	0.004083
5	R(4)	0.004075	0.004484	0.003249	0.002315
6	R(5)	0.002363	0.002606	0.001554	0.001047
7	R(6)	0.000970	0.001075	0.000223	0.000032
8	R(7)	-0.000147	-0.000154	-0.000851	-0.000763
9	R(8)	-0.001039	-0.001138	-0.001737	-0.001412
10	R(9)	-0.001755	-0.001928	-0.002482	-0.001994
11	R(10)	-0.002330	-0.002562	-0.003110	-0.002440
12	R(11)	-0.002795	-0.003075	-0.003639	-0.002832
13	R(12)	-0.003181	-0.003499	-0.004095	-0.003230
14	R(13)	-0.003508	-0.003860	-0.004495	-0.003558
15	R(14)	-0.003785	-0.004164	-0.004841	-0.003839
16	R(15)	-0.004020	-0.004421	-0.005141	-0.004067
17	R(16)	-0.004222	-0.004643	-0.005400	-0.004270
18	R(17)	-0.004404	-0.004842	-0.005629	-0.004520
19	R(18)	-0.004584	-0.005039	-0.005836	-0.004728
20	R(19)	-0.004786	-0.005260	-0.006018	-0.004915

The ECS approximation depends on adjustable parameters d_c (cm), A $(cm^{-1}atm^{-1})$, λ and β which need to be optimized. For that, a MATLAB code was used by considering the measured broadening coefficients. By using the ECS law, in our present study, the line-mixing coefficients in the R-branch show good agreement and the best optimized values of d_c , A, λ and β generated by the program are 3.8, 0.00315, 0.55 and 0.065, respectively.

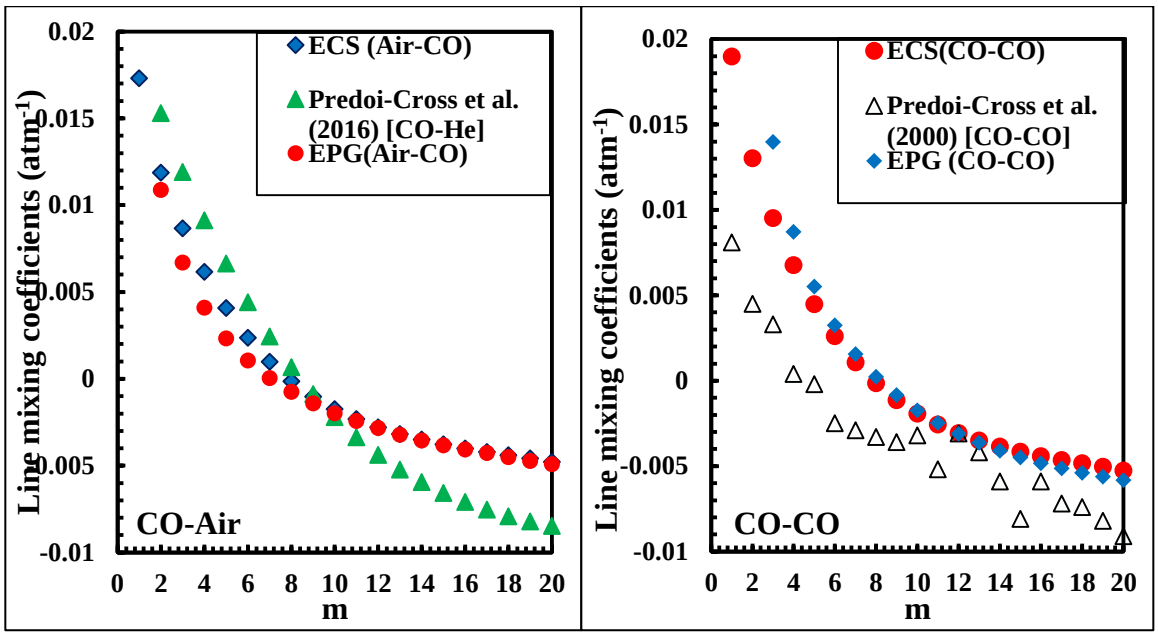

Figure 4.12. Weak self- and air-mixed line mixing coefficients in the R-branch compared with previous studies using ECS and EPG methods.

Figure 4.12 shows line-mixing coefficients of the spectra of pure and air-mixed CO in the R-branch, and are compared with those of Predoi-Cross *et al*. [31, 64]. In reference [31], line-mixing coefficients of self-broadened spectra were calculated from ECS model for $0 \rightarrow 2$ band, whereas a very recent publication by Predoi-Cross *et al*. [64] considered EPG model in order to calculate the line-mixing coefficients of CO spectra broadened by helium (He). Line-mixing data reported for the $0 \rightarrow 2$ band [64] deviate from our calculated values. It is important to note that, self- and air-broadened line-mixing coefficients obtained from this study with the ECS and EPG law are showing good agreement with each other.

4.5. Line-shape study of pure and air-mixed CO spectra between 296 and 79 K

17 spectra of air-mixed CO and 14 spectra of pure CO were considered for analysis of the temperature-dependence broadening and shift coefficients at different temperatures

ranging from 296 to 79 K. Physical conditions of these spectra are listed in Tables 4.8 and 4.9. Temperature-dependent air-broadening, air- and self-shift coefficients of these spectra are listed in Tables 4.10, 4.11 and 4.12.

Table 4.8: Physical conditions of 17 spectra of air-mixed CO.

Temperature (K)	Gas	Path length (cm)	Pressure (Torr)	Volume Mixing Ratio (VMR)
296.92	CO-Air	4.305	619.61	0.00718
297.02	CO-Air	4.305	241.41	0.00280
297.13	CO-Air	4.305	128.90	0.00150
297.19	CO-Air	4.305	65.28	0.00076
230.83	CO-Air	4.305	531.34	0.00760
230.83	CO-Air	4.305	135.90	0.00193
230.83	CO-Air	4.305	37.11	0.00050
182.67	CO-Air	4.305	449.20	0.00870
182.67	CO-Air	4.305	231.59	0.00448
182.67	CO-Air	4.305	110.48	0.00209
182.67	CO-Air	4.305	48.60	0.00093
142.29	CO-Air	4.305	580.82	0.00609
142.29	CO-Air	4.305	359.50	0.00376
79.36	CO-Air	4.305	490.06	0.04304
79.36	CO-Air	4.305	277.01	0.00410
79.36	CO-Air	4.305	85.05	0.00126
79.36	CO-Air	4.305	35.99	0.00053

4.5.1. Spectroscopic results and comparisons with other studies

At first, four spectra at room temperature and three spectra at 230.83 K (in total 7 spectra of air-mixed CO) were fitted simultaneously in order to see how a different temperature affects the air-broadening and air-shift coefficients. Then, the rest of the spectra were gradually added to the fitting process. The Voigt profile was implemented for the measurement of temperature-dependent line-shape parameters of air-broadened CO spectra. Figure 4.13 shows forty (40) ro-vibrational P- and R-branch transitions in the spectral range of 2000 to 2250 cm^{-1}.

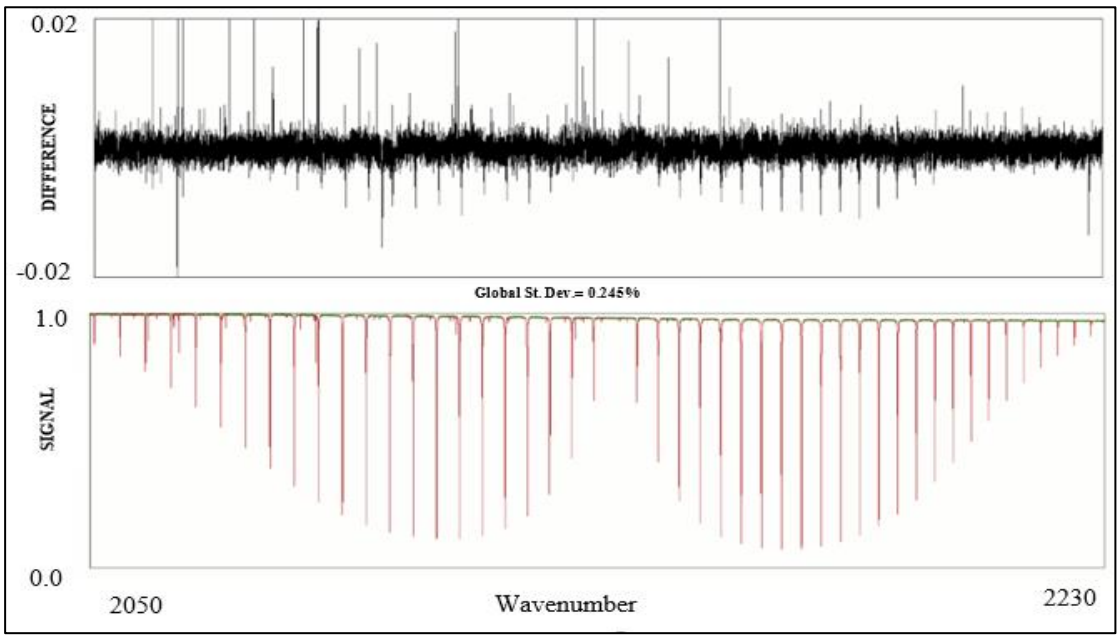

Figure 4.13: In the lower trace, seven spectra of air-mixed CO are shown covering the spectral range of 2050 to 2230 cm^{-1} at 296 and 230 K. The Voigt profile was implemented for this analysis. The upper trace represents the weighted fit residuals. The standard deviation shown here is 0.245%.

Table 4.9: Physical conditions of pure CO spectra at different temperatures.

Temperature (K)	Gas	Path length (cm)	Pressure (Torr)	Volume Mixing Ratio (VMR)
296.41	CO-CO	1.1313	113.81	1
296.36	CO-CO	1.1313	15.63	1
296.36	CO-CO	1.1313	1.02	1
296.42	CO-CO	4.305	0.94	1
230.84	CO-CO	4.305	30.03	1
230.85	CO-CO	4.305	63.10	1
230.85	CO-CO	4.305	100.96	1
230.92	CO-CO	4.305	456.77	1
182.66	CO-CO	4.305	20.02	1
182.66	CO-CO	4.305	65.70	1
182.67	CO-CO	4.305	104.64	1
182.67	CO-CO	4.305	157.55	1
79.73	CO-CO	4.305	36.13	1
79.73	CO-CO	4.305	73.57	1

Table 4.10: Temperature-dependence air-broadening coefficients retrieved with Voigt profile.

Line position (cm^{-1})	**m**	**296K&230 K**	**296K,230K&183K**	**296K,230K,183K& 79K**
2055.400399(12)	-21	0.805(56)	0.900(71)	0.901(66)
2059.914801(9)	-20	0.801(37)	0.899(44)	0.903(42)
2064.397107(7)	-19	0.787(26)	0.882(29)	0.914(28)
2068.847067(5)	-18	0.807(19)	0.943(19)	0.972(19)
2073.264700(4)	-17	0.726(15)	0.932(14)	0.928(14)
2077.649920(4)	-16	0.725(12)	0.934(10)	0.929(11)
2082.002425(3)	-15	0.745(10)	0.930(8)	0.929(9)
2086.322088(3)	-14	0.736(9)	0.904(6)	0.907(8)
2090.608883(2)	-13	0.733(9)	0.847(6)	0.859(7)
2094.862458(2)	-12	0.772(8)	0.784(5)	0.821(6)
2099.082903(2)	-11	0.759(8)	0.689(4)	0.773(6)
2103.269899(2)	-10	0.784(8)	0.584(4)	0.677(6)
2107.423375(2)	-9	0.737(7)	0.498(4)	0.434(6)
2111.543194(2)	-8	0.747(7)	0.438(4)	0.202(6)
2115.629163(2)	-7	0.715(7)	0.390(4)	0.128(5)
2119.681131(2)	-6	0.701(7)	0.367(3)	0.094(5)
2123.699014(2)	-5	0.713(7)	0.361(3)	0.071(5)
2127.682635(2)	-4	0.722(7)	0.465(3)	0.093(5)
2131.631789(2)	-3	0.777(7)	0.633(3)	0.179(5)
2135.546385(3)	-2	0.819(8)	0.867(3)	0.388(5)
2139.426293(4)	-1	0.833(11)	1.047(4)	0.590(7)
2147.081286(4)	1	0.853(10)	1.042(3)	0.545(7)
2150.856170(2)	2	0.809(8)	0.845(3)	0.352(5)
2154.595732(2)	3	0.790(7)	0.555(3)	0.126(5)
2158.299859(2)	4	0.713(7)	0.355(3)	0.062(5)
2161.968418(2)	5	0.673(7)	0.297(3)	0.056(5)
2165.601216(2)	6	0.693(7)	0.294(3)	0.074(5)
2169.198133(2)	7	0.669(7)	0.309(3)	0.094(5)
2172.758988(2)	8	0.705(7)	0.320(3)	0.111(5)
2176.283706(2)	9	0.738(7)	0.361(4)	0.157(5)
2179.772096(2)	10	0.726(7)	0.412(4)	0.290(6)
2183.223925(2)	11	0.760(7)	0.492(4)	0.567(6)
2186.639201(2)	12	0.764(8)	0.593(4)	0.692(6)
2190.017723(2)	13	0.738(8)	0.703(5)	0.753(6)
2193.359304(2)	14	0.737(9)	0.801(5)	0.819(7)
2196.663860(2)	15	0.729(9)	0.879(6)	0.884(8)
2199.931161(3)	16	0.729(10)	0.927(7)	0.926(9)
2203.161155(3)	17	0.718(12)	0.944(9)	0.94(10)
2206.353654(4)	18	0.732(14)	0.942(13)	0.937(13)
2209.508524(5)	19	0.788(18)	0.913(18)	0.963(18)
2212.625566(6)	20	0.798(24)	0.907(26)	0.955(25)

Table 4.11: Temperature-dependence air-shift coefficients retrieved with Voigt profile.

Line position (cm^{-1})	**m**	**296K&230K**	**296K,230K,183K**	**296,230,183&79K**
2055.400399(12)	-21	0.0000116(13)	0.0000081(18)	0.0000101(17)
2059.914801(9)	-20	0.0000015(8)	0.0000095(12)	0.0000053(11)
2064.397107(7)	-19	0.0000024(6)	0.0000077(8)	0.0000073(7)
2068.847067(5)	-18	0.0000037(4)	0.0000109(6)	0.0000119(5)
2073.26470(4)	-17	0.0000111(3)	0.0000153(4)	0.0000133(4)
2077.64992(4)	-16	0.0000095(3)	0.0000118(3)	0.0000129(3)
2082.002425(3)	-15	0.0000074(2)	0.0000111(2)	0.0000122(2)
2086.322088(3)	-14	0.0000061(2)	0.0000109(2)	0.0000118(2)
2090.608883(2)	-13	0.0000046(2)	0.0000094(2)	0.0000127(2)
2094.862458(2)	-12	0.0000080(2)	0.0000113(1)	0.0000142(1)
2099.082903(2)	-11	0.0000020(2)	0.0000079(1)	0.0000118(1)
2103.269899(2)	-10	0.0000034(1)	0.0000092(1)	0.0000128(1)
2107.423375(2)	-9	0.0000020(1)	0.0000056(1)	0.0000128(1)
2111.543194(2)	-8	0.0000008(1)	0.0000033(1)	0.0000077(1)
2115.629163(2)	-7	0.0000006(1)	0.0000043(1)	0.0000088(1)
2119.681131(2)	-6	0.0000010(2)	0.0000039(1)	0.0000086(1)
2123.699014(2)	-5	0.0000015(2)	0.0000040(1)	0.0000077(1)
2127.682635(2)	-4	-0.0000007(2)	0.0000017(1)	0.0000056(1)
2131.631789(2)	-3	0.0000061(2)	0.0000050(1)	0.0000030(2)
2135.546385(3)	-2	-0.0000017(2)	-0.0000040(1)	-0.0000003(2)
2139.426293(4)	-1	-0.0000017(3)	-0.0000092(2)	-0.0000001(3)
2147.081286(4)	1	-0.0000096(3)	-0.0000173(2)	-0.0000118(3)
2150.856170(2)	2	-0.0000073(2)	-0.0000104(1)	-0.0000047(2)
2154.595732(2)	3	-0.0000044(2)	-0.0000059(1)	-0.0000032(1)
2158.299859(2)	4	-0.0000041(2)	-0.0000030(1)	0.0000018(1)
2161.968418(2)	5	-0.0000042(2)	-0.0000015(1)	0.0000035(1)
2165.601216(2)	6	-0.0000024(2)	0.0000003(1)	0.0000049(1)
2169.198133(2)	7	-0.0000028(2)	0.0000007(1)	0.0000036(1)
2172.758988(2)	8	-0.0000021(1)	0.0000003(1)	0.0000035(1)
2176.283706(2)	9	-0.0000007(1)	0.0000017(1)	0.0000042(1)
2179.772096(2)	10	0.0000002(1)	0.0000017(1)	0.0000041(1)
2183.223925(2)	11	0.0000007(1)	0.0000051(1)	0.000007(1)
2186.639201(2)	12	0.0000027(1)	0.0000062(1)	0.0000079(1)
2190.017723(2)	13	0.0000018(2)	0.0000052(1)	0.0000066(1)
2193.359304(2)	14	0.0000031(2)	0.0000071(2)	0.0000087(2)
2196.663860(2)	15	0.0000057(2)	0.0000086(2)	0.0000089(2)
2199.931161(3)	16	0.0000048(2)	0.0000078(2)	0.0000089(2)
2203.161155(3)	17	0.0000054(2)	0.0000082(3)	0.0000080(3)
2206.353654(4)	18	0.0000064(3)	0.0000098(4)	0.0000088(3)
2209.508524(5)	19	0.0000131(4)	0.0000157(5)	0.0000132(5)
2212.625566(6)	20	0.0000050(5)	0.0000109(7)	0.0000107(6)

Table 4.12: Temperature-dependence Self-Broadening coefficients retrieved with Voigt profile.

Line position	m	296K,230K&183K	296,230,183&142K	142,183, &80K
2059.914801(9)	-20	0.5503(5)	0.577(5)	0.763(31)
2064.397107(7)	-19	0.5199(4)	0.567(4)	0.995(23)
2068.847067(5)	-18	0.5518(3)	0.616(3)	1.025(16)
2073.26470(4)	-17	0.5568(3)	0.644(3)	1.006(11)
2077.64992(4)	-16	0.5519(3)	0.641(2)	0.886(8)
2082.002425(3)	-15	0.5697(2)	0.659(2)	0.852(6)
2086.322088(3)	-14	0.5848(2)	0.673(2)	0.836(4)
2090.608883(2)	-13	0.5861(2)	0.679(2)	0.839(3)
2094.862458(2)	-12	0.6008(2)	0.696(2)	0.830(3)
2099.082903(2)	-11	0.6083(2)	0.707(2)	0.822(2)
2103.269899(2)	-10	0.6196(2)	0.72(2)	0.847(2)
2107.423375(2)	-9	0.6228(2)	0.724(1)	0.838(1)
2111.543194(2)	-8	0.6276(2)	0.728(1)	0.835(1)
2115.629163(2)	-7	0.6248(2)	0.726(1)	0.820(1)
2119.681131(2)	-6	0.6215(2)	0.726(1)	0.807(1)
2123.699014(2)	-5	0.6043(2)	0.720(1)	0.802(1)
2127.682635(2)	-4	0.6131(2)	0.728(1)	0.809(1)
2131.631789(2)	-3	0.6010(2)	0.724(1)	0.812(1)
2135.546385(3)	-2	0.6238(2)	0.738(2)	0.795(1)
2139.426293(4)	-1	0.7153(2)	0.765(2)	0.805(1)
2147.081286(4)	1	0.6053(2)	0.732(2)	0.787(1)
2150.856170(2)	2	0.6177(2)	0.741(2)	0.790(1)
2154.595732(2)	3	0.6072(2)	0.733(1)	0.807(1)
2158.299859(2)	4	0.6049(2)	0.714(1)	0.814(1)
2161.968418(2)	5	0.6069(2)	0.715(1)	0.811(1)
2165.601216(2)	6	0.6086(2)	0.718(1)	0.809(1)
2169.198133(2)	7	0.6172(2)	0.723(1)	0.814(1)
2172.758988(2)	8	0.6171(2)	0.724(1)	0.825(1)
2176.283706(2)	9	0.6138(2)	0.723(1)	0.840(1)
2179.772096(2)	10	0.6124(2)	0.716(1)	0.840(1)
2183.223925(2)	11	0.6032(2)	0.708(1)	0.844(2)
2186.639201(2)	12	0.5929(2)	0.698(2)	0.847(2)
2190.017723(2)	13	0.5858(2)	0.685(2)	0.843(3)
2193.359304(2)	14	0.5755(2)	0.674(2)	0.846(3)
2196.663860(2)	15	0.5638(2)	0.661(2)	0.846(4)
2199.931161(3)	16	0.5513(2)	0.645(2)	0.850(6)
2203.161155(3)	17	0.5423(3)	0.632(2)	0.890(8)
2206.353654(4)	18	0.5306(3)	0.618(3)	0.977(11)
2209.508524(5)	19	0.5225(3)	0.597(3)	1.067(16)
2212.625566(6)	20	0.5123(4)	0.566(4)	1.048(22)

Figure 4.14 and 4.15 illustrate the temperature-dependence air-broadening coeffcients of CO at different temperature , and their comparison with other studies. Predoi-Cross *et al.* [10] studied N_2-broadened CO spectra in the 0→2 band, whereas Devi *et al.* [18] reported the temperature-dependence of air-broadened coefficients of CO in the 0→2 band retrieved from spectra covering the 150 to 298 K temperature range.

In Figure 4.15, the seven spectra of the current study at 296 and 230 K show good agreement with the HITRAN database and the with other studies. They all have very steady values between 0.7 and 0.8 cm^{-1} $atm^{-1}K^{-1}$. However, the temperature-dependence air-broadening coefficients of 17 spectra in the temperature range of 296 to 79 K increased slightly for the rotational quantum index $|m|>14$, and decreased drastically ($|m|<14$) compare to the other two temperature intervals, especially spectral lines from R(10) to P(10).

No studies of temperature-dependence air-shift coeffcients of CO in the 0→1 band have previously been reported. Figure 4.16 shows the comparison of air-shift coefficients of CO in the 0→1 band at different temperature intervals and with Devi *et al.* [18], that covered results obtained for the 0→2 band. In that case, spectra at 296 and 230 K are showing lower air-shift coefficients than in the other two intervals. Devi *et al.* [18] reported higher air-shift coeffcient values for the 0→2 band than measured in the 0→1 band, supported by the fact that there is a vibrational dependence for this type of line parameters.

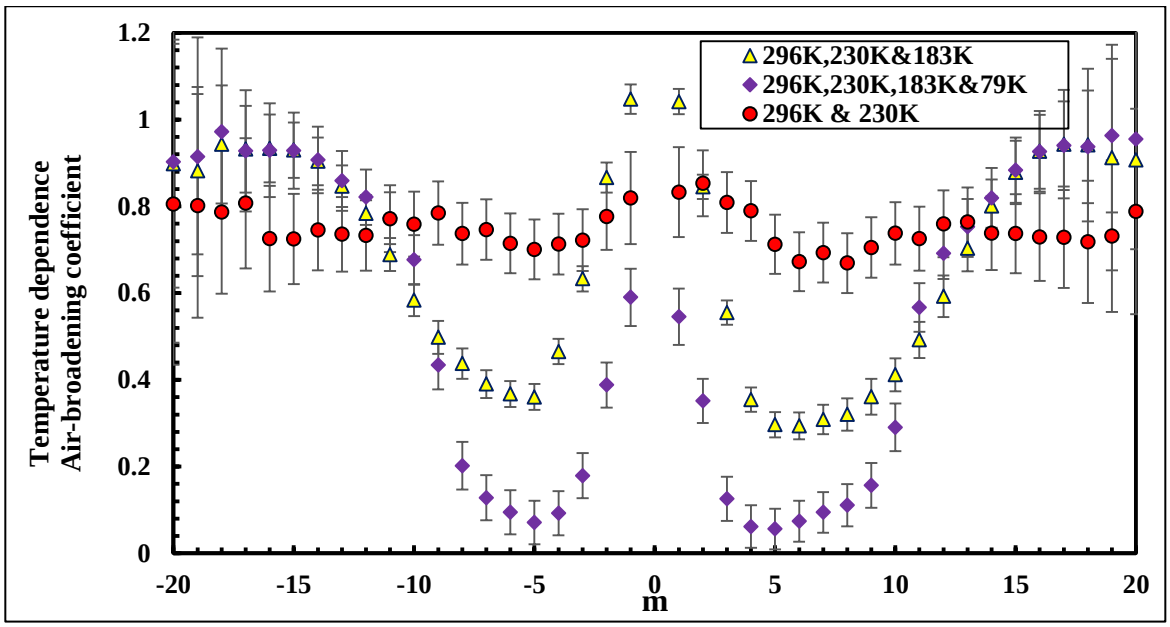

Figure 4.14: Measured temperature-dependence air-broadening coefficients compared at three different temperature ranges.

Temperature-dependent self-broadening coefficients of CO in the 0→1 band have not been determined previously. Figure 4.17 shows the self-broadening coefficients of CO in the 0→1 band, and their comparison. Spectra in the temperature range of 296 to 183 K and 296 to 142 K are showing a similar trend, wheras the low-temperature range 183 to 80 K illustrates a reverse trend for lower quantum number index ($-10 \geq m \leq 10$).

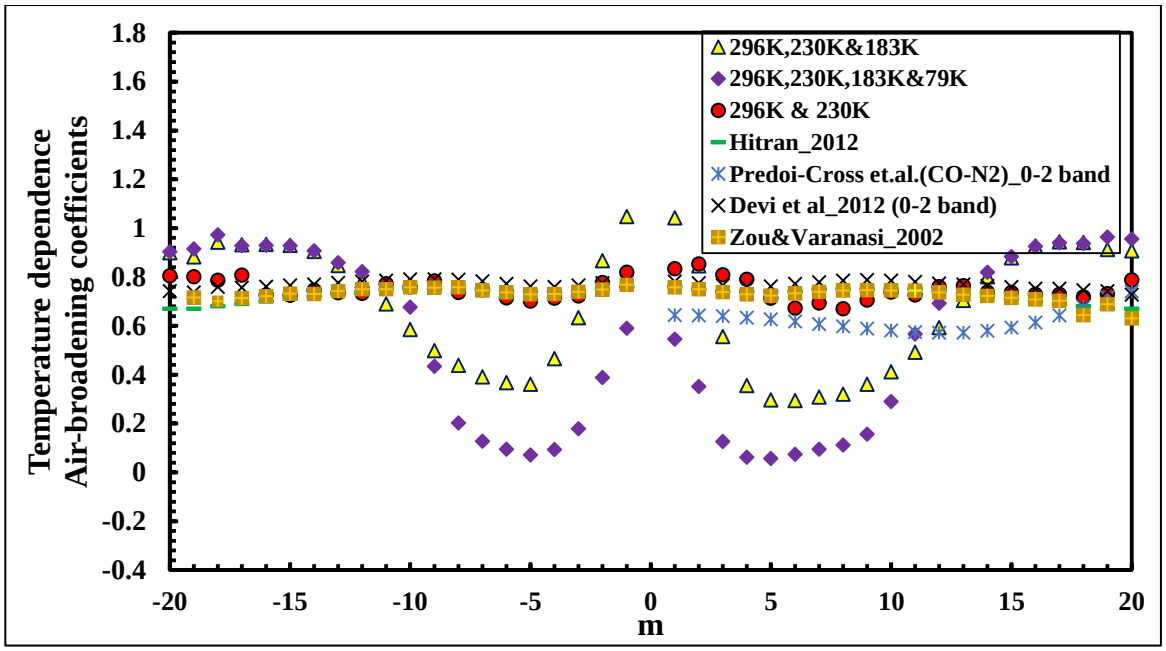

Figure 4.15: Measured temperature-dependence air-broadening coefficients at three different temperature range, and their comparison with other studies. The overlaid sets of data prove that the temperature dependence coefficients depend on the range of temperatures used for spectra.

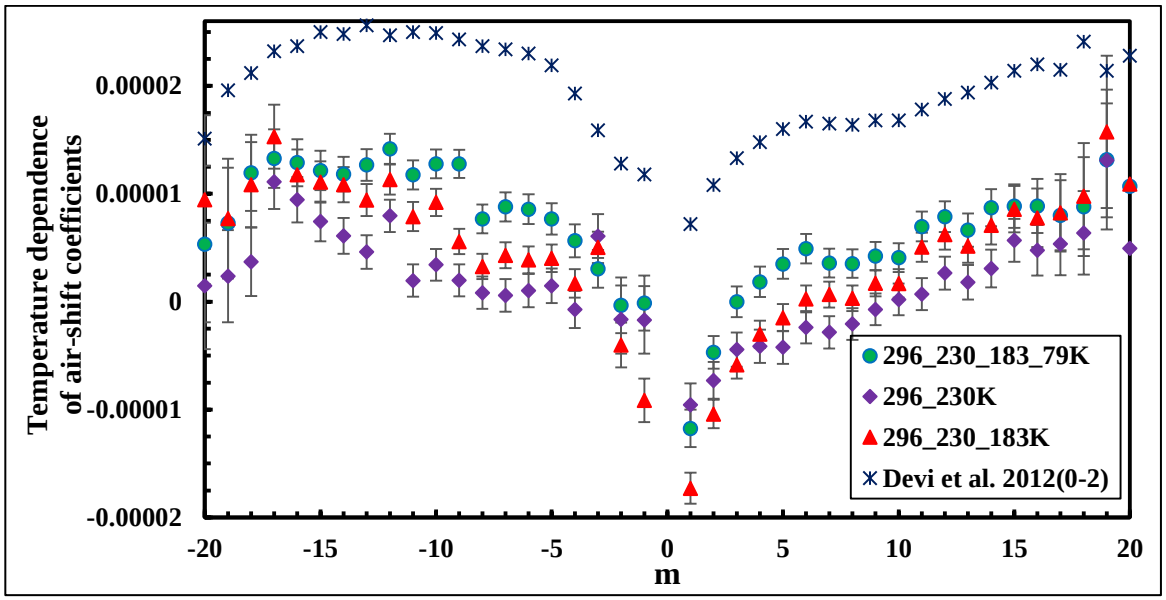

Figure 4.16: Measured temperature-dependence air-shift coefficients at three different temperature range, and their comparison with Devi *et al*. [18].

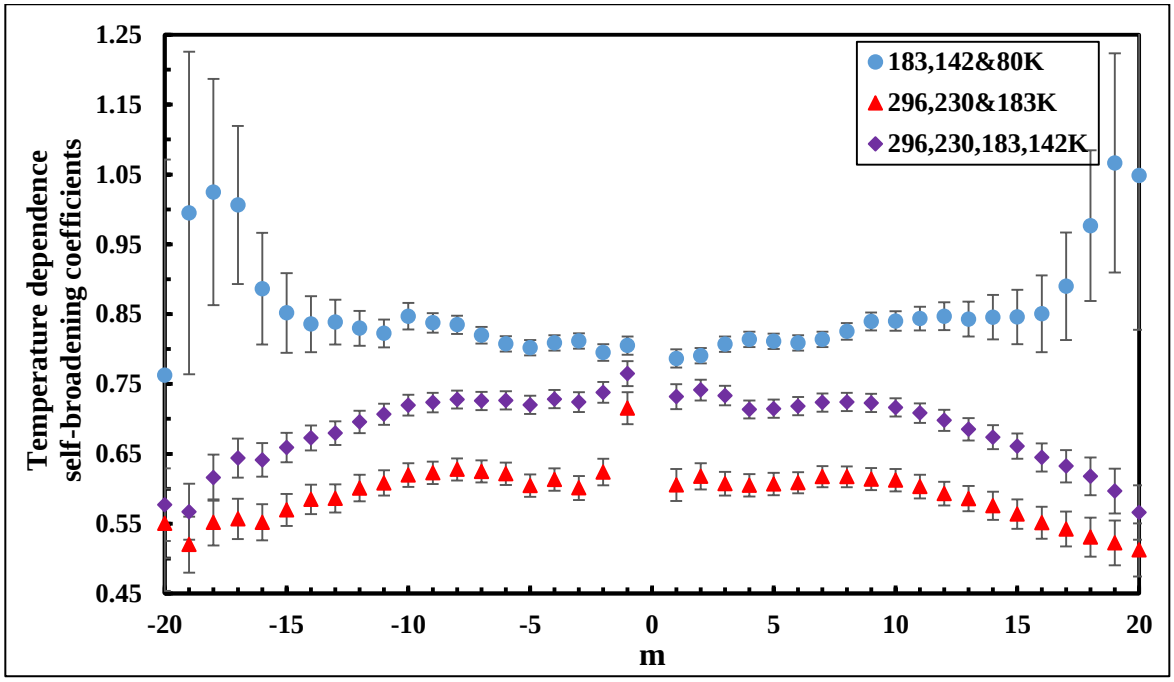

Figure 4.17: Measured temperature-dependence self-shift coefficients compared at three different temperature range.

CHAPTER 5: CONCLUSION AND SUMMARY

In this Thesis, I examined the line-shape parameters of the spectra of pure and air-mixed CO in the 0→1 band at 296 K and other temperatures than room temperature (296 to 79 K) using a multispectral fitting technique. In the first part of this project I measured the line-shape parameters including line intensities, Einstein-A coefficients, self- and air-induced broadening coefficients, air-pressure-induced line-shift coefficients and compared them with previous studies done by other researchers. I also compared my results for different line profiles. Line intensities, Einstein-A coefficients, air-broadening coefficients, air-induced pressure-shift coefficients are in good agreement with the previously reported values. Ratios of intensities (average of 1.007) and broadening coefficients (average of 1.006) with respect to the HITRAN data reflect very good accuracy. For the first time, self-pressure shift coefficients for pure CO in the 0→1 band were considered. I also found that self-broadening and self-pressure-shift coefficients are not showing similarities with the other studies. Most of the spectral lines corresponding to $|m| < 20$ were saturated for pure CO due to their high strength, and therefore only those lines of higher m values were taken in order to compute my results for different line models. In this study, the Voigt and Rautian profiles show better accuracy for measuring the self-broadening and shift coefficients.

The next part of the experimental work was to compare my experimentally determined weak line-mixing coefficients with the theoretically calculated line mixing using the EPG and ECS laws. It can be concluded that the EPG calculation predicts the line-mixing effects which introduce asymmetries in the absorption lines. Here good agreement means, both the approaches are showing similar results which verify the foundation of these two semi-empirical approaches.

CHAPTER FIVE: CONCLUSION AND SUMMARY

In the second part of this experimental work, I have examined 17 spectra of air-mixed CO and 14 spectra of pure CO for a wide range of temperatures from 296 to 79 K. The purpose of this work was to study how temperature affects the line parameters (especially broadening and shifts) of those spectra. With the inclusion of low-temperature spectra, the temperature-dependence air-broadening coefficients dropped rapidly in the strong spectral line regions ($-10 \geq m \leq 10$). In addition, temperature-dependence air-shift coefficients and self-broadening coefficients were measured. The temperature dependent exponents reported in this study will help atmospheric researchers to accurately model the spectral features of different constituent gases present in different planetary atmospheres.

The spectroscopic line-shape parameters of CO resulting from my experimental studies have significant impact for the interpretation of planetary atmospheres which have CO as a trace constituent. Furthermore, more precise radiative transfer modeling can be achieved with help of my laboratory investigation which will help the spectroscopic research community to understand better the terrestrial atmosphere. In addition, these results will be considered for future upgrades of the HITRAN database. Since my experimental studies consider all the needed line parameters, the outcome of my investigation can be used for the analysis of data obtained from the satellite-based sensors including ACE-FTS, TES, and MOPITT. NDACC and TCCON are two ground-based monitoring systems whose data interpretation would also benefit from the results of our laboratory study.

Bibliography

1. Rinsland, C.P. and L.L. Strow, Line Mixing Effects in Solar Occultation Spectra of the Lower Stratosphere - Measurements and Comparisons with Calculations for the 1932-cm^{-1} CO_2 Q Branch. *Applied Optics*, 1989. **28**(3): p. 457-464.

2. Herschel, W., Experiments on the Refrangibility of the Invisible Rays of the Sun. *Philosophical Transactions of the Royal Society of London*, 1800. **90**: p. 284-292.

3. Abney, Captain, Lieut., Colonel, and Festing, On the Influence of the Atomic Grouping in the Molecules of Organic Bodies on Their Absorption in the Infra-Red Region of the Spectrum. *Philosophical Transactions of the Royal Society of London*, 1881. **172**: p. 887-918.

4. Smith, B.C., *Fundamentals of Fourier Transform Infrared Spectroscopy* 1996, Boca Raton: CRC Press.

5. Perkins, W.D., Fourier Transform Infrared Spectroscopy. Part II. Advantages of FT-IR. *Journal of Chemical Education*, 1987. **64**(11): p. A269.

6. Siesler, H.W. and H.W. Siesler, Book Review: IR and Raman Spectroscopy—Fundamental Processing. By Siegfried Wartewig. *Chemphyschem*. **5**(5): p. 757-757.

7. Mozayeni, Applications of FT-IR Spectroscopy. *Journal of the American Oil Chemists' Society*, 1988. **65**(9): p. 1420.

8. Horrison, J.F., Relationship between the Charge Distribution and Dipole Moment Functions of CO and the Related Molecules CS, SiO, and SiS. *Journal of Physical Chemistry*, 2006. **110**: p. 10848-10857.

9. Waring, R.H., G.B. Steventon, and S.C. Mitchell, Molecules of Death. 2nd Edition, 2007.

10. Predoi-Cross, A., C. Luo, P.M. Sinclair, J.R. Drummond, and A.D. May, Line Broadening and the Temperature Exponent of the Fundamental Band in CO–N_2 Mixtures, in *Journal of Molecular Spectroscopy*. 1999. p. 291-303.

11. Petrenko, V.V., P. Martinerie, P. Novelli, D.M. Etheridge, I. Levin, Z. Wang, T. Blunier, J. Chappellaz, J. Kaiser, P. Lang, L.P. Steele, S. Hammer, J. Mak, R.L. Langenfelds, J. Schwander, J.P. Severinghaus, E. Witrant, G. Petron, M.O. Battle, G. Forster, W.T. Sturges, J.F. Lamarque, K. Steffen, and J.W.C. White, A 60 Yr Record of Atmospheric Carbon Monoxide Reconstructed from Greenland Firn Air. *Atmos. Chem. Phys.*, 2013. **13**(15): p. 7567-7585.

12. Connes, J., P. Connes, and J.P. Maillard, *Atlas Des Spectres Dans Le Proche Infrarouge De Venus, Mars, Jupiter Et Saturne*. 1969, [Place of publication not identified]: C.N.R.S.

13. Beer, R., Detection of Carbon Monoxide in Jupiter. *The Astrophysical Journal*, 1975. **200**: p. L167.

14. Noll K.S., R.F. Knacke., T.R. Geballe., and T. A.Tokunaga., Detection of Carbon Monoxide in Saturn. *The Astrophysical Journal*, 1986. **309**: p. L91.

15. Kaplan, L.D., J. Connes, and P. Connes, Carbon Monoxide in the Martian Atmosphere. *The Astrophysical Journal*, 1969. **157**: p. L187.

16. Kakar, R.K., J.W. Walters, and W.J. Wilson, Mars: Microwave Detection of Carbon Monoxide. *Science*, 1977. **196**(4294): p. 1090.

17. Connes, P., Carbon Monoxide in the Venus Atmosphere. *The Astrophysical Journal*, 1968. **152**: p. 731.

18. Devi, V.M., D.C. Benner, M.A.H. Smith, A.W. Mantz, K. Sung, L.R. Brown, and A. Predoi-Cross, Spectral Line Parameters Including Temperature Dependences of Self- and Air-Broadening in the 2←0 Band of CO at 2.3μm. *Journal of Quantitative Spectroscopy and Radiative Transfer*, 2012. **113**(11): p. 1013-1033.

19. Nakazawa, T. and M. Tanaka, Measurements of Intensities and Self- and Foreign-Gas-Broadened Half-Widths of Spectral Lines in the Co Fundamental Band. *Journal of Quantitative Spectroscopy and Radiative Transfer*, 1982. **28**(5): p. 409-416.

20. Devi, V.M., A. Predoi-Cross, D.C. Benner, M.A.H. Smith, C.P. Rinsland, and A.W. Mantz, Self- and H_2-Broadened Width and Shift Coefficients in the 2 ← 0 Band of $^{12}C^{16}O$: Revisited. *Journal of Molecular Spectroscopy*, 2004. **228**(2): p. 580-592.

21. Devi, V.M., D.C. Benner, M.A.H. Smith, A.W. Mantz, K. Sung, and L.R. Brown, Spectral Line Parameters Including Temperature Dependences of Air-Broadening for the 2←0 Bands of $^{13}C^{16}O$ and $^{12}C^{18}O$ at 2.3μm.. *Journal of Molecular Spectroscopy*, 2012. **276–277**: p. 33-48.

22. Rothman, L.S., D. Jacquemart, A. Barbe, D. C. Benner, M. Birk, L.R. Brown, M.R. Carleer, C. Chackerian Jr, K. Chance, L.H. Coudert, V. Dana, V.M. Devi, J.M. Flaud, R.R. Gamache, A. Goldman, J.M. Hartmann, K.W. Jucks, A.G. Maki, J.Y. Mandin, S.T. Massie, J. Orphal, A. Perrin, C.P. Rinsland, M.A.H. Smith, J. Tennyson, R.N. Tolchenov, R.A. Toth, J. Vander Auwera, P. Varanasi, and G. Wagner, The Hitran 2004 Molecular Spectroscopic Database. *Journal of Quantitative Spectroscopy and Radiative Transfer*, 2005. **96**(2): p. 139-204.

23. Rothman, L.S., I.E. Gordon, A. Barbe, D.C. Benner, P.F. Bernath, M. Birk, V. Boudon, L.R. Brown, A. Campargue, J.P. Champion, K. Chance, L.H. Coudert, V.

Dana, V.M. Devi, S. Fally, J.M. Flaud, R.R. Gamache, A. Goldman, D. Jacquemart, I. Kleiner, N. Lacome, W.J. Lafferty, J.Y. Mandin, S.T. Massie, S.N. Mikhailenko, C.E. Miller, N. Moazzen-Ahmadi, O.V. Naumenko, A.V. Nikitin, J. Orphal, V.I. Perevalov, A. Perrin, A. Predoi-Cross, C.P. Rinsland, M. Rotger, M. Šimečková, M.A.H. Smith, K. Sung, S.A. Tashkun, J. Tennyson, R.A. Toth, A.C. Vandaele, and J. Vander Auwera, The Hitran 2008 Molecular Spectroscopic Database. *Journal of Quantitative Spectroscopy and Radiative Transfer*, 2009. **110**(9–10): p. 533-572.

24. Rothman, L.S., I.E. Gordon, Y. Babikov, A. Barbe, D. Chris Benner, P.F. Bernath, M. Birk, L. Bizzocchi, V. Boudon, L.R. Brown, A. Campargue, K. Chance, E.A. Cohen, L.H. Coudert, V.M. Devi, B.J. Drouin, A. Fayt, J.M. Flaud, R.R. Gamache, J.J. Harrison, J.M. Hartmann, C. Hill, J.T. Hodges, D. Jacquemart, A. Jolly, J. Lamouroux, R.J. Le Roy, G. Li, D.A. Long, O.M. Lyulin, C.J. Mackie, S.T. Massie, S. Mikhailenko, H.S.P. Müller, O.V. Naumenko, A.V. Nikitin, J. Orphal, V. Perevalov, A. Perrin, E.R. Polovtseva, C. Richard, M.A.H. Smith, E. Starikova, K. Sung, S. Tashkun, J. Tennyson, G.C. Toon, V.G. Tyuterev, and G. Wagner, The Hitran2012 Molecular Spectroscopic Database. *Journal of Quantitative Spectroscopy and Radiative Transfer*, 2013. **130**: p. 4-50.

25. Zou, Q. and P. Varanasi, New Laboratory Data on the Spectral Line Parameters in the 1-0 and 2-0 Bands of 12c16o Relevant to Atmospheric Remote Sensing. *Journal of Quantitative Spectroscopy and Radiative Transfer*, 2002. **75**(1): p. 63-92.

26. Régalia-Jarlot, L., X. Thomas, P. Von der Heyden, and A. Barbe, Pressure-Broadened Line Widths and Pressure-Induced Line Shifts Coefficients of the (1-0) and (2-0) Bands Of. *Journal of Quantitative Spectroscopy and Radiative Transfer*, 2005. **91**(2): p. 121-131.

27. Brault, J.W., L.R. Brown, J. Chackerian, C. , R. Freedman, A. Predoi-Cross, and A.S. Pine, Self-Broadened $^{12}C^{16}O$ Line Shapes in the 2←0 Band. *Journal of Molecular Spectroscopy*, 2003. **222**(2): p. 220-239.

28. Mantz, A.W., V. Malathy Devi, D. C. Benner, M.A.H. Smith, A. Predoi-Cross, and M. Dulick, A Multispectrum Analysis of Widths and Shifts in the 2010–2260 cm^{-1} Region of $^{12}C^{16}O$ Broadened by Helium at Temperatures between 80 and 297 K. *Journal of Molecular Structure*, 2005. **742**(1–3): p. 99-110.

29. Thibault, F., J. Boissoles, R. Le Doucen, R. Farrenq, M. Morillon-Chapey, and C. Boulet, Line-by-Line Measurements of Interference Parameters for the 0–1 and 0–2 Bands of CO in He, and Comparison with Coupled-States Calculations. *The Journal of Chemical Physics*, 1992. **97**(7): p. 4623-4632.

30. Boissoles, J., C. Boulet, D. Robert, and S. Green, IOS and ECS Line Coupling Calculation for the CO–He System: Influence on the Vibration–Rotation Band Shapes. *The Journal of Chemical Physics*, 1987. **87**(6): p. 3436-3446.

31. Predoi-Cross, A., J.P. Bouanich, D.C. Benner, A.D. May, and J.R. Drummond, Broadening, Shifting, and Line Asymmetries in the 2← 0 Band of CO and CO-N_2:

Experimental Results and Theoretical Calculations. *The Journal of chemical physics*, 2000. **113**(1): p. 158.

32. Hollas, J.M., Modern Spectroscopy 4th Edition, 2004.

33. Povey, C., High Resolution Spectroscopy and Applications. *Physics and Astronomoy Department, Univeristy of Lethbridge*, 2013.

34. Aarthi, G., Assistant Professor, Vit University. *Introdcution to Optoelectronic Devices*, 2012.

35. Giancoli, D.C., *Physics*: *Principles with Applications*. Englewood Cliffs, NJ: Prentice Hall, 2005.

36. Bernath, P.F., *Spectra of Atoms and Molecules*. 2015, [Oxford, UK]: Oxford University Press.

37. Berman and P. R., Speed-Dependent Collisional Width and Shift Parameters in Spectral Profiles. *Journal of Quantitative Spectroscopy and Radiative Transfer*, 1972. **12**(9): p. 1331-1342.

38. Hartmann, J.-M., C. Boulet, and D. Robert, *Collisional Effects on Molecular Spectra: Laboratory Experiments and Models, Consequences for Applications*. 2008, Elsevier.

39. Joubert, P., X. Bruet, J. Bonamy, D. Robert, F. Chaussard, X. Michaut, R. Saint-Loup, and H. Berger, H_2 Vibrational Spectral Signatures in Binary and Ternary Mixtures: Theoretical Model, Simulation and Application to Cars Thermometry in High Pressure Flames. *Comptes Rendus de l'Académie des Sciences - Series IV - Physics*, 2001. **2**(7): p. 989-1000.

40. Sergei, G.R. and I.S. Igor, The Effect of Collisions on the Doppler Broadening of Spectral Lines. *Soviet Physics Uspekhi*, 1967. **9**(5): p. 701.

41. Cuadros, F.Cachadiña, and W. I. Ahumada, Determination of Lennard-Jones Interaction Parameters Using a New Procedure. *Molecular Engineering*, 1996. **6**(3): p. 319-325.

42. Forester, T.R. and W. Smith, Dlpoly, CCP5 Program Library. 2001.

43. Nosé, S., A Unified Formulation of the Constant Temperature Molecular Dynamics Methods. *The Journal of Chemical Physics*, 1984. **81**(1): p. 511.

44. Brunner, T.A., D. Prichard, and K.P. Lawley, Dynamics of the Excited State. *Advances in Chemical Physics, Volume 50*, 1982.

45. Hirschfelder, J. O. Curtiss, C. F. Bird, R. B. Mayer, and M. Goeppert, *Molecular Theory of Gases and Liquids*. Vol. 26. 1954: Wiley New York.

46. Birnbaum, G., *Microwave Pressure Broadening and Its Application to Intermolecular Forces*, in *Advances in Chemical Physics*. 1967. p. 487-548.

47. Bonamy, J., D. Robert, and C. Boulet, Simplified Models for the Temperature Dependence of Linewidths at Elevated Temperatures and Applications to CO Broadened by Ar and N_2. *Journal of Quantitative Spectroscopy and Radiative Transfer*, 1984. **31**(1): p. 23-34.

48. Anderson, P.W., Pressure Broadening in the Microwave and Infra-Red Regions. *Physical Review*, 1949. **76**(5): p. 647-661.

49. Tsao, C.J. and B. Curnutte, Line-Widths of Pressure-Broadened Spectral Lines. *Journal of Quantitative Spectroscopy and Radiative Transfer*, 1962. **2**(1): p. 41-91.

50. Nakazawa, T. and M. Tanaka, Intensities, Half-Widths and Shapes of Spectral Lines in the Fundamental Band of CO at Low Temperatures. *Journal of Quantitative Spectroscopy and Radiative Transfer*, 1982. **28**(6): p. 471-480.

51. Lemoal, M.F. and F. Severin, N_2 and H_2 Broadening Parameters in the Fundamental-Band of CO. *Journal of Quantitative Spectroscopy & Radiative Transfer*. **35(2)**(1986): p. 145-152.

52. Drascher, T., T.F. Giesen, T.Y. Wang, N. Schmücker, R. Schieder, G. Winnewisser, P. Joubert, and J. Bonamy, Temperature-Dependent Line Shift and Broadening of CO Infrared Transitions. *Journal of Molecular Spectroscopy*, 1998. **192**(2): p. 268-276.

53. Coleman, M.D. and T.D. Gardiner, Sensitivity of Model-Based Quantitative FTIR to Instrumental and Spectroscopic Database Error Sources. *Vibrational Spectroscopy*, 2009. **51**(2): p. 177-183.

54. Egevskaya, T.B., A Small Interferometer—a Double Cat's Eye— for Rapid-Scanning Fts. *Infrared Physics*, 1984. **24**(2): p. 329-331.

55. Mantz, A.W., A. Henry, and A. Valentin, Stabilized Tunable Diode Laser Measurements of the P(2) Line in the ^{13}CO Fundamental Band Broadened by Helium at Temperatures between 11.5 and 298.6 K. *Journal of Molecular Spectroscopy*, 2001. **207**(1): p. 113-119.

56. Benner, D.C., C.P. Rinsland, V.M. Devi, M.A.H. Smith, and D. Atkins, A Multispectrum Nonlinear Least Squares Fitting Technique. *Journal of Quantitative Spectroscopy and Radiative Transfer*, 1995. **53**(6): p. 705-721.

57. Rohart, F., H. Mäder, and H.W. Nicolaisen, Speed Dependence of Rotational Relaxation Induced by Foreign Gas Collisions: Studies on CH_3F by Millimeter Wave Coherent Transients. *The Journal of Chemical Physics*, 1994. **101**(8): p. 6475.

58. Rohart, F., A. Ellendt, F. Kaghat, and H. Mäder, Self and Polar Foreign Gas Line Broadening and Frequency Shifting of CH_3F: Effect of the Speed Dependence Observed by Millimeter-Wave Coherent Transients. *Journal of Molecular Spectroscopy*, 1997. **185**(2): p. 222-233.

59. Wehr, R., R. Ciuryło, A. Vitcu, F. Thibault, J.R. Drummond, and A.D. May, Erratum to "Dicke-Narrowed Spectral Line Shapes of CO in Ar: Experimental Results and a Revised Interpretation" [J. Mol. Spectrosc. 235 (2006) 54–68]. *Journal of Molecular Spectroscopy*, 2006. **237**(1): p. 127.

60. Devi, V.M., D.C. Benner, L.R. Brown, C.E. Miller, and R.A. Toth, Line Mixing and Speed Dependence in CO_2 at 6348 cm^{-1}: Positions, Intensities, and Air- and Self-Broadening Derived with Constrained Multispectrum Analysis. *Journal of Molecular Spectroscopy*, 2007. **242**(2): p. 90-117.

61. Gang, L., E.G. Iouli, S.R. Laurence, T. Yan, H. Shui-Ming, K. Samir, C. Alain, and S.M. Emile, Rovibrational Line Lists for Nine Isotopologues of the CO Molecule in the X 1σ+ Ground Electronic State. *The Astrophysical Journal Supplement Series*, 2015. **216**(1): p. 15.

62. Levy, A., N. Lacome, J. Chackerian, C., and K. Narahari Rao, Spectroscopy of the Earth's Atmosphere and of the Interstellar Medium. *Academic Press, New York*, 1992.

63. Rodrigues, R., K. W.Jucks, N. Lacome, G. Blanquet, J. Walrand, W.A. Traub, B. Khalil, R. Le Doucen, A. Valentin, C. Camy-Peyret, L. Bonamy, and J.M. Hartmann, Model, Software, and Database for Computation of Line-Mixing Effects in Infrared Q Branches of Atmospheric CO_2—I. Symmetric Isotopomers. *Journal of Quantitative Spectroscopy and Radiative Transfer*, 1999. **61**(2): p. 153-184.

64. Predoi-Cross, A., K. Esteki, H. Rozario, H. Naseri, S. Latif, F. Thibault, V.M. Devi, M.A.H. Smith, and A.W. Mantz, Theoretical and Revisited Experimentally Retrieved He-Broadened Line Parameters of Carbon Monoxide in the Fundamental Band. *Journal of Quantitative Spectroscopy and Radiative Transfer*, 2016. **184**: p. 322-340.

65. Griffiths, P.R., J. de Haseth, Fourier Trasform Infrared Spectroscopy, 2nd Editor, 2007.